

# MAGNETIC HEUSLER COMPOUNDS

Tanja Graf<sup>1,2</sup>, Jürgen Winterlik<sup>1</sup>, Lukas Mühler<sup>1,3</sup>, Gerhard H. Fecher<sup>1,3</sup>, Claudia Felser<sup>1,3</sup> and Stuart S.P. Parkin<sup>2</sup>

## Contents

1. Introduction	1
2. Crystal Structure and Atomic Ordering	4
3. Semiconductors	10
3.1. Magnetic SCs	13
3.2. TE materials	14
3.3. Topological insulators	17
4. The Slater–Pauling Rule	23
5. Half-Metallic Ferromagnets	27
6. Heusler Compounds in Devices for Spintronic Applications	37
6.1. Magneto resistance devices	38
6.2. Spin injection	43
7. Tetragonal Heusler Compounds	46
7.1. Tetragonal Heusler compounds for shape-memory and magnetocaloric applications	57
8. Summary and Outlook	64
Acknowledgments	65
References	65

## 1. INTRODUCTION

The history of one of the most exciting material classes can be traced back to the year 1903 when Fritz Heusler discovered that an alloy with the composition  $\text{Cu}_2\text{MnAl}$  behaves like a ferromagnet, although non of its constituent elements is magnetic by itself (Heusler, 1903; Heusler et al., 1903). However, it took three decades until the crystal structure was determined to be ordered with a face centered, cubic lattice (Bradley and

<sup>1</sup> Institute for Analytical and Inorganic Chemistry, Johannes Gutenberg-University, Mainz, Germany

<sup>2</sup> IBM Almaden Research Center, San Jose, California, USA

<sup>3</sup> Max-Planck-Institute for Chemical Physics of Solids, Dresden, Germany

Rodgers, 1934; Heusler, 1934). Unfortunately, they faded almost in oblivion in the following decades, and only few reports on the synthesis and properties of new Heusler compounds were published in the 1970s and 1980s (Brooks and Williams, 1975; van Engen and Bushow, 1983; van Engen et al., 1983; Webster, 1971). In recent years, Heusler compounds were rediscovered and their enormous potential in many diverse fields, ranging from spintronics, over shape memory alloys and semiconductors (SCs) with tunable band gaps to topological insulators, generated a tremendous research effort. For further insights into Heusler materials from the viewpoint of a chemist, the interested reader is referred to our recent review article (Graf et al., 2011a).

Generally, Heusler compounds belong to a group of ternary intermetallics with the stoichiometric composition XYZ (often called “Half-Heusler”) or  $X_2YZ$  and crystallize in an ordered  $f\bar{c}c$ -based structure. Mostly, X and Y are transition or rare earth (RE) metals and Z is usually a main group element.

The quite new research area of spintronics is a multidisciplinary field. New materials must be found for satisfying the different types of demands. The search for stable half-metallic ferromagnets (HMFs) and ferromagnetic SCs with Curie temperatures ( $T_C$ ) higher than room temperature (RT) is still a challenge for solid state scientists. In principle, a HMF behaves like a metal for one spin direction and like an insulator for the other spin direction. A general understanding of how structures are related to properties is a necessary prerequisite for designing new materials showing desired functionalities. In this context, computational simulations are an important tool.

The development of magnetic Heusler compounds specifically designed for spintronic applications made tremendous progress in the very recent past. The boom about Heusler compounds for spintronic applications and the huge number of both, theoretical and experimental investigations (over 700 publications concerning  $X_2YZ$  Heusler compounds in the past 8–9 years) began in 2002/2003 with the observation of—at that time—large negative magnetoresistance (MR) in powder compacts of  $\text{Co}_2\text{Cr}_{0.6}\text{Fe}_{0.4}\text{Al}$  (Block et al., 2003). A magnetoresistive effect of 30% in a small magnetic field of 0.1 T at RT was found. This demonstrated for the first time the feasibility of a cheap and simple magnetic sensor based on polycrystalline, intermetallic materials. This value was later optimized by using powder compacts of  $\text{Co}_2\text{Cr}_{0.6}\text{Fe}_{0.4}\text{Al}$ , mixed with insulating  $\text{Al}_2\text{O}_3$ , to a maximum MR ratio of 88% in an induction field of 0.125 T at 295 K (Block et al., 2006). The discovery of  $\text{Co}_2\text{FeSi}$ , the Heusler compound with the highest magnetic moment of  $5.97 \mu_B$  at 5 K and the highest Curie temperature of 1100 K caught further attention by chemists as well as physicists. (Wurmehl et al., 2006a,c).

Indeed, the properties of many Heusler compounds can be predicted by simply counting the number of valence electrons (Felser et al., 2007; Graf

et al., 2011a,b), which allows for instance the design of SCs with tunable band gaps (Gruhn, 2010), superconductors (Winterlik et al., 2009), HMF (Barth et al., 2010; Felser et al., 2007; Wurmehl et al., 2006a), compensated ferrimagnets (Balke et al., 2007a; Winterlik et al., 2008), and topological insulators (Chadov et al., 2010; Lin et al., 2010) simply by changing the constituent elements. Despite all these interesting properties of Heusler compounds, in this chapter we will focus on magnetic materials and their applications in the field of spintronics.

Discussing the properties of magnetic Heusler compounds, one major difference between Half-Heusler and Heusler compounds has to be considered: Half-Heusler materials exhibit one magnetic sublattice since only the atoms on the octahedral sites carry localized magnetic moments of considerable sizes, while in  $X_2YZ$  Heusler compounds two magnetic sublattices are present which are coupled to each other, as shown in Fig. 1.1.

Since the magnetic moment is carried by the X atom occupying an octahedral lattice position, magnetic Half-Heusler materials exist mainly for  $X = \text{Mn}$ , and RE which is a result of the localized nature of the four 3d electrons of  $\text{Mn}^{3+}$  and the 4f electrons, respectively. Among the RE-containing Heusler compounds known in literature, most compounds are semiconducting or semimetallic systems and antiferromagnets with low Néel temperatures (Casper and Felser, 2008; Gofryk et al., 2005). Since the magnetic ions occupy an NaCl-type sublattice, their distance is large which hints at a magnetic interaction based on a super-exchange mechanism. Despite the Mn-containing Half-Heusler compounds, which are HMF with high  $T_C$  (Casper et al., 2006; de Groot et al., 1983; Kübler, 1984), only very few ferromagnetic Half-Heusler compounds are described in literature, for instance NdNiSb and VCoSb (Hartjes and Jeitschko, 1995; Heyne et al., 2005).

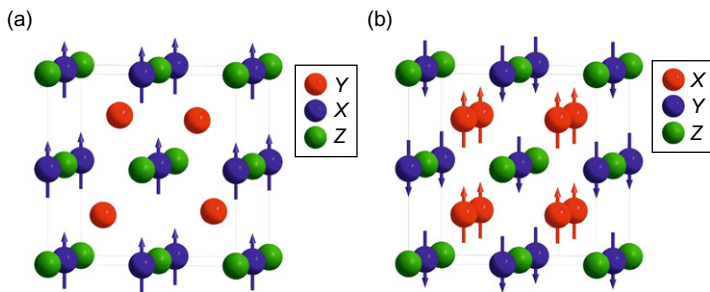


**Figure 1.1** Half-Heusler compounds exhibit only one magnetic sublattice since only the atoms on the octahedral sites carry a localized magnetic moment.  $X_2YZ$  Heusler compounds, however, have two magnetic sublattices which can couple ferromagnetically or antiferromagnetically (shown here). Reprinted from Graf et al. (2011a) with kind permission of Elsevier.

For the  $X_2YZ$  Heusler compounds the situation is completely different because the two X atoms occupy tetrahedral lattice sites allowing for magnetic interaction between the X atoms. Thus a second, more delocalized magnetic sublattice is formed in addition to the one originating from the Y atoms (compare Fig. 1.1). Due to the two different magnetic sublattices, the  $X_2YZ$  Heusler compounds can show all kinds of magnetic phenomena, and in fact, today ferromagnetism, ferrimagnetism, antiferromagnetism, and half-metallic ferromagnetism are known.

Tetragonally distortions corresponding to a type of band Jahn–Teller effect have been reported in the 1970s (Suits, 1976). Recently, these tetragonally distorted Heusler compounds have attracted considerable attention (Balke et al., 2007a; Winterlik et al., 2008; Wu et al., 2009, 2010). The tetragonal distortion is observed for  $Mn_2YZ$  compounds crystallizing in the inverse Heusler structure. In this structure, the Mn atoms occupy two different lattice sites, one with tetragonal and one with octahedral coordination. Theoretical investigations by Kübler showed that the Mn atom on the octahedral site formally possesses an oxidation state of +3 ( $Mn^{3+}$ ,  $d^4$ ) (Kübler et al., 1983). According to crystal field theory  $d^4$  high spin ions in an octahedral coordination sphere undergo a tetragonal distortion, which leads to a rearrangement of the molecular orbitals and an overall energy gain. This phenomenon is commonly known as the Jahn–Teller effect. Alternatively, a double degenerate van Hove singularity, that is, saddle point in the band structure, can lead to a tetragonal distortion since this singularity maximizes the band energy, leading to an unfavorable condition, which is avoided by a tetragonal lattice distortion. In the case of  $Mn_2YZ$  compounds, the cubic unit cell can undergo an elongation or a compression along the  $c$ -axis. Consequently, the symmetry of the crystal changes from the cubic space group  $F43m$  to the tetragonal space group  $I4m2$ . Up to now, only few tetragonally distorted Heusler materials have been studied thoroughly,  $Mn_{3-x}Ga$  being the most prominent example (Balke et al., 2007a; Winterlik et al., 2008). These materials are particularly interesting due to the perpendicular magnetic anisotropy (PMA), which can be achieved in thin films (Wu et al., 2009) opening the door to spin-transfer torque (STT) devices. Many potential compounds  $Mn_2YZ$  and their alloys  $Mn_{3-x}Y_xZ$  for a STT application are still undiscovered. However, these materials still exhibit certain challenges, which have to be overcome for technological application. It is therefore essential to design new materials that fulfill all the required criteria as we will discuss later.

## 2. CRYSTAL STRUCTURE AND ATOMIC ORDERING

The Half-Heusler compounds have the general formula  $XYZ$  and crystallize in a noncentrosymmetric cubic structure (space group no. 216,  $F43m$ ,  $C1_b$ ) which is a ternary ordered variant of the  $CaF_2$  structure and can

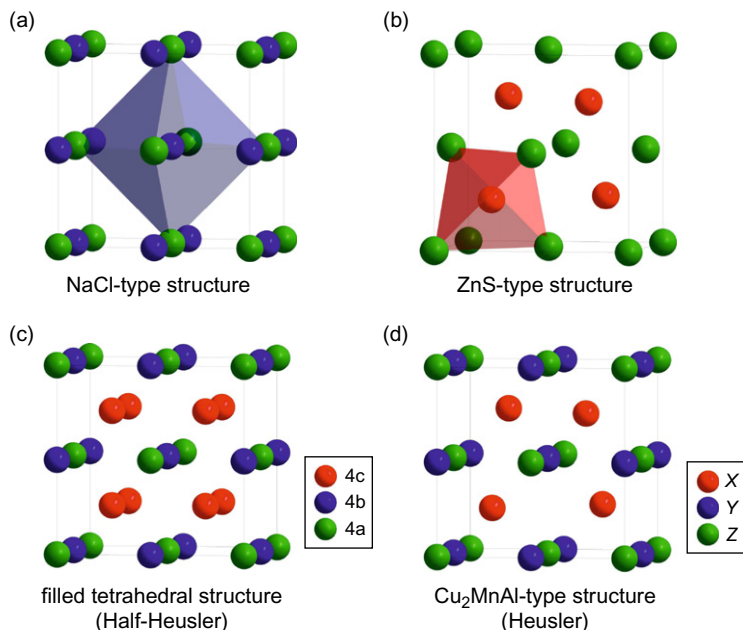


**Figure 1.2** (a) Rock salt structure, (b) Zinc blende structure and their relations to the Half-Heusler structure (c), and to the Heusler structure (d). Reprinted from [Graf et al. \(2011a\)](#) with kind permission of Elsevier.

be derived from the tetrahedral ZnS-type structure by filling the octahedral lattice sites (Fig. 1.2). A characteristic feature of this Half-Heusler structure type are three interpenetrating *fcc* sublattices, each of which are occupied by the X, Y and Z atoms ([Webster and Ziebeck, 1988](#)). The corresponding occupied Wyckoff positions are 4a (0, 0, 0), 4b (1/2, 1/2, 1/2), and 4c (1/4, 1/4, 1/4). In principle, three inequivalent atomic arrangements are possible, which have to be carefully differentiated, especially if electronic structure calculations are performed, since the correct site assignment is crucial for the obtained electronic structure.

Viewing the Half-Heusler structure as a ZnS-sublattice (Wyckoff positions 4a and 4c), in which the octahedral sites are occupied (4b), emphasizes the covalent bonding interaction between two of the contained elements which plays a major role for the electronic properties of the material. In contrast, it is worth to mention that the atoms on position 4a and 4b built a NaCl-type sublattice, that is, their interaction has a strong ionic character. The specific ordering of the atoms depends strongly on the chemical nature of the elements. In MgAgAs, for instance, Ag and anionic As form the covalent ZnS-sublattice, while Mg and Ag built the NaCl-type lattice

(Nowotny and Sibert, 1941). Consequently, As is eightfold coordinated by monovalent and divalent cations. Even though MgAgAs is the assigned prototype of all Half-Heusler compounds, it has to be clarified that MgAgAs actually crystallizes with a different atomic order compared to most other Half-Heusler compounds (Villars and Calvert, 1991). So in this case a peculiar situation is present: The assigned prototype itself is an exception! MgCuSb is an example which represents the atomic arrangement in most Half-Heusler materials correctly (Nowotny and Sibert, 1941; Nuss and Jansen, 2002); here, Cu and anionic Sb form the ZnS sublattice, and cationic Mg and anionic Sb occupy the ionic NaCl-type sublattice. Thus, Cu is coordinated by four Mg and four Sb atoms in form of an ideal cube.

Which of these two described atomic arrangements is preferred, depends on the one hand on the difference in radii of the involved atoms, and on the other hand on the nature of interatomic interaction. If the difference in radii of the involved cations is rather small (Mg, Ag), the anion has eight cations in its coordination sphere and every cation is surrounded by four anions. From metal–organic chemistry it is well known that some metals exhibit a strong tendency to form covalent bonds, for instance Mg, Ag or Li. This property supports the formation of the covalent ZnS-type lattice, if such elements are contained in the compounds. Examples are LiAlSi, LiMgSb and the above discussed MgAgAs. However, if the cations show distinct differences in size and metal–metal interaction is dominant, as it is the case in MgCuSb, the anion (Sb) is coordinated by four cations (Cu), Cu for his part by four anions and four cations, and Mg by four cations. Further examples for this kind of order are all Half-Heusler compounds containing two transition metals and the REYZ materials. In some cases, both variants are labeled with the same prototype, LiAlSi type (Villars and Calvert, 1991). However, most Half-Heusler compounds containing two transition metals are designated with MgAgAs-type structure (Villars and Calvert, 1991), which is actually wrong. We would like to emphasize that the correct assignment of the lattice positions is essential to understand the structure–to–property relations of these materials and special care has to be taken when performing theoretical studies to obtain correct results.

The Heusler compounds with  $X_2YZ$  composition crystallize in the cubic space group  $Fm\bar{3}m$  (space group no. 225) with  $Cu_2MnAl$  ( $L2_1$ ) as prototype (Bradley and Rodgers, 1934; Heusler, 1903; Heusler et al., 1903; Heusler, 1934). The X atoms occupy the Wyckoff position 8c ( $1/4, 1/4, 1/4$ ), the Y and the Z atoms are located at 4a (0, 0, 0) and 4b ( $1/2, 1/2, 1/2$ ), respectively. Similar to Half-Heusler materials, this structure consists of four interpenetrating *fcc* sublattices, two of which are equally occupied by X. A rock salt-type lattice is formed by the least and most electropositive element (Y and Z). Due to the ionic character of their interaction, these elements are coordinated octahedrally. On the other hand, all tetrahedral holes are filled by X. This structure can also be understood as a zinc blende-type sublattice, build up by one X and Z,

the second X occupies the remaining tetrahedral holes, whereas Y is located in the octahedral holes. These relations are illustrated in Fig. 1.2. In the literature, Heusler compounds are often described by a CsCl-like superstructure. This is reasonable under the assumption of disorder on the Y and Z sites and if the unit cell edges of the Heusler cell is shifted by  $(1/4, 1/4, 1/4)$  with respect to the  $Fm\bar{3}m$  cell. The combination of both X-site  $\bar{f}cc$  lattices leads to a simple cubic lattice. The Y and the Z atoms occupy the centers of the simple cubic lattice, which results in the CsCl-like superstructure. This kind of disorder between the Y and Z site is often observed in half-metallic Heusler systems but fortunately does not affect the properties significantly. The shifted Heusler cell, as well as the CsCl structure, are displayed in Fig. 1.3. This description provides an intuitive understanding for one design rule: The combination of two binary alloys crystallizing in the CsCl-type structure leads to the formation of Heusler compounds (Butler et al., 2011).

In addition to the structure described above, an inverse Heusler structure is observed, if the atomic number of Y is higher than the one of X from the same period ( $Z(Y) > Z(X)$ ), however, it may also appear in compounds with transition metals from different periods (Puselj and Ban, 1969). In all cases, the element X is more electropositive than Y. Consequently, Y and Z form a zinc blende lattice to achieve an octahedral coordination for X. The remaining X atoms fill the tetrahedral holes with fourfold symmetry. The structure is still described by four interpenetrating  $\bar{f}cc$  sublattices, however the X atoms do not form a simple cubic lattice. Instead, they are placed on the Wyckoff positions 4a (0, 0, 0) and 4d ( $3/4, 3/4, 3/4$ ), while the Y and the Z atoms are located at 4b ( $1/2, 1/2, 1/2$ ) and 4c ( $1/4, 1/4, 1/4$ ), respectively. The prototype of this structure is  $\text{CuHg}_2\text{Ti}$  with space group  $F\bar{4}3m$  (space group no. 216). The difference to normal Heusler compounds can be emphasized by expressing the formula as  $(XY)_2X'Z$ . This inverse Heusler structure is

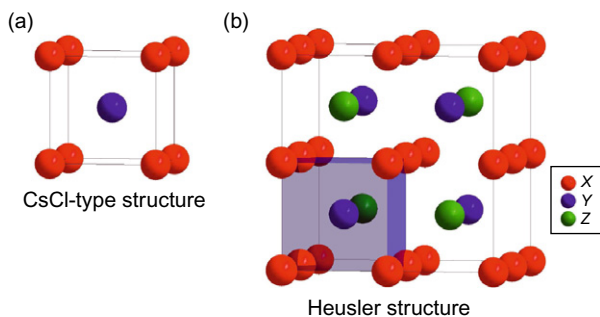
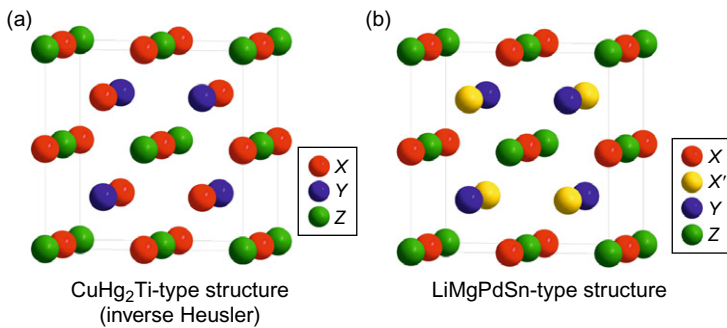


**Figure 1.3** (a) CsCl structure and (b) the Heusler structure which is shifted by  $(1/4, 1/4, 1/4)$  with respect to the standard cell to make the CsCl superstructure visible. Reprinted from Graf et al. (2011a) with kind permission of Elsevier.

frequently observed for  $\text{Mn}_2$ -based materials. A well-studied example is the compound  $\text{Mn}_2\text{CoSn}$  or  $(\text{MnCo})\text{MnSn}$  (Lakshmi et al., 2002; Surikov et al., 1990). These manganese-based materials are currently attracting considerable research activities and will be discussed in detail later. In case of quaternary Heusler compounds there are two different elements X and X'. They are located at the 4a and 4d position, respectively, Y is placed on 4b and Z on 4c. This structure has the prototype  $\text{LiMgPdSn}$ . An illustration of the inverse Heusler structure and the quaternary variant is given in Fig. 1.4.

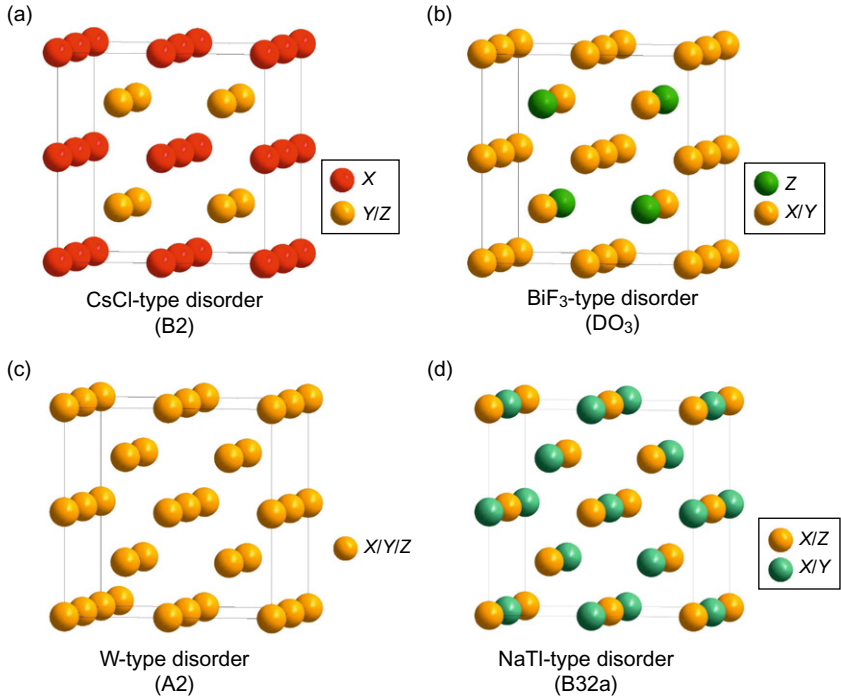
The properties of Heusler materials are strongly dependent on the atomic arrangement of the atoms. Already a partial intermixture can alter the electronic structure distinctly (Kandpal et al., 2007c; Miura et al., 2004a; Picozzi et al., 2004). As described above, Half-Heusler compounds are tetrahedrally filled structures, which are closely related to binary SCs. Covalent bonding interaction plays a significant role and their crystalline order is retained up to the composition temperature (Skovsen et al., 2010). Thus, structural disorder leading to an occupation of the vacant lattice site occurs only rarely in Half-Heusler compounds, whereas the  $\text{X}_2\text{YZ}$  phases often display considerable amounts of atomic disorder. Therefore, a careful analysis of their crystal structure is essential to understand the structure-to-property relation and to design new materials with predictable properties. Here, we will focus on disorder effects occurring in the  $\text{X}_2\text{YZ}$  materials. The interested reader is referred to Graf et al. (2011a) for further discussion of the Half-Heusler structure.

Figure 1.5 shows the transition from the ordered to the most prominent disordered Heusler structures, which will be explained in the following (Bacon and Plant, 1971; Graf et al., 2009; Webster, 1969; Webster and Ziebeck, 1988; Ziebeck and Neumann, 2001): If the Y and the Z atoms are



**Figure 1.4** (a) The inverse Heusler structure  $\text{CuHg}_2\text{Ti}$  and (b) the quaternary version  $\text{LiMgPdSn}$ . Reprinted from Graf et al. (2011a) with kind permission of Elsevier.





**Figure 1.5** Overview of the different types of disorder occurring in the Heusler structure: (a) CsCl-type disorder, (b) BiF<sub>3</sub>-type disorder, (c) NaTl-type disorder, and (d) tungsten-type disorder. Reprinted from [Graf et al. \(2011a\)](#) with kind permission of Elsevier.

evenly distributed, the 4a and 4b positions become equivalent. This leads to a CsCl-like structure, also known as B2-type disorder. As a consequence, the symmetry is reduced and the resulting space group is  $Pm\bar{3}m$ . On the other hand, the random distribution of X and Y or X and Z leads to a BiF<sub>3</sub>-type disorder (space group no. 216:  $Fm\bar{3}m$ , DO<sub>3</sub>). Different from these types of disorder, the NaTl-type structure is observed very rarely. In this structure type the X-atoms, which occupy one of the  $fcc$  sublattices, are mixed with the Y atoms, whereas the X atoms on the second sublattice are mixed with the Z atoms. This kind of disorder is also known as B32a disorder (Space group no. 227,  $Fd\bar{3}m$ ). Here, the X atoms are placed at the Wyckoff position 8a (0, 0, 0), while Y and Z are randomly distributed at position 8b (1/2, 1/2, 1/2). In contrast to these partial disorder phenomena all positions become equivalent in the tungsten-type structure with a  $bcc$  lattice and reduced symmetry ( $Im\bar{3}m$  (A2)). [Table 1.1](#) summarizes the different ordering variants of Heusler compounds. The site occupancy is

**Table 1.1** Site occupancy and general formula for different atomic order of Heusler compounds

Site occupancy	General formula	Structure type			Space group
		ICSD	SB	Pearson	
X, X', Y, Z	XX'YZ	LiMgPdSn	Y	cF16	$F\bar{4}3m$ (no. 216)
X=X, Y, Z	X <sub>2</sub> YZ	Cu <sub>2</sub> MnAl	L2 <sub>1</sub>	cF16	$Fm\bar{3}m$ (no. 225)
X, X'=Y, Z	XX' <sub>2</sub> Z	CuHg <sub>2</sub> Ti	X	cF16	$F\bar{4}3m$ (no. 216)
X=X'=Y, Z	X <sub>3</sub> Z	BiF <sub>3</sub>	DO <sub>3</sub>	cF16	$Fm\bar{3}m$ (no. 225)
X=X', Y=Z	X <sub>2</sub> Y <sub>2</sub>	CsCl	B2	cP2	$Pm\bar{3}m$ (no. 221)
X=Y, X'=Z	X <sub>2</sub> X' <sub>2</sub>	NaTl	B32a	cF16	$Fd\bar{3}m$ (no. 227)
X=X'=Y=Z	X <sub>4</sub>	W	A2	cI2	$Im\bar{3}m$ (no. 229)

The notations according to the Inorganic Crystal Structure Database (ICSD), the Strukturberichte (SB), the Pearson database, as well the space group are given.

correlated with the corresponding general formula. Different notations of the crystal structures according to the Inorganic Crystal Structure Database (ICSD), the Strukturberichte (SB), and the Pearson database, as well as the space group are given.

Figure 1.6 shows the group–subgroup relationship between all possible types of simple disorder in the Heusler structure. For comparison, the Half-Heusler structure is also included in the diagram. All disorder types, which can be found in the Heusler structure, may also occur in Half-Heusler compounds, where the vacancy is statistically distributed on all positions. Only in the CaF<sub>2</sub>-type disorder, the vacant site is preserved. The numbers behind *t* (“translationsgleich”) and *k* (“klassengleich”) specify the index of the reduction in symmetry. One should note, that there are two atoms per unit cell for the tungsten-type and the CsCl structure. For all other structure types there are 16 atoms per unit cell due the doubling of all cell axes.

### 3. SEMICONDUCTORS

Starting from the structural resemblance with silicon and binary SCs such as GaAs (III–V) and ZnSe (II–VI) one can easily design ternary semiconducting Half-Heusler compounds by distributing the eight valence electrons among three elements. Here, several subgroups have to be differentiated: The Nowotny–Juza phases A<sup>I</sup>B<sup>II</sup>C<sup>V</sup> with A<sup>I</sup>=Li, Cu, Ag, B<sup>II</sup>=Be, Mg, Zn, Cd, and C<sup>V</sup>=N, P, As, Sb, Bi are well known wide band gap SCs (Juza and Hund, 1948; Kalarasse and Bennecer, 2006; Nowotny and Bachmayer, 1950). Furthermore, the A<sup>I</sup>B<sup>III</sup>C<sup>IV</sup> (for instance

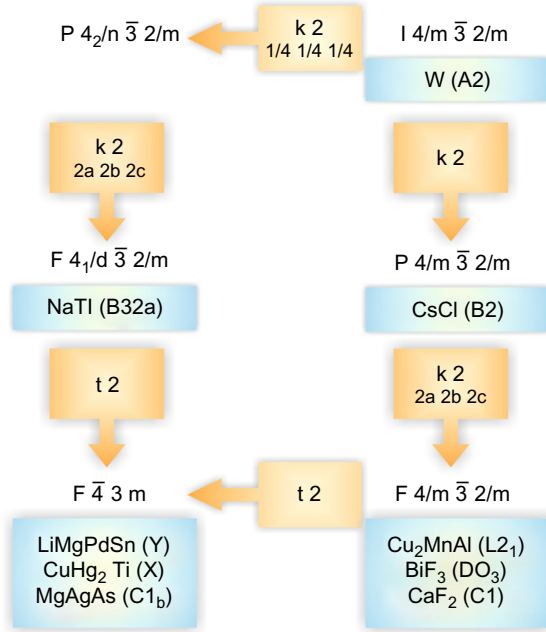


**Figure 1.6** Bärnighausen tree for Heusler compounds illustrating the group–subgroup relations between different ordering variants. The indices of *klassengleiche* (k) and *translationsgleiche* (t) as well as the unit cell transformations and the origin shifts are given. Reprinted from [Graf et al. \(2011a\)](#) with kind permission of Elsevier.

LiAlSi ([Spina et al., 2003](#)) and LiGaSi ([Nowotny and Holub, 1960](#))) and the  $A^{II}B^{III}C^{IV}$  phases (e.g.,  $Mg_2Si$ ; [Martin, 1972](#)) also belong to the group of filled tetrahedral structures. Within these eight valence electron compounds, the gap size is larger for compounds with a large Pauli electronegativity difference of the Y and Z species ([Kandpal et al., 2006b](#)) as displayed in [Fig. 1.7](#). In addition, a vast number of semiconducting compounds is obtained by replacing one main group element by a transition metal and increasing the valence electron count to 18 (e.g.,  $TiCoSb$ ,  $ZrNiSn$ , etc.). Such closed-shell 18-electron compounds ( $s^2$ ,  $p^6$ ,  $d^{10}$ ) are nonmagnetic and semiconducting ([Offernes et al., 2007](#); [Pierre et al., 1994](#); [Tobola et al., 1998](#)) as shown in [Fig. 1.7a](#), the band gap scales linearly with the average atomic number  $\langle Z \rangle = 1/N \sum_{i=1}^N Z_i$  ( $N$ , the number of atoms per unit cell) which is a good estimate for the spin–orbit coupling (SOC) strength. Indeed, the Li-containing group with low  $\langle Z \rangle$  values exhibits tunable band gaps in the optical regime as indicated by the photograph in [Fig. 1.7b](#). At rather high  $\langle Z \rangle$  values ( $>55$ ) the SOC splitting becomes strong enough to cause the interchange of the valence and conduction

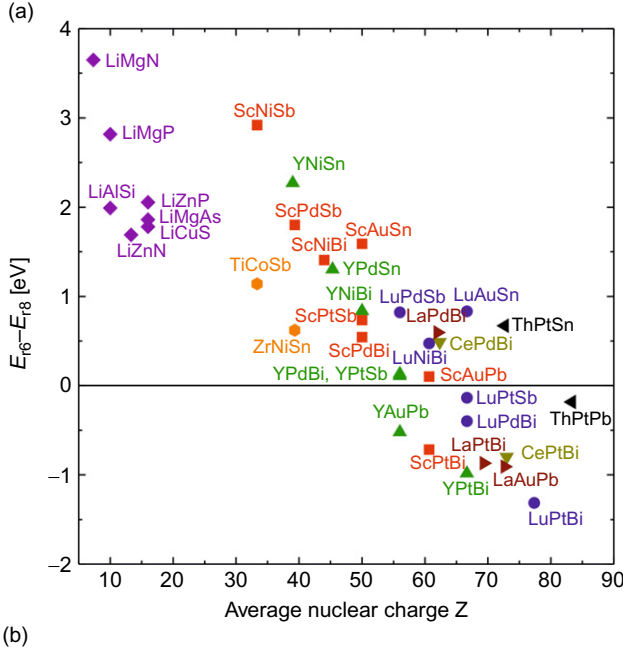


**Figure 1.7** (a) Band gaps as a function of their average nuclear charge  $\langle Z \rangle$  for various half-Heusler and Nowotny-Juza phases calculated using the optimized lattice parameter. (b) The band gap of Heusler compounds can easily be tuned within the optical spectrum by changing the chemical composition.

band symmetry characters (denoted as  $\Gamma_6$  and  $\Gamma_8$  which correspond to  $s$ - and  $p$ -type symmetries, respectively). Formally this leads to a zero-gap system, this symmetry inversion is intimately connected with a change in the band structure topology and plays a crucial role for novel adiabatic effects (anomalous Hall effect, spin Hall effect, adiabatic pumping, etc.). An interesting group of compounds is located near to the crossover point  $\langle Z \rangle$ . These borderline systems exhibit an almost linear dispersive band structure which is very close to an ideal Dirac cone, indicating their high potential as future thermoelectric (TE) materials. This group of semiconducting

materials can even be further extended to ternary RE containing Half-Heuslers, which also follow the 18-valence electron rule since the strongly localized 4f electron do not contribute to the overall valence electron count. A hexagonal variant of the Heusler structure can be found within these RE-containing compounds, the so-called LiGaGe structure. In fact, for some compositions both, the cubic and the hexagonal structure type exist, for example, the REAuSn series (Fig. 1.8).

In the class of  $X_2YZ$  Heusler compounds, only few semiconducting materials are known, which either have 18 valence electrons ( $\text{Li}_2\text{AgSb}$ ) or 24 valence electrons ( $\text{Fe}_2\text{VAl}$ ). Although this group is rather small, there are new properties to be discovered, such as extremely high electron mobilities.

### 3.1. Magnetic SCs

Over the past 40 years, the SC industry continuously shrinks the sizes of electronic components on silicon chips, increasing the performance of computers. The limit of this technology is reached when the smaller component size is prevented by the fundamental physical laws. In the past decade, spintronics has developed as a new approach that has revolutionized the market of electronic devices. Some predicted advantages of this new technology are the nonvolatility of data storage, the increased speed of data processing, the high-storage density, and the low-energy consumption. To exploit the full potential of spintronics, the development of new magnetic materials, magnetic SCs, and HMF is necessary (Felser et al., 2007). Due to their exceptional electronic structure, HMF meet all the requirements of spintronics: in these materials the electrons with one spin direction propagate like in metal and those with opposite spin behave semiconducting.

Many attempts have been made to prepare a semiconducting compound that possesses ferromagnetic properties. Mn-doped GaAs (Ohno et al., 1996) is a classical example but its Curie temperature is  $\sim 150$  K (Edmonds et al., 2002) which is still far away from being suitable for applications in electronic devices (MacDonald et al., 2005).

Therefore, the search for magnetic SCs within the Heusler compounds is a field of ongoing research. Balke et al. investigated suitable compounds that bridge both semiconducting and ferromagnetic properties in one material (Balke et al., 2008). The  $\text{C1}_b$   $\text{Ti}_{1-x}\text{Y}_x\text{CoSb}$  series ( $\text{Y} = \text{Sc}, \text{Ti}, \text{V}, \text{Cr}, \text{Mn}, \text{or Fe}$ ) were studied, both experimentally and theoretically. Band structure calculations predict semiconducting behavior for  $\text{Ti}_{0.9}\text{Sc}_{0.1}\text{CoSb}$ ,  $\text{Ti}_{0.9(0.95)}\text{V}_{0.1(0.05)}\text{CoSb}$  as well as half-metallic behavior for  $\text{Ti}_{0.9}\text{Cr}_{0.1}\text{CoSb}$ ,  $\text{Ti}_{0.9}\text{Mn}_{0.1}\text{CoSb}$  and  $\text{Ti}_{0.9(0.95)}\text{Fe}_{0.1(0.05)}\text{CoSb}$ . Semiconductivity was confirmed by electrical resistivity measurements. In particular, metallic  $\text{Ti}_{0.95}\text{Fe}_{0.05}\text{CoSb}$  undergoes a metal-to-semiconductor transition at  $\sim 210$  K. The Curie temperature of  $\text{Ti}_{0.9}\text{Fe}_{0.1}\text{CoSb}$  is estimated above 700 K. However, its precise determination is complicated since the onset

of the alloy decomposition also occurs at about the same temperature (Kroth et al., 2006). In contrast, the magnetic transition of the Cr-substituted compound occurs at low temperatures (60 K). However, the XRD measurements revealed a very small change in the lattice constant between pure TiCoSb and the Ti–Y substituted compounds. This makes this substitutional series attractive for spintronic applications like spin-LEDs or other spin-injecting devices. The growth of epitaxial thin and smooth films for devices should be readily possible. If depositing layer by layer, one can use the Co-planes to merge different materials without any destructive interfacial effects.

Recently, a promising concept based on LiZnAs was developed theoretically (Masek et al., 2007) and also demonstrated experimentally (Deng et al., 2011). In this compound it is possible to tune the magnetic properties and the electrical properties independently. This is achieved by substitution of Mn for Zn leading to ferromagnetism, and simultaneously varying the Li concentration and thus, tuning the carrier concentration to achieve semiconducting transport behavior in  $\text{Li}_{1+y}(\text{Zn}_{1-x}\text{Mn}_x)\text{As}$ . This concept can be applied to a vast number of Half-Heusler compounds, since they exhibit a vacant lattice site that can be easily occupied by dopants.

The observed magnetism of the RE containing Half-Heusler compounds is almost exclusively caused by localized 4f-electrons. Most compounds are antiferromagnetic with the low Neel temperatures or nonmagnetic (especially Lu- and La-based compounds; Szytula, 1991). The values of the effective magnetic moments  $\mu_{\text{eff}}$  are in good agreement with the values of the free  $\text{RE}^{n+}$  ions. These compounds show interesting transport and MR properties. Within the  $\text{LnNiSb}$  ( $\text{Ln} = \text{Tb}, \text{Dy}, \text{Ho}$ ) series,  $\text{NiDySb}$  and  $\text{NiTbSb}$  show a metal-insulator transition and a negative giant magnetoresistance (GMR) effect. Two main origins may give this effect: the reduction of the spin-disorder scattering due to an enhanced field-induced alignment of moments, and the reduction of the gap arising from the splitting of the up- and down-spin bands (KAR98). In contrast,  $\text{NiDyBi}$  shows a positive MR at low temperatures and fields which is explained by the extraordinary magnetoresistance (EMR) effect (Casper and Felser, 2008). Since many RE-containing Half-Heusler compounds narrow-gap SCs (Larson et al., 1999), they are perfect candidates for multifunctional topological insulators.

### 3.2. TE materials

Thermoelectric converters (TECs) for power generation aim at reducing  $\text{CO}_2$  emission via the conversion of a part of the low-grade waste heat generated by engines, industrial furnaces, gas pipes, etc. to electricity. The recovery of waste heat from the exhaust of an automotive engine, in particular, is a very attractive way for reduction of fuel consumption. TECs with high overall efficiency directly convert heat into electricity

without moving parts and thus not only decrease our reliance on fossil fuels but also actively counteract the global warming. Thus a breakthrough in the efficiency of TE materials would make a key contribution to an environmentally friendly and sustainable energy system for the coming generations.

State of the art converters are simply too inefficient to be economic, due to a combination of low efficiency values (5–10%) and expensive elementary constituents (Te, Ge, etc.). The performance of a material measured by the figure of merit  $ZT$ , where  $ZT = \sigma S^2 T / \kappa$  (with  $\sigma$  = electrical conductivity,  $S$  = Seebeck coefficient and  $\kappa$  = thermal conductivity). The biggest loss in  $ZT$  and/or efficiency while going from the raw material to the TE module is due to crucial electric and thermal contacts involved. Thinking about the assembly of a TE module and its thermal cycling to operation temperatures, the knowledge about diffusion and phase separation processes in the used TE materials becomes more and more important for the processibility and realization of the more efficient TE modules and TECs.

The large interest in this field is naturally drawn to the rich class of Heusler SCs with 18 valence electrons. Today research is especially focused on two systems which are based on  $\text{TiNiSn}$  for the  $n$ -type and  $\text{TiCoSb}$  for

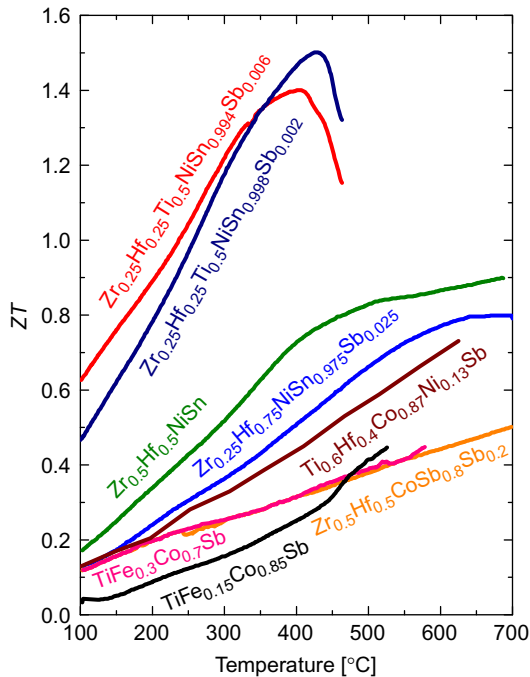


**Figure 1.8** State of the art thermoelectric merit of half-Heusler materials.

the *p*-type materials, respectively. For Sb-doped TiNiSn, power factors up to  $70 \mu\text{W}/\text{cmK}^2$  at 650 K can be reached (Bhattacharya et al., 2000). These compounds can easily be doped with other elements, thus the band structure can be changed in a simple chemical way. Nevertheless, a ZT of only 0.45 at 650 K were achieved due to the comparatively high thermal conductivity of about  $10 \mu\text{W}/\text{mK}$ . Efficient approaches to reduce the thermal conductivity based on nanostructuring were developed which enhance the phonon scattering and thus, lead to a significant decrease of the thermal conductivity by retaining the electrical conductivity and the Seebeck coefficient. This concept was recently applied to Heusler compounds (Graf et al., 2010). It is based on exploiting a phase separation of the solid solution  $\text{Mn}_{(1-x)}\text{Ti}_x\text{CoS}$  into the compounds TiCoSb and MnCoSb. EDX measurements on the two-phase material revealed the presence of size- and shape-tunable TiCoSb regions in a MnCoSb matrix. It was demonstrated that the formed phase and the grain boundaries considerably influence the phonon scattering, which leads to a reduction of the thermal conductivity by a factor of 3 compared to single phase of TiCoSb. In contrast to grinding and hot pressing approaches to introduce grain boundaries, the intrinsic phase separation has the advantage that there is no need for separate processing steps after synthesis of compounds.

One of the highest figures of merit (1.5 at 700 K) for Heusler compounds was reported by Sakurada and Shutoh for Sb-doped  $\text{Ti}_{0.50}\text{Zr}_{0.25}\text{Hf}_{0.25}\text{NiSn}$  (Sakurada and Shutoh, 2005; Shutoh and Sakurada, 2005). It should be noted that these materials also show a phase separation which is probably the key to the high ZT value. A variety of substitutions other elements were made for further optimization of the TE performance (Schwall and Balke, 2011; Sootsman et al., 2009). However, the majority of these compounds are the *n*-type TE materials. On the other hand, efficient *p*-type materials that operate at high temperatures are rare. Very recently, Yan et al. (2011) reported a 60 % ZT enhancement—compared to a highest reported value so far—with a maximum ZT—peak of 0.8 at 700 °C in  $\text{Zr}_{0.5}\text{Hf}_{0.5}\text{CoSn}_{0.8}\text{Sb}_{0.2}$ . The improvement is due a simultaneous increase in Seebeck coefficient and a significant decrease in thermal conductivity caused by the nanostructures. The samples were made by first forming alloyed ingots using arc melting and then creating nanopowders by ball milling the ingots, and finally obtaining dense bulk by hot pressing. In order to achieve the best performance of TE modules, corresponding *n*- and *p*-type materials should be designed to exhibit similar chemical and physical properties (Rowe, 2006). This can be easily realized when starting with the same parent material, for example, TiNiSn. Yang et al. (2008) have evaluated the electrical transport properties of several Heusler compounds and calculated the maximum power factors and the corresponding optimal *n*- or *p*-type doping levels which can provide guidance for future experimental work.



Ouardi et al. (2010a) investigated the substitutional series of  $\text{Ti}_{1-x}\text{M}_x\text{-NiSn}$  (where  $\text{M}=\text{Sc}, \text{V}$  and  $0 < x \leq 0.2$ ) (Ouardi et al., 2010b) and  $\text{Ti}_{0.3-x}\text{Sc}_x\text{Zr}_{0.35}\text{Hf}_{0.35}\text{NiSn}$  (where  $0 < x \leq 0.05$ ) with respect to their electronic structure and transport properties. These results show the possibility to create  $n$ - and  $p$ -type TEs with significantly high power-factors and ZTs within a single Heusler compound. Theoretical it was shown that the  $p$ -type doping (Sc) creates holes in the triply degenerate valence band at the  $\Gamma$ -point whereas the  $n$ -type doping (V) supplies electrons to the single conduction band above the indirect gap at the X-point which is typical for all semiconducting transition metal-based Half-Heusler compounds.

### 3.3. Topological insulators

Nowadays the topological insulating (TI) materials are subject to an intensive research in fundamental and applied branches of condensed matter physics (Bernevig and Zhang, 2006; Fu and Kane, 2007; Hasan and Kane, 2010; Kane and Mele, 2005; Moore, 2009; Qi and Zhang, 2010; Zhang et al., 2009a). This new quantum state of matter which leads to robust spin-polarized surface and edge states can open new directions for spintronics. Pure spin currents could be used for spin injection, for example. Therefore, we want to draw the attention of scientists working on magnetism to this new research area. However, the material base of TIs is not necessarily restricted to the main families of HgTe- and BiSe-based compounds (Bernevig et al., 2006; Chen et al., 2009; Dai et al., 2008; König et al., 2007a; Teo et al., 2008; Zhang et al., 2009b). The computational design provides the basis for the discovery of new multifunctional TIs, based on Heusler compounds and their relatives.

Many new exciting properties were predicted by theory, however only few of them were experimentally realized due to the lack of high-quality samples, single crystals, thin films and quantum well structures with well-defined charge carriers and control of both, disorder and defects. In particular, an important technological role is supposed for new multifunctional materials, such as strongly correlated, magnetic, superconducting and wide band-gap TIs suitable for the high-temperature applications, etc. The crucial role of TIs for the future quantum computing is strongly supported by the permanently increasing number of related publications (Hsieh et al., 2009; Jiang et al., 2011). Within this chapter, we would like to emphasize the potential importance of this topic also for the solid state chemists and material researchers. Indeed, bringing their experience into this branch will, with no doubt, result in a variety of new TIs and TI-based devices.

A TI can be defined as a single material which is insulating/semiconducting in the bulk (the typical band gap width does not exceed 0.3 eV) and metallic at the surface. Its surface states represent the so-called Quantum Spin Hall (QSH) (Bernevig and Zhang, 2006) state of matter consisting of

antiparallel spin-up and spin-down electron currents summing up to a dissipation less pure spin current which can be detected by transport measurements. The corresponding surface band structure forms an odd number of the two-dimensional (2D) Dirac cones in the vicinity of the Fermi energy ( $E_F$ ) which can be monitored by angle-resolved photoemission (ARPES). In contrast to TIs, graphene with four Dirac cones appears to be a topologically trivial system. The basic feature of a TI in the bulk is a finite band gap characterized by symmetry interchange of the conduction and valence bands (compared to a trivial insulator) caused by strong SOC (so-called band inversion) which occurs at the odd number of time-reversal symmetric points of the Brillouin zone corresponding to an odd number of Dirac cones. This leads to a time-reversal symmetric state of the whole system which in turn causes all miracle properties of TIs. TIs can be divided into 2D and three-dimensional (3D) (Fig. 1.9). The dimensions are not related to the crystal structures: 2D TIs are typically cubic 3D semimetals with zero bulk band gap originated from degeneration of the valence and conduction bands at the time-reversal symmetric points (see Fig. 1.9). Thus, to open a bulk gap and recover the surface QSH an additional symmetry break is required. This can be achieved by constructing composite systems, for example, quantum wells as was realized in the CdTe/HgTe/CdTe

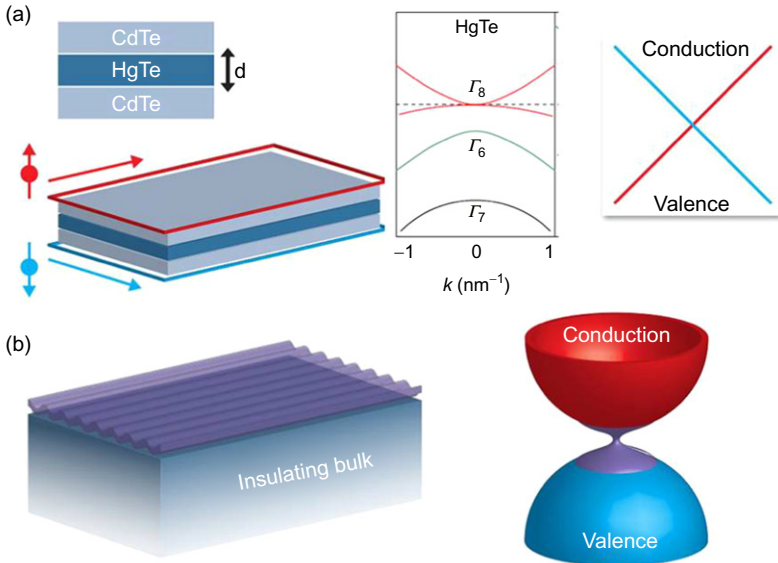


**Figure 1.9** (a) A 2D TI. Only one of the one-dimensional counter-propagating edge states is shown for each surface. (b) A 3D TI and schematic band structure with a Dirac cone.

heterostructure (König et al., 2007a). Within a certain thickness range of the HgTe layer, topological edge states were observed at the CdTe/HgTe interface (Fig. 1.9a).

3D TIs exhibit edge states on the surface of a single crystal (Fig. 1.9b) which can be easily synthesized. 3D TIs are intrinsic bulk thin-gap SCs because the band inversion takes place between two  $p$  states. In Bi<sub>2</sub>Se<sub>3</sub> and related structures 3D TI surface states in form of robust Dirac cones were observed in ARPES (Xia et al., 2009). However, the sample quality (i.e., level of disorder and number of defects) (Karla et al., 1998b) is crucial, as corresponding single crystals as well as thin films often exhibit large direct metallic conductivity which strongly dominates in comparison with the topological surface states contribution in transport measurements.

Up to now the quantum well structure in CdTe/HgTe/CdTe is the only topologically nontrivial system proven by measuring its transport properties (König et al., 2007a). A powerful tool to study and predict the TI state are *ab initio* electronic structure calculations (some of these new systems were already designed by band engineering; Heremans et al., 2008). Indeed, the direct relation between the physical functionality and the electronic structure allows to link the reciprocal space image to the real crystal structure geometry. Figure 1.10 displays the large subgroup of newly identified TI systems within the family of Heusler relatives. As described earlier in Chapter II Half-Heusler compounds can be viewed as stuffed zinc-blende versions with additional transition/RE elements occupying the octahedral vacancies (Half-Heusler (LaPtBi) and inverse Heusler structure (Li<sub>2</sub>AgSb in Fig. 1.10)) (Müchler et al., 2012). Another structure family with low symmetry are the chalcopyrites that are famous due to their low cost solar cell applications (CuIn<sub>1-x</sub>Ga<sub>x</sub>Se<sub>2</sub>). Their structure can be viewed as a doubled zinc-blende cell with a trivalent In or Ga and a monovalent Cu substituted for a divalent Zn (Fig. 1.10). Crystallization in this structure opens a finite band gap in case of the initially cubic heavy zero-gap SCs (Chadov et al., 2010; König et al., 2007b).

The typical band structure of a binary SC such as CdTe is displayed in Fig. 1.11 with  $p$ -like and  $s$ -like states marked in blue and red, respectively. The light binaries (such as ZnS and GaN) exhibit strong  $sp$ -hybridization, whereas in heavy analogues the hybridization is weaker. At the same time, the increased SOC splits the  $p_{1/2}$  and  $p_{3/2}$  states and at a certain point leads to the inversion of the conduction and valence band characters by forming a negative band gap. The typical band structure of such a heavy binary SC is shown in the vicinity of the  $\Gamma$  point in Fig. 1.11 for HgTe (up to now this is the only synthesized nontrivial heavy binary system). The negative band gap forms if the valence (the degenerated bonding  $p$ -band) and the conduction band (the nondegenerated antibonding  $s$ -band) start to overlap. In contrast to a lighter CdTe, the  $s$ -band of HgTe appears below the  $E_F$  which is fixed between the degenerated  $p$ -bands. The resulting band structure of HgTe is

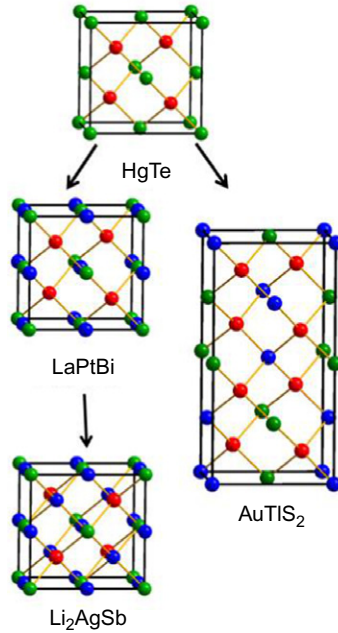


**Figure 1.10** TI candidates based on the tetrahedral symmetry. HgTe is the sparse parent compound; occupation of the tetrahedral vacancies leads to a family with an inverse  $\text{CaF}_2$  structure; filling up the octahedral vacancies leads to the family of Heuslers (LaPtBi); by adding more “stuffing” atoms to a Heusler, the so-called inverse Heusler structure is obtained ( $\text{Li}_2\text{AgSb}$ ); doubling the cubic Heusler unit cell leads to a chalcopyrite structure ( $\text{AuTlS}_2$ ).

semimetallic with a zero band gap at  $E_F$ . If the cubic symmetry is broken, SOC opens a finite band gap at  $E_F$  due to the forbidden crossing of the  $s$  and  $p$  bands.

Since the ternary XYZ Heusler class is extremely rich as mentioned above, it provides a rather wide design flexibility by tuning both, the band gap and the SOC. In addition, RE atoms induce new properties such as superconductivity or magnetism (Canfield et al., 1991; Gofryk et al., 2007; Karla et al., 1998b; Pierre and Karla, 2000) by providing various multifunctionalities. Based on the band structure calculations many of the Heusler materials which are topologically similar to HgTe were already proposed (Chadov et al., 2010). A typical example is LaPtBi, where the small electronegativity difference between Pt and Bi together with a large SOC forms a band structure very similar to for HgTe.

Band structure calculations revealed that CdTe is a topologically trivial SC with a wide band gap of 1.5 eV between the  $p$ -type valence band (blue) and the  $s$ -type conduction band (red) (Fig. 1.11). The conductance band has

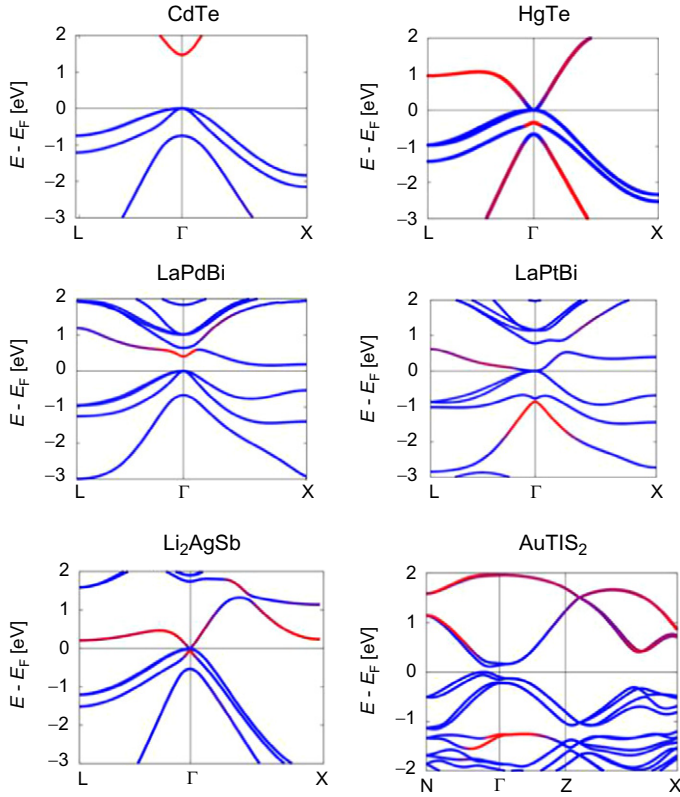


**Figure 1.11** Comparison of the electronic structure of semiconductors and semimetals within different structures types.  $s$  bands are drawn in red and  $p$  bands in blue. CdTe, HgTe, LaPdBi, LaPtBi,  $\text{Li}_2\text{AgSb}$ ,  $\text{AuTiS}_2$ .

$p$ -character at the  $\Gamma$  point. The relativistic band structure of HgTe is displayed in Fig. 1.11 which shows the band inversion of the  $s$ -states at  $\Gamma$  (red). SOC (Fig. 1.11) splits the degenerated  $p$  states into  $p_{1/2}$  and  $p_{3/2}$  components, and thereby lifts the degeneracy of the  $s$  states opening a negative band gap below  $E_F$ . The remaining cubic symmetry keeps the parabola-like  $p_{3/2}$  states degenerated which does not allow to open a real band gap. These two cases are encountered in XYZ Heusler compounds, too. Both, trivial and nontrivial topological SCs with inverted band structures can be designed by varying the average nuclear charge (i.e., the SOC) in ternary compounds. For example, LaPdBi (Fig. 1.11) with  $\langle Z \rangle = 62$  exhibits a band structure similar to CdTe ( $\langle Z \rangle = 55$ ) whereas LaPtBi ( $\langle Z \rangle = 72.66$ ) exhibits a band inversion similar to HgTe ( $\langle Z \rangle = 62$ , Fig. 1.11e). The band inversion also occurs in the “inverted” Heusler structure as displayed in Fig. 1.11 for the typical borderline example

$\text{Li}_2\text{AgSb}$  ( $\langle Z \rangle = 26$ ). Fully relativistic band structure calculations place it just at the border between trivial and nontrivial regimes (i.e., the  $s$  and the  $p$  bands are degenerated at  $E_F$ ). The latter is nothing else as the quantum critical point. A similar situation was encountered earlier in the XYZ Heusler compounds, for example, as  $\text{YPtSb}$  or  $\text{YPdBi}$  ( $\langle Z \rangle = 56$ ) (Chadov et al., 2010; Oestreich et al., 2003; Ouardi et al., 2011). The heavier compound  $\text{Li}_2\text{AuSb}$  is metallic in the bulk and  $\text{Li}_2\text{AgBi}$ , which could be a TI is not known. However, for all cubic TIs discussed here the same problem remains: The TI state can be induced only by breaking the cubic symmetry, that is, by fabricating a quantum well structure or by straining the structure on the surface. All these systems are 2D TIs. Otherwise one needs to search for new low-symmetric chemical relatives exhibiting the intrinsic TI state (i.e., the 3D TIs).

Fortunately, distorted HgTe relatives already exist, for instance within the heavy chalcopyrites. Indeed, in these materials the structural distortion lifts the degeneracy of the  $p$  states at the  $E_F$  and opens a finite band gap ( $\text{AuTlSe}_2$ ) and the system becomes a 3D TI. We would like to emphasize that the band inversion is the necessary condition for the formation of a TI, while the parity change is the sufficient condition as sketched in Fig. 1.12. The parity change is caused by the band inversion between the  $s$  and  $p$  states. The bonding and antibonding  $s$  bands have positive and negative parity, respectively. The bonding  $p$  state carries the negative parity whereas its antibonding counterpart is positive. Inverting the antibonding  $s$  with the bonding  $p$  band leads to bonding below  $E_F$  and the parity changes. This analysis must be performed in all time-reversal symmetric points of the Brillouin zone. In case of  $\text{Bi}_2\text{Se}_3$  the parity change caused by inversion of the Bi and Se  $p_x$  bands is discussed in Zhang et al. (2009a). Another example are the skutterudites with a  $d$ - $f$  inversion (Yan et al., 2012).

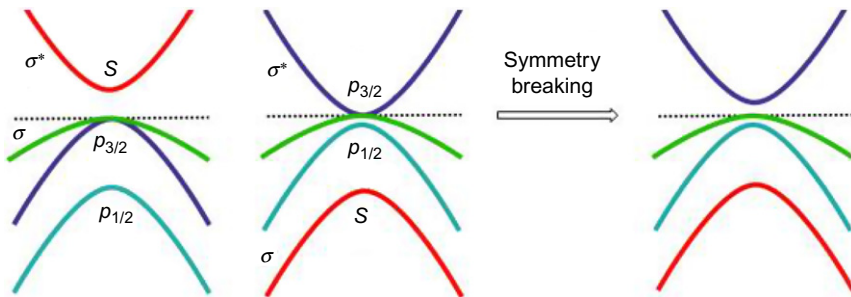


**Figure 1.12** Change in bonding of the molecular orbitals at the  $\Gamma$  point for the trivial semiconductor  $\text{Cu}_2\text{Se}$  (left) and the nontrivial semiconductor  $\text{Ag}_2\text{Te}$  (right). The BI of the  $s$  and  $p$  bands leads to a change of parity. Due to symmetry breaking a bulk band gap opens and the band inversion remains.

## 4. THE SLATER–PAULING RULE

In general, simple electron counting rules help to understand the electronic and magnetic properties of Half-Heusler and Heusler compounds (Graf et al., 2011a). An important electron counting rule for magnetic Heusler compounds is the so-called Slater–Pauling rule.

Slater and Pauling discovered that the magnetic moment  $m$  of the 3d elements and their binary alloys can be estimated on the basis of the average valence electron number ( $n_V$ ) per atom (Pauling, 1938; Slater, 1936a). The materials are divided into two areas depending on  $m(n_V)$ : The first area of the Slater–Pauling curve is the area of low valence electron concentrations ( $n_V \leq 8$ ) and of localized magnetism. Here, mostly *bcc* and *bcc* related structures are found. The second area is the area of high valence electron concentrations ( $n_V \geq 8$ ) and of itinerant magnetism. In this area, systems with closed packed structures (*fcc* and *hcp*) are found. Iron is located at the borderline between localized and itinerant magnetism. Figure 1.13b shows the Slater–Pauling curve for transition metals and some alloys. Heusler compounds are situated in the localized part of this curve. Therefore, we focus on this area of the curve. The magnetic moment in multiples of Bohr magnetons  $\mu_B$  is given by

$$m = n_V - 2n_{\downarrow} \quad (1)$$

where  $2n_{\downarrow}$  denotes the number of electrons in the minority states. The minimum in the minority density of states forces the number of electrons in the *d* minority band to be approximately three. Neglecting the *s* and *p* electrons, the magnetic moment in the localized area of the Slater–Pauling curve can be calculated according to

$$m \approx n_V - 6 \quad (2)$$

which means that the magnetic moment per atom is just the average number of valence electrons minus six. HMF exhibit per definition a band gap in the minority density of states at the Fermi level. Due to this band gap, the number of occupied minority states needs to be an integer, which is exactly fulfilled for the case  $m = n_V - 6$  (Kübler, 2000; Wurmehl et al., 2005). This rule may lead to noninteger values, if the average valence electron concentration is not integer. Thus, it is often more convenient to use the valence electron number per formula unit  $N_V$ .

For Half-Heusler compounds with three atoms per formula unit, the Slater–Pauling rule is given by

$$m_{XYZ} = N_V - 18 \quad (3)$$

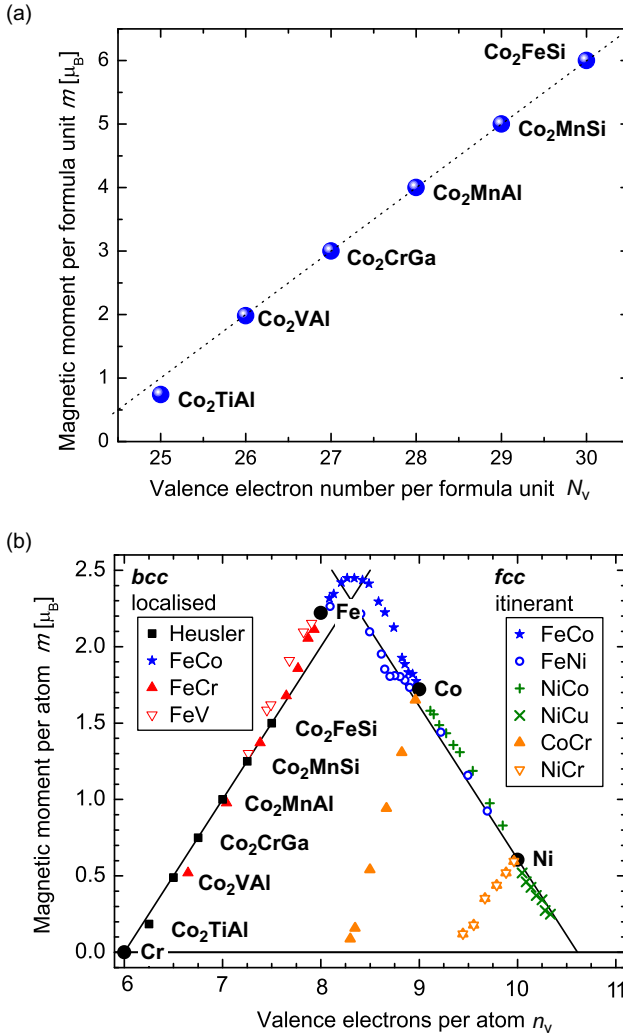


**Figure 1.13** (a) The magnetic moment per formula unit of  $\text{Co}_2$ -based Heusler compounds is proportional to the number of valence electrons and follows the Slater-Pauling curve, which is illustrated in (b). The values for 3d transition metals and their alloys are given for comparison. (Note: the  $A_{1-x}B_x$  alloys are given as  $AB$  in the legend for shortness.) Reprinted from [Graf et al. \(2011a\)](#) with kind permission of Elsevier.



In the case of  $X_2YZ$  Heusler materials, there are four atoms per unit cell leading to the formula

$$m_{X_2YZ} = N_V - 24 \quad (4)$$

The magnetic moment as function of the number of valence electrons per formula unit is shown in Fig. 1.13.

We would like to emphasize that, besides very few exceptions, magnetic Half-Heusler compounds are only stable for a valence electron number of 22 with Mn or a RE element on the octahedral lattice site, which can be attributed to the high tendency towards a localized magnetic moment of Mn as described by Kübler et al. (1983). This Kübler rule plays an important role in all Heusler compounds. The oxidation state of the localized Mn atoms can be formally described to be  $Mn^{3+}$  with a  $d^4$  configuration giving rise to a magnetic moment of approximately  $4 \mu_B$ . The localized magnetic moment of Mn is also represented in the calculated spin density distribution of MnNiSb displayed in Fig. 1.14.

Deviating from 22 valence electrons mostly results in the formation of a different crystal structure, for example, MnCrSb, FeMnSb and  $Mn_2Sb$  do not crystallize in the Half-Heusler structure (de Groot, 1991; de Groot et al., 1986). A detailed list of magnetic moments located at the Mn–Y site is given in Kübler et al. (1983).

The magnetic moment of half-metallic Heusler materials scales linearly with the number of valence electrons according to  $m = N_V - 24$  as shown in Fig. 1.13. Only a few of them with  $N_V \leq 24$  are known, for example,  $Mn_2VAl$  which is a HMF with 22 valence electrons (Weht and Pickett, 1999). Substituting Co for half on the Mn atoms on the X position, results in nonmagnetic  $(Co_{0.5}Mn_{0.5})_2VAl$  with 24 electrons (Galanakis and Dederichs, 2005). This example shows, that the Slater–Pauling rule is also valid for quaternary Heusler compounds (Alijani et al., 2011a,b, 2012).

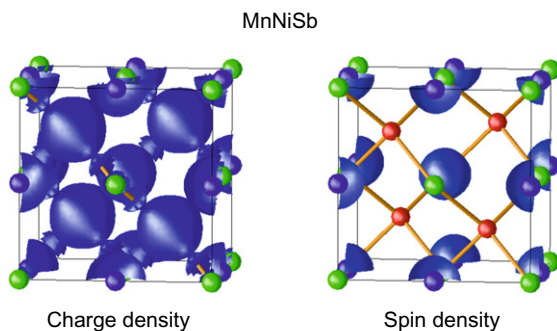


**Figure 1.14** Charge and spin density distributions of MnNiSb. Reprinted from Graf et al. (2011a) with kind permission of Elsevier.

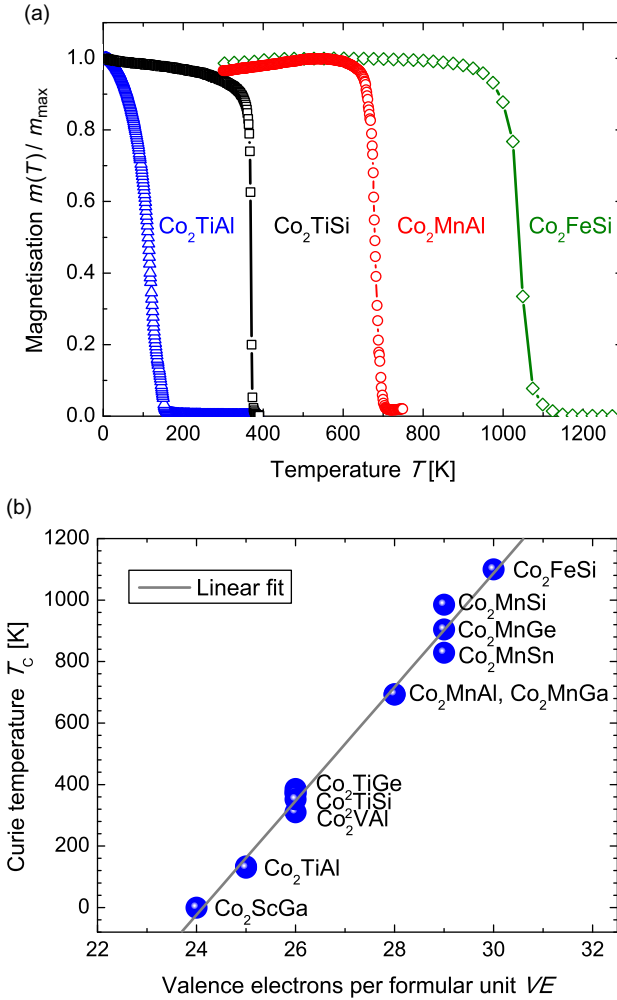


**Figure 1.15** (a) Temperature-dependent magnetization measurements of selected  $\text{Co}_2$ -based Heusler compounds (Balke et al., 2010) and (b)  $T_C$  of  $\text{Co}_2$ -based Heusler compounds are linearly dependent on the number of valence electrons. Reprinted from Graf et al. (2011a) with kind permission of Elsevier.

Additionally,  $T_C$  of  $\text{Co}_2$ -based Heusler compounds show a linear dependency on the magnetic moment (Wurmehl et al., 2006a). Due to the Slater–Pauling behavior of the magnetic moments,  $T_C$  follows a linear trend, when viewed as a function of valence electrons, as displayed in Fig. 1.15. The linear trend is interrupted for materials with  $N_V = 27$ . Theoretical studies revealed, that the magnetic moments on the Co and on the Y sites increase simultaneously with  $N_V$ , which leads to a nonlinearity with  $m$ . This is compensated

by changes in the Heisenberg exchange average resulting in a linear dependency on  $N_V$  (Fecher et al., 2006; Kübler et al., 2007). It should be noted that the magnetization as a function of temperature drops very slowly. For  $\text{Co}_2\text{MnSi}$  a reduction of less than 1% is observed when changing the temperature from 5 K to RT. Up to now,  $\text{Co}_2\text{FeSi}$  is the Heusler compound with the highest magnetic moment of  $5.97 \mu_B$  at 5 K and a  $T_C$  of 1100 K, the highest  $T_C$  for a HMF (Wurmehl et al., 2006a,c).

## 5. HALF-METALLIC FERROMAGNETS

At the beginning of the 1980s, the interest in fast and nonvolatile mass storage memory devices raised tremendous research activity in the field of magneto-optics. Almost all existing magnetic solids were studied with regard to the magneto-optic Kerr effect (MOKE), leading to a maximum MOKE rotation of  $1.27^\circ$  of  $\text{MnPtSb}$  (van Engen et al., 1983). This result motivated the investigation of the electronic structure of  $\text{MnPtSb}$  and the isoelectronic Heusler compounds  $\text{MnNiSb}$  and  $\text{MnPdSb}$ , which lead to the prediction of  $\text{MnNiSb}$  as the first material being a HMF by de Groot and coworkers in 1983 (de Groot et al., 1983; Helmholdt et al., 1984). Indeed, many authors have verified this prediction in the mean time (Galanakis et al., 2000; Kübler, 1984; Kulatov and Mazin, 1990; Wang et al., 1994; Youn and Min, 1995). Several explanations for both the electronic structure and the band gap have been given, in terms a Ni–Mn interaction only, but these considerations did not clarify why the octahedral coordination of manganese is essential for the evolution of half-metallic ferromagnetism (Galanakis et al., 2002). However, Kübler summarized the chemical bonding, in relation to the band gap, as a nickel-induced Mn–Sb covalent interaction (Kübler, 2000). According to theoretical calculations, a minority band gap, located within the larger gap of the NiSb substructure is formed from the  $d$  states (Kandpal et al., 2005). The spin-polarized states at the Fermi energy strongly exhibit Mn character.

A 100% spin polarization for bulk  $\text{MnNiSb}$  was confirmed by polarized positron annihilation experiments and inverse photoemission (Hanssen and Mijnders, 1986; Hanssen et al., 1990; Kirillova et al., 1995). The surfaces, however, do not show half-metallicity, which can partly be explained by the observation of manganese segregations on the surface and its high affinity to oxygen (Bona et al., 1985; Ristoiu et al., 2000a,b; Soulen et al., 1999) but maybe also by the general tendency of antimony to build surface segregations. But even for noncontaminated surfaces, a genuine half-metallic character was not observed (Galanakis, 2002; de Wijs and de Groot, 2001). This underlines again the sensitivity of half-metallic properties to the crystal structure.

The transport properties of  $\text{MnNiSb}$  were studied thoroughly and electrical resistivity data revealed a phase transition at approximately 90 K (Borca et al., 2001; Hordequin et al., 2000; Otto et al., 1989). One possible

explanation for this phase transition is the occurrence of thermal excitations, if the Fermi energy is positioned close to a band edge. A crossing of a magnon and a phonon branch, at an energy corresponding to 80 K, was also discussed in this context (Hordequin et al., 1997a,b). A final understanding of the phase transition, however, is still missing. The local magnetic moments of Mn and Ni were examined using magnetic circular dichroism, and revealed that the major portion of the magnetic moment is located at the Mn site. A reduction of both, the manganese and nickel moments around 80 K was observed indicating a loss of coupling between Mn and Ni (Borca et al., 2001). Additionally, the disappearance of the Ni moment at the transition temperature was also found by computational studies (Lezaic et al., 2006). Interestingly, none of these anomalies was observed in the spontaneous magnetization of bulk MnNiSb (Otto et al., 1989).

The compounds MnPtSb and MnPdSb are isoelectronic to MnNiSb, and therefore, their electronic structures are similar. The main difference is the higher nuclear charge of Pd and Pt with respect to Ni. Therefore, relativistic effects leading to an energy shift of the minority spin electrons have to be taken into account when calculating the band structure of these compounds (Wijngaard et al., 1989). These effects also provide an understanding for the differences in the MOKE measurements for MnNiSb and MnPtSb (Kulatov et al., 1995). In the case of MnPdSb, the Fermi level intersects at the top of the valence band, but further calculations are needed to clarify, if it is a HMF or not. Maybe correlation effects have to be taken into account since very small effects alter the spin polarization considerably. On the other side, MnPtSb is half-metallic, but in contrast to Ni, Pt does not carry any magnetic moment and no magnetic anomalies are expected. Angular-resolved photoemission measurements on MnPtSb single crystals yielded good agreement with the calculated band structure, which is remarkable, since the ground state in the experiment deviates from the occupations used for the eigenvalue calculation in density-functional theory (Kisker et al., 1987).

If other than isoelectronic elements are substituted in MnNiSb, the total valence electron number has to be kept constant ( $N_V = 22$ ), as discussed above. MnAuSn is also a HMF but it is not as intensively investigated as MnNiSb (Casper et al., 2006; Ksenofontov et al., 2006a; Offernes et al., 2003). Mn cannot be replaced by other transition metals in the formal oxidation state  $3+$ , since this leads to the formation of a different crystal structure. In fact, all Half-Heusler compounds, which are known with  $X = \text{RE}$  elements, are also known for  $X = \text{Mn}^{3+}$ . However, in the RE-containing materials, correlation effects have to be considered to describe their electronic structure correctly (Casper et al., 2009). Therefore, the following question needs to be solved in future: What is so special about  $\text{Mn}^{3+}$  and are these materials strongly correlated?

Theoretical calculations predicted MnCoSb to be a HMF with a reduced magnetic moment of  $3 \mu_B$  (Kübler, 1984). Experimental results,

however, demonstrated that MnCoSb crystallizes in a cubic superstructure with doubled lattice parameter and Co displacements (Ksenofontov et al., 2006b). This structure can be illustrated by alternating MnSb and Co<sub>2</sub>MnSb cells. The magnetic moment is 3.8  $\mu_B$  and consequently, MnCoSb is not a HMF. Unfortunately, pure MnFeSb does not exist, and only a substitution of up to 10% of Fe for Ni retains the Half-Heusler structure (de Groot et al., 1986). The compounds MnFeSb, MnMnSb and MnCrSb do not exist in the Half-Heusler structure, they form antiferromagnetically ordered materials with a Cu<sub>2</sub>Sb-type crystal structure.

A different route to induce half-metallic ferromagnetism in Half-Heusler compounds is provided by electron doping of semiconducting TiCoSb resulting in a dilute magnetic SC (Balke et al., 2008). The partial replacement of Ti by Cr or Fe (10%) converts the SC TiCoSb into a HMF. Both, calculations and experiments indicate that only the atoms replacing Ti contribute to the total magnetic moment, which is in good agreement with the magnetic sublattice located at the octahedral positions. For the Cr-containing material, the experimental magnetic moment is distinctly smaller than expected from calculations, which can be explained by partial antiferromagnetic coupling of the Cr atoms. Since the  $T_C$  of these materials are well above RT (700 K for Ti<sub>0.9</sub>Fe<sub>0.1</sub>CoSb), these are interesting materials for future applications in magnetoelectronics and spintronics.

In the very same year as the discovery of half-metallicity in MnNiSb by de Groot and coworkers, in 1983, *ab initio* calculations performed by Kübler et al. revealed that the density of states of the ferromagnetic L2<sub>1</sub> Heusler compounds Co<sub>2</sub>MnSn and Co<sub>2</sub>MnAl nearly vanishes for one spin direction at the Fermi energy ( $\epsilon_F$ ) resulting in a high spin polarization. They concluded that this leads to peculiar transport properties (Kübler et al., 1983). Indeed, these results were verified by many authors and extended to a large group of Co<sub>2</sub>-based Heusler compounds (Block et al., 2003; Fujii et al., 1990; Kandpal et al., 2007a; Kurtulus et al., 2005a,b; Picozzi et al., 2004; Wurmehl et al., 2005).

One design recipe for new HMF with L2<sub>1</sub> structure developed by Butler is fairly simple (Butler et al., 2011): Alloys with B2-type structure that are found in the localized part of the Slater–Pauling curve can be combined to form a L2<sub>1</sub> ordered Heusler compounds. For instance, the combination of binary FeTi and FeAl results in the HMF Fe<sub>2</sub>TiAl. However, the story of success of Heusler compounds in spintronics started with Co<sub>2</sub>Cr<sub>0.6</sub>Fe<sub>0.4</sub>Al (CCFA). The idea behind this material was the combination of a large band gap in the minority density of states with a large density of states (van Hove singularity) in the majority states. The appearance of a van Hove singularity at or close to  $\epsilon_F$  is an important requirement for a stable HMF insensitive to disorder (Felser et al., 1999). The same fingerprint is also observed in many colossal magnetoresistive (CMR) compounds with high spin polarization (Felser et al., 1999; Felser and Seshadri, 2000). Band structure calculations

revealed that this is fulfilled for  $\text{Co}_2$ -based Heusler compounds with 27.8 or 28.5 valence electrons and that, in these cases,  $\epsilon_F$  is located in the middle of the minority band gap which makes the HMF state stable against temperature fluctuations (Balke et al., 2006; Block et al., 2003). This noninteger number of valence electrons can, among others, be implemented by quaternary alloys of the  $\text{Co}_2\text{Y}_{1-x}\text{Y}'_x\text{Z}$  or  $\text{Co}_2\text{YZ}_{1-x}\text{Z}'_x$  types.

Due to the rather disappointing results with Heusler compounds in the early days of GMR multilayers, there were only a few groups working in this area. Interest in Heusler compounds grew enormously with the discovery of a high MR effect in CCFA together with its success in tunnel magnetoresistance (TMR) devices. Band structure calculations assuming ordered compounds  $\text{Co}_2\text{CrAl}$  and CCFA predicted a full spin polarization at  $\epsilon_F$  (Block et al., 2003). In case of CCFA a peak in the density of states indicates a half-metallic ferromagnetic state with a van Hove singularity in the majority channel near  $\epsilon_F$  and a band gap in the minority channel. Due to this special band structure,  $\text{Co}_2\text{Cr}_{0.6}\text{Fe}_{0.4}\text{Al}$  was a promising candidate for a high MR ratio. Indeed, in powder pellets a high MR ratio of 30% was observed in a low external magnetic field of 0.1 T at RT (Block et al., 2003). This was the starting point for extensive investigations to gain an understanding of the extraordinary electronic structure of CCFA.

To confirm the initial assumption band structure calculations proved the half-metallic ferromagnetism occurring in the Cr-rich compounds (Fecher et al., 2005; Galanakis et al., 2002; Miura et al., 2004a; Wurmehl et al., 2006b). For example, Zhang et al. found that  $\text{Co}_2\text{CrAl}$  is a HMF with  $3 \mu_B$  in agreement with the Slater–Pauling rule (Zhang et al., 2004). However, the substitution of Cr for Fe results in a loss for half-metallic ferromagnetism in  $\text{Co}_2\text{Cr}_{(1-x)}\text{Fe}_x\text{Al}$  for  $x \geq 0.625$  (Kobayashi et al., 2004). The replacement of Cr by Fe can be understood as an electron doping that leads to a shift of the van Hove singularity relative to  $\epsilon_F$ . This circumstance opens the possibility to tune the electronic properties according to different demands. However, it has to be noted that such a simple rigid band model is often too trivial to describe the results of such a doping procedure (Fecher et al., 2005; Wurmehl et al., 2006b). On the other side, band structure calculations for the disordered compound verified a distinct reduction of the magnetic moment and a loss of half-metallic ferromagnetism. Applying the coherent potential approximation (CPA), Miura et al. studied the consequences of disorder on the electronic and magnetic properties of  $\text{Co}_2\text{Cr}_{(1-x)}\text{Fe}_x\text{Al}$  (Miura et al., 2004a). They found that the complete spin polarization is retained up to 10% of CsCl-type disorder, while a stronger reduction of the spin polarization occurs for the other types of disorder. Using single point contacts a spin polarization of 81% was measured (Clifford et al., 2004). Galanakis investigated, in addition to the bulk properties, the influence of surface states on the half-metallic properties of Heusler compounds and reported, that the CrAl-terminated surface of

$\text{Co}_2\text{CrAl}$  behaves differently compared to most other Heusler alloys, that is, that the half-metallic properties are preserved (Galanakis, 2004).

Experimental data of  $\text{Co}_2\text{CrAl}$  reveal a magnetic moment of  $1.56 \mu_{\text{B}}$  per formula unit, as already observed by Buschow and Van Engen (Buschow and van Engen, 1981). It was assumed, that the magnetic moment is mainly carried by the Co atoms, while the contribution of Al and Cr is small. According to recent band structure calculations, all constituents of the compound should carry a magnetic moment:  $0.77 \mu_{\text{B}}$  per Co atom,  $1.63 \mu_{\text{B}}$  per Cr atom and  $-0.10 \mu_{\text{B}}$  per Al atom. Consequently, a value of  $3 \mu_{\text{B}}$  is then expected for the total magnetic moment in agreement with the Slater–Pauling rule. The element specific investigation of magnetic moments has turned out to be a useful tool to discriminate different types of disorder (Elmers et al., 2003). However, the comparison of experimental data and calculations reveals that atomic disorder on lattice sites is the biggest drawback for the production of HMF, especially for thin films. Unfortunately, the preparation of well-ordered  $\text{Co}_2\text{Cr}_{(1-x)}\text{Fe}_x\text{Al}$  films is extremely difficult. The reason for the reduced magnetic moment and the problem of disorder, especially in Cr–Al-containing compounds is their sensitivity against oxygen, which might trigger disorder and phase separation effects.

Although the family of  $\text{X}_2\text{YZ}$  Heusler compounds is very large, there are only few compounds that exhibit half-metallic ferromagnetism and are not based on  $\text{X} = \text{Co}$ . Only recently, it was discovered that the  $\text{MnYZ}$  are ferrimagnetic half-metals (see Section 7 for a detailed discussion). The first authors to report on experiments with Co-based materials were Webster and Ziebeck (Webster, 1971; Webster and Ziebeck, 1973). Since that time, especially the Co- and Mn-based compounds evoked great interest due to their high Curie temperatures.

As already stated above, the electronic structure plays an important role for the determination of magnetic properties and the prediction of HMF. Therefore, band structure calculations need to be carried out carefully and all approximations need to be considered when the results are discussed.

Unfortunately, the first efforts to calculate the band structure of  $\text{Co}_2\text{MnSn}$ ,  $\text{Co}_2\text{TiSn}$ , and  $\text{Co}_2\text{TiAl}$  did not yield half-metallic ferromagnetism (Ishida et al., 1982). Instead, the calculations showed a crossing of the minority bands at  $\epsilon_{\text{F}}$  although a minimum of the density of states at the Fermi level was observed. At that time, the calculations were based on a spherical potential, and the exchange correlation of the local spin density approximation (LSDA) was used in a rather simple form (von Barth and Hedin, 1972; Hedin and Lundqvist, 1971; Kohn and Sham, 1965). The first clear indications of half-metallic ferromagnetism were found by Ishida et al. for  $\text{Co}_2\text{MnZ}$  and  $\text{Ru}_2\text{MnZ}$  ( $\text{Z} = \text{Al}, \text{Si}, \text{Sn}, \text{Sb}$ ) (Ishida et al., 1995a,b). Mohn et al., on the other hand, found a magnetic ground state for  $\text{Co}_2\text{TiZ}$  ( $\text{Z} = \text{Al}, \text{Sn}$ ) by a full-potential method, however, no half-metallic ground state was revealed (Mohn et al., 1995). Galanakis et al. reported half-metallic



ferromagnetism in different  $\text{Co}_2\text{YZ}$  compounds, but not for Co-based ones with  $\text{Y}=\text{Ti}$  or  $\text{Fe}$  (Galanakis et al., 2002). Their results are in good agreement with the results by Picozzi et al. who used a generalized gradient approximation (GGA) correction instead of pure LSDA (Picozzi et al., 2002). The GGA by Perdew et al. does not only consider the exchange correlation potential of the local density approximation, like in pure LSDA, but additionally its gradient (Perdew et al., 1992, 1996, 1997; Perdew and Yue, 1986). It was not possible to verify the half-metallic ferromagnetism in  $\text{Co}_2\text{FeAl}$  using a spherical potential and GGA (Antonov et al., 2005; Miura et al., 2004a). GGA calculations with a full potential, however, yield a half-metallic ground state for the complete substitution series  $\text{Co}_2\text{Cr}_{(1-x)}\text{Fe}_x\text{Al}$  (Fecher et al., 2005). This illustrates, that the correct electronic ground state is only obtained, if the full potential and the GGA are taken into account.

Based on these results, the properties of Co-based Heusler compounds were calculated, leading to the result that most Co-based compounds follow the Slater–Pauling rule (compare Fig. 1.13). The question, however, in which way the electrons have to be distributed for the formation of a HMF, remains to be solved. The  $s$  and  $p$  electrons do not contribute to the magnetic moment, they are fully delocalized. The  $d$  electrons, however, are sufficiently localized to be attributed to specific atoms. For the compounds  $\text{Co}_2\text{Y}$  ( $\text{Y}=\text{Sc}, \dots, \text{Fe}$ ),  $\text{Z}=\text{Al}, \text{Si}$ ) approximately 7.5  $d$  electrons are localized at Co, that is, Co has approximately a  $d^{7.5}$  configuration (Kandpal et al., 2007a). On the other side, the number of  $d$  electrons at Y increases linearly with the atomic number. The magnetic moment at the Co position is  $\approx 1 \mu_B$  for  $\text{Co}_2\text{YSi}$  with  $\text{Y}=\text{Ti}, \dots, \text{Mn}$  and a little bit lower for  $\text{Co}_2\text{YAl}$  with  $\text{Y}=\text{V}, \dots, \text{Fe}$ . In both cases, the Y elements Ti and Sc do not contribute to the magnetic moment, independent of Z. The total magnetic moment, however, follows the Slater–Pauling rule, which means that the Co moment is reduced for a lighter transition metal Y. The moment at the Co site needs to increase for  $\text{Co}_2\text{FeSi}$  to achieve the total magnetic moment of  $6 \mu_B$ . These relations are illustrated in Fig. 1.16. Regrettably, for this compound a wrong result is obtained by LSDA–GGA calculations, even with the full potential. The behavior of the Co magnetic moments ( $\approx 1 \mu_B$ ) illustrate that the Co–Co interaction plays a crucial role for half-metallic ferromagnetism. On the contrary, this interaction is absent in case of Half-Heusler compounds.

To explain the properties of  $\text{Co}_2\text{FeSi}$ , a partial localization and correlation of  $d$  electrons needs to be considered. The relative relevance of itinerant compared to localized magnetism of  $d$  electrons in intermetallic alloys was already discussed by Slater (1936a,b), van Vleck (1945, 1953), and Goldmann (1953). Particularly, a localization of the  $d$  electrons in Heusler compounds is unquestioned as already mentioned by Pauling for  $\text{Cu}_2\text{MnAl}$  (Pauling, 1938). However, the following question needs to be answered: To which extent do the Coulomb interactions between the  $d$  electrons



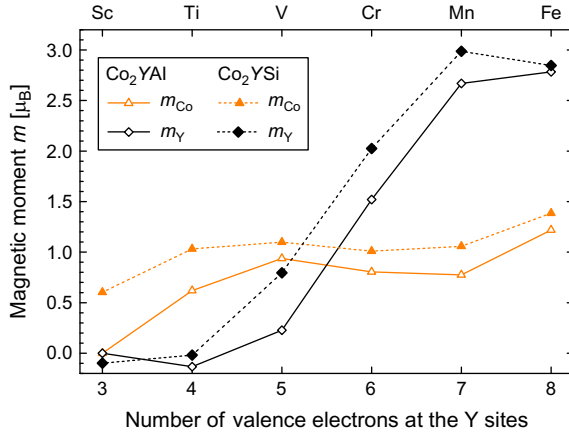


**Figure 1.16** Element specific magnetic moments in  $\text{Co}_2\text{YZ}$  ( $Z = \text{Al}, \text{Si}$ ). Shown is the evaluation of the local moments at the Co and Y = Sc, Ti, V, Cr, Mn, and Fe sites as a function of the valence electron number at the Y sites. Data taken from [Kandpal et al. \(2007a\)](#) and reprinted from [Graf et al. \(2011a\)](#) with kind permission of Elsevier.

persist, despite the increasing screening effect by delocalized electrons, so that as a result a conservation of important atomic properties, such as Hund's rule is achieved ([Flude, 1995](#))?

To answer this question, calculations with the LDA + U method, which is the simplest and most popular method to incorporate electron–electron correlations on transition metal positions, were performed ([Anisimov et al., 1997](#); [Kandpal et al., 2006a](#)). The LDA + U method takes the orbit dependency of the Coulomb and exchange interaction into account, which are, on the other hand, not considered in a pure LSDA calculation. The effective Coulomb exchange interaction,  $U_{\text{eff}} = U - J$ , was used to correct for the double counted terms.  $U$  and  $J$  correspond to the exchange and the Coulomb integral, respectively. [Figure 1.17](#) compares the spin-resolved band structure of  $\text{Co}_2\text{FeAl}$  calculated in the LSDA – GGA and the LDA + U approach ([Fecher and Felser, 2007](#)). It can be seen, that the inclusion of  $U_{\text{eff}}$  in the calculation does not cause pronounced changes in the majority bands. Even the flat band at  $\approx 4$  eV below  $\epsilon_F$  is only shifted by 200 meV to higher binding energies. This is remarkable, since this band is mainly responsible for the localized magnetic moment at the Fe atom. However, the major impact of the Coulomb parameter is found in the minority bands, and, in particular, on their unoccupied part. The gap is clearly opened up and the flat, lowest conduction bands at the  $\Gamma$  point are shifted by  $\approx 1$  eV to higher energies.

Additional calculations were performed for the series  $\text{Co}_2\text{Mn}_{(1-x)}\text{Fe}_x\text{Si}$  ( $0 \leq x \leq 1$ ) by [Kandpal et al. \(2006a\)](#). Independent of the Fe concentration

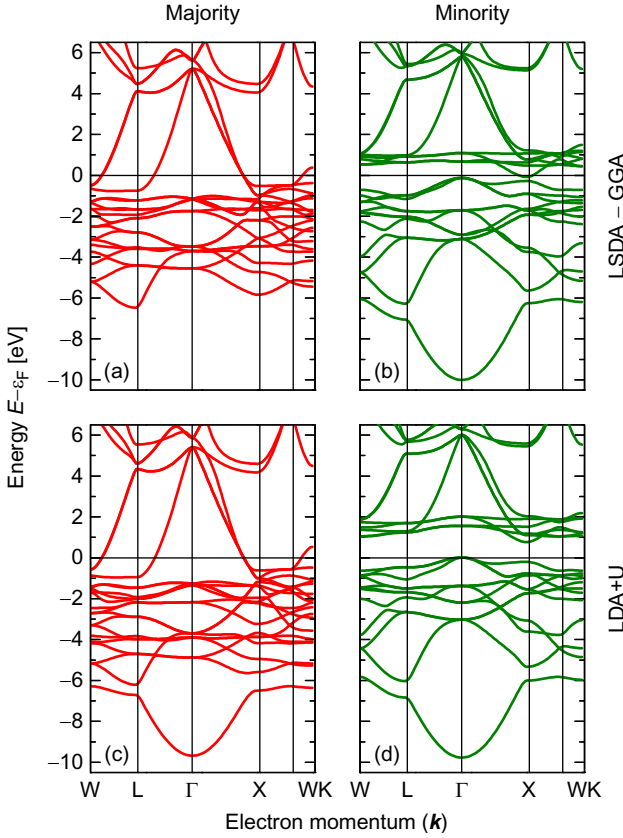


**Figure 1.17** Spin-resolved band structure of  $\text{Co}_2\text{FeAl}$ . Compared are the band structures calculated in the LSDA-GGA (a, b) and the LDA+U (c, d) approaches. Data taken from [Fecher and Felser \(2007\)](#) and reprinted from [Graf et al. \(2011a\)](#) with kind permission of Elsevier.

$x$ , the following values were chosen for  $U_{\text{eff}}$ :  $U_{\text{Co}} = 1.9$ ,  $U_{\text{Fe}} = 1.795$ , and  $U_{\text{Mn}} = 1.768$  eV. Previous results showed, that the experimental magnetic state of  $\text{Co}_2\text{MnSi}$  and  $\text{Co}_2\text{FeSi}$  is well describe with exactly these semiempirical values within the LDA+U method. The values correspond to those for the Coulomb interaction  $U_{\text{dd}}$  between d electrons in elemental 3d transition metals, determined by Bandyopadhyay and Sarma already prior to the introduction of the LDA+U method ([Bandyopadhyay and Sarma, 1989](#)).

The curve for the magnetic moment  $m$  as a function of the iron concentration  $x$ , obtained by LDA+U calculations, matches well with the experimental data as shown in [Fig. 1.18](#). A shift of  $\epsilon_{\text{F}}$  within the

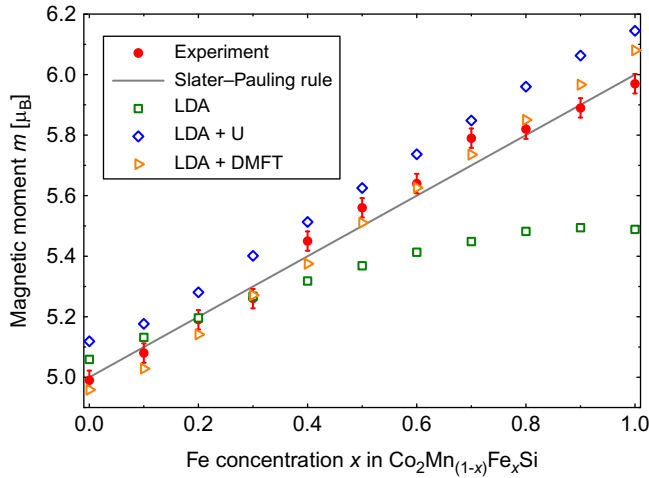


**Figure 1.18** Comparison of the total magnetic moments for  $\text{Co}_2\text{Mn}_{(1-x)}\text{Fe}_x\text{Si}$  calculated within LDA (open squares), LDA + U (open diamonds) and LDA + DMFT (open triangles) with the results of the SQUID magnetic measurements (filled circles). Data taken from [Chadov et al. \(2009\)](#) and reprinted from [Graf et al. \(2011a\)](#) with kind permission of Elsevier.

minority band gap, from the upper edge of the minority valence band to the bottom edge of the minority conduction band, is observed. The main impact of dynamical correlations is usually seen in the spectral (energy dependent) properties. In contrast, the electronic structure near the Fermi level and the related quantities must be much less affected due to the Fermi-liquid character of dynamical self-energy. Indeed, as shown in [Fig. 1.18](#) the full account of correlation effects within the LDA + DMFT approach does not significantly change the values of magnetic moments (as energy-integrated quantities) calculated within an account of the static part of correlations only, that is, with LDA + U ([Chadov et al., 2009](#)). The HMF state in  $\text{Co}_2\text{Mn}_{(1-x)}\text{Fe}_x\text{Si}$  is conserved for the whole range of  $x$  within the LDA + DMFT approach contrary to calculations that ignore correlation effects confirming the assumption, that the electron–electron correlation cannot be neglected in Heusler compounds ([Fig. 1.19](#)).

The electronic structure of the substitution series  $\text{Co}_2\text{Mn}_{(1-x)}\text{Fe}_x\text{Si}$  was also studied experimentally by high resolution, high energy X-ray photoelectron spectroscopy (HAXPES) ([Balke et al., 2006](#); [Fecher et al., 2007](#)). The high photon energy of 8 keV ensures a real bulk sensitivity for the valence band spectrum due to the high escape depth of the emitted electrons (115 Å). Most interesting in this investigation is the comparison of the calculated DOS and the measured spectra close to  $\epsilon_F$  as this might give an indication of the gap in the minority states. The majority band structure

contributes only a few states to the density at  $\epsilon_F$  emerging from strongly dispersed bands. This region of low density is surrounded by a high DOS arising from flat bands at the upper and lower limit of the minority band gap. The onset of the minority valence band is clearly seen in the total DOS as well as the low majority density at  $\epsilon_F$ . In fact, the same behavior was observed in the measured valence band spectra. The Fermi energy level can be estimated to be approximately 0.5 eV above the minority valence band. This is a strong evidence that all compounds of the  $\text{Co}_2\text{Mn}_{(1-x)}\text{Fe}_x\text{Si}$  series exhibit HMF behavior. However, the desired method to finally prove half-metallic ferromagnetism in Heusler compounds, is spin-resolved photoemission.

The electronic properties of all Heusler compounds strongly depend on the specific arrangement of the atoms on the different lattice positions. In fact, the intermixing of two atoms, or even complete atomic disorder may occur in some compounds (for a detailed discussion of different types of disorder see [Graf et al., 2009, 2011a](#)). The effect of atomic disorder on the electronic structure in Half-Heusler alloys was for the first time studied by Ebert and Schütz for  $\text{MnPtSb}$  ([Ebert and Schütz, 1991](#)). The local density of states (LDOS) was calculated using the spin-polarized relativistic Korringa–Kohn–Rostocker (KKR) method within an atomic sphere approximation (ASA). The comparison of the minority-spin band gap at  $\epsilon_F$  for an ordered and antisite disordered compound revealed that impurity states fill the band gap locally. This effect is most pronounced in case of Mn atoms on Pt sites, in which a peak arises in the minority-spin gap, resulting in a distinct reduction of the spin polarization and the magnetic moment.

A more quantitative investigation on the effect of atomic disorder was carried out by Orgassa et al. for  $\text{MnNiSb}$  ([Orgassa et al., 1999, 2000](#)). Here, the effect of random atom distributions on each lattice site was investigated by the layer KKR–ASA method combined with the CPA. The authors considered different types of atomic disorder: The partial interchange of Ni and Mn, the partial occupation of the vacant lattice site by Mn and Ni or Sb. In all cases, disorder-induced states appear in the minority-spin gap, resulting in a band gap narrowing and a reduction of the spin polarization at  $\epsilon_F$ . Although the spin polarization remains 100% for disorder levels lower than a few percent, a considerable decrease is initiated for higher amounts ( $\geq 5\%$ ). For instance, the spin polarization is reduced to 52% for 5% Mn–Ni interchange. When Mn and Sb occupy the vacant lattice site, a reduction to values as low as 24% takes place. Thus, a suppression of antisite disorder and very careful structure analysis is necessary to obtain high spin polarizations in Half-Heusler materials. Intrinsic defects in  $\text{MnNiSb}$  and their consequences for the spin polarization were also investigated theoretically by [Attema et al. \(2004\)](#). The authors showed that most types of defects which are likely to occur do not influence the spin polarization distinctly. To further clarify the relationship between atomic disorder and the spin

polarization, Miura et al. theoretically investigated the electronic structure of disordered  $\text{Co}_2\text{Cr}_x\text{Fe}_{(1-x)}\text{Al}$ , based on first-principle density functional calculations with the KKR–CPA (Miura et al., 2004a,b). This study revealed that in the parent phase  $\text{Co}_2\text{CrAl}$  the spin polarization remains high (more than 90%), even for a complete interchange of Cr and Al. A detailed analysis of the DOS and the atom orbital projected LDOS of Co 3d revealed that the energy gap of the minority DOS near  $\epsilon_F$  is mainly constructed of Co 3d states. Thus, the disorder between Cr and Al does not significantly affect the electronic structure near the Fermi level, and therefore, the semiconducting character of the minority bands is still kept even in the disordered B2 structure. Thus, it is no longer surprising that the TMR effect was observed for the first time at RT in magnetic tunnel junctions (MTJs) with CsCl-type (B2) disordered CCFA electrodes (Inomata et al., 2003). The spin polarization of  $\text{Co}_2\text{Cr}_x\text{Fe}_{(1-x)}\text{Al}$  is reduced with increasing Fe concentration for both ordered  $L2_1$  and disordered B2 structures. For CCFA the spin polarization is evaluated as 90% and 77% for the  $L2_1$  and B2-type structures, respectively (Miura et al., 2004b). Contrary to the Cr–Al interchange, the Co–Cr interchange gives rise to a considerable reduction of the spin polarization, due to the appearance of antiside Co 3d states in the minority-spin band gap. The total magnetic moment is reduced linearly from  $3 \mu_B$  per formula unit with increasing amount of Co–Cr disorder. Wurmehl et al. showed, that this reduction of the total magnetic moment can be attributed to ferrimagnetic order with an antiparallel alignment of the antiside Cr moments to the other magnetic moments on the ordinary Cr and Co sites (Wurmehl et al., 2006b).

## 6. HEUSLER COMPOUNDS IN DEVICES FOR SPINTRONIC APPLICATIONS

The development of present-day spintronics has the power to revolutionize Information and Communication Technology (ICT) in the same way the discovery of GMR did in the 1990's for data storage. Spintronics combines the intrinsic nonvolatility of magnetism with high speed and as such has the potential to resolve some of the major problems facing conventional electronics.

In the past,  $\text{Co}_2$ -based Heusler materials were intensely studied due to their high potential as new electrode materials in magneto resistance devices, such as MTJs (Herbot et al., 2009; Inomata et al., 2003; Ishikawa et al., 2006; Kämmerer et al., 2004; Kubota et al., 2004; Taira et al., 2009; Tsunegi et al., 2009) GMR devices (Furubayashi et al., 2008; Kodama et al., 2009; Nikolaev et al., 2009; Sakuraba et al., 2009; Yakushiji et al., 2006) and also for spin injection from ferromagnetic electrodes into SCs (Dong et al.,

2005). However, the advent of STT, which provides an ultra-low-power switching (writing) solution and can allow for the scaling of the individual bit cell below the 10 nm industry node, is foreseen as the next step to the development of practical spintronic devices. New and ideally RE-free materials for implementation in STT-magnetic random access memory (MRAM) and spin torque oscillators (STO) devices require high spin polarizations and  $T_C$  but low saturation magnetization ( $m_s$ ) and Gilbert damping in order to facilitate the sufficiently low switching currents according to the Slonczewski–Berger equation (Berger, 1996; Slonczewski, 1996). For an efficient and thermally stable switching, a material with a PMA would furthermore be preferable.

Many Heusler compounds are high-temperature ferromagnets/ferrimagnets with damping constants smaller than those of any conventional ferromagnetic metal. The necessary small  $m_s$  and a high  $T_C$  can be realized with ferrimagnetic Heusler-related compounds. Due to their tetragonal structure, the large uniaxial magnetic anisotropy  $K_u$  can be used to obtain PMA electrodes, thus opening the way to universally applicable spintronic devices, combining all the strengths and avoiding many of the weaknesses of the state of the art.

In the following achievements based on Heusler compounds as magnetic electrodes in TMR and GMR devices will be reviewed. Moreover, a newly developed spin injector scheme will be presented. Additionally, recent progress in the field of tetragonally distorted Heusler materials will be discussed.

## 6.1. Magneto resistance devices

The first theoretical prediction of half-metallicity in MnNiSb stimulated tremendous research interest, aiming at the utilization of Heusler compounds in MTJs. In fact, for a MnNiSb bulk single crystal a spin polarization of almost 100% at  $\epsilon_F$  was observed by means of spin-polarized positron annihilation (SSPA) (Hanssen and Mijnders, 1986; Hanssen et al., 1990). The preparation of thin films of this material, however, turned out to be not without difficulties. Therefore, different growth methods, comprising co-sputtering and molecular beam epitaxy (MBE), had to be employed to prepare epitaxial films. Finally, the crystal structure was confirmed by XRD as well as the presence of a magneto crystalline anisotropy (MCA). Furthermore, a maximum spin polarization of  $\approx 60\%$  at 1.6 K was observed by point-contact Andreev reflection measurements (Mancoff et al., 1999; Soulen et al., 1998; Tanaka et al., 1999). The first integration of an epitaxial MnNiSb thin film into a MTJ yielded a low TMR effect of 9% at RT and 18% at 4.2 K, which corresponds to a spin polarization of only 25% (Tanaka et al., 1999). Since another MnNiSb thin film, that was grown in a similar manner, showed a spin polarization of 60%, a considerable contribution of

atomic disorder at the empty lattice sites in the vicinity of the tunnel barrier is assumed (Orgassa et al., 1999). This is in good agreement with the reported vanishing of the energy gap for the minority spins at  $\epsilon_F$  with more than 7% atomic disorder and the fragility of the surface state due to reduced symmetry and surface reconstruction (Jenkins, 2004; Jenkins and King, 2001). Similar arguments can also be applied for other Half-Heusler thin films. For example, sputtering MnPtSb on  $\text{Al}_2\text{O}_3$  (001) substrates leads to the formation of spin valves showing a MR ratio of only 0.47% at RT (Johnson et al., 1996; Kautzky et al., 1997).

Scientific interest in this field was further stimulated by investigation carried out by Block et al., who discovered a large negative MR at RT in the quaternary Heusler compound  $\text{Co}_2\text{Cr}_{0.6}\text{Fe}_{0.4}\text{Al}$  (Auth et al., 2003; Block et al., 2003; Felser et al., 2003), which demonstrated the tunability of the spin density of states at the Fermi level by substituting constituent elements. Consequently, in pressed powder compacts that act as a series of MTJs, a MR of  $-30\%$  was reported in a small external field of 0.1 T. This discovery triggered enormous research efforts focusing on the implementation of this material into spintronic devices (Clifford et al., 2004; Conca et al., 2007; Inomata et al., 2003; Okamura et al., 2004). Shortly after that, the first TMR using a B2-ordered sputtered CCFA electrode was reported to be 26.5% at 5 K (16% at RT) by Inomata et al. (2003). The incorporation of Heusler compounds into TMR devices led to an dramatic increase in the TMR ratio in the following years as shown in Fig. 1.1. One breakthrough was the discovery of a large MR effect of nearly 600% in  $\text{Co}_2\text{MnSi}$  with an  $\text{AlO}_x$  tunnel barrier at low temperature (Sakuraba et al., 2006). However, the temperature dependence was strong and the TMR value decreased to only 70% at RT. The discovery of  $\text{Co}_2\text{FeSi}$ , the half-metallic Heusler compound with the highest magnetic moment of  $5.97 \mu_B$  and the highest Curie temperature of 1100 K (Wurmehl et al., 2006c), and the adjustment of the Fermi level to the middle of the gap using  $\text{Co}_2\text{FeAl}_{0.5}\text{Si}_{0.5}$  or  $\text{Co}_2\text{Fe}_{0.5}\text{Mn}_{0.5}\text{Si}$  improved the temperature dependence considerably (Fecher and Felser, 2007; Kandpal et al., 2007b). Nevertheless, the list of promising candidates is long, and many different materials have been tested, for example,  $\text{Co}_2\text{FeSi}$ ,  $\text{Co}_2\text{MnSi}$ ,  $\text{Co}_2\text{MnGe}$ ,  $\text{Co}_2\text{Fe}_{0.5}\text{Mn}_{0.5}\text{Si}$ ,  $\text{Co}_2\text{FeAl}_{0.5}\text{Si}_{0.5}$  (Ebke et al., 2008; Gercsi et al., 2006; Marukame et al., 2006; Tezuka et al., 2006b; Tsunegi et al., 2008). Subsequently an improvement of the film quality led to a distinct improvement of the MTJs based on Heusler compounds. For tungsten-type disordered  $\text{Co}_2\text{FeAl}$ , a TMR at RT of 47% was obtained, while  $\text{Co}_2\text{FeAl}$  electrodes in the CsCl-type structure yielded only a TMR of 27% (Okamura et al., 2005). These results are in good agreement with calculations that predicted a spin polarization ( $P$ ) of 62% for the tungsten-type and 30% for the B2-type structure (Miura et al., 2004a). It turned out, that not only a sufficient crystallinity of the thin films plays a major role in MTJs, but that also the surface roughness and the

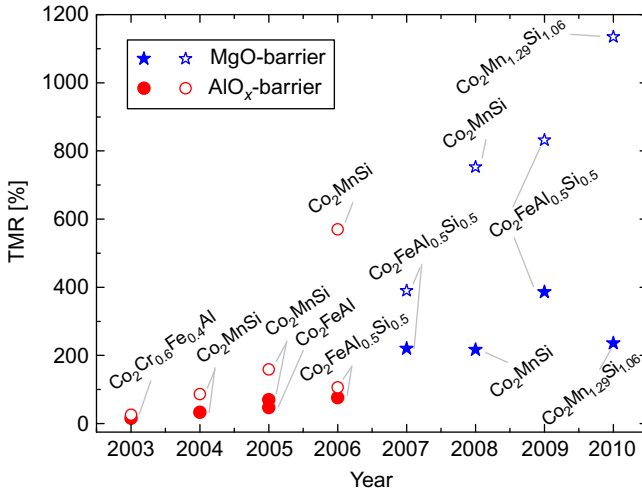


**Figure 1.19** Development of the TMR ratio for MTJs with Heusler electrodes. Open symbols denote the TMR value at 5 K, while filled symbols display the value at room temperature. Data taken from Inomata et al. (2003), Kämmerer et al. (2004), Okamura et al. (2005), Sakuraba et al. (2006), Tezuka et al. (2006a, 2007, 2009), Tsunegi et al. (2008), and Yamamoto et al. (2010). Reprinted from Graf et al. (2011a) with kind permission of Elsevier.

interface morphology between the Heusler electrode and the barrier has a great influence on the TMR value (Oogane et al., 2006). As a result, epitaxially grown Heusler alloys with flat surfaces lead to distinctly enhanced TMR ratios. Apart from that, a spin polarization of 0.49 was measured for an ordered Co<sub>2</sub>FeSi thin film by the point Andreev reflection technique (PCAR). TMR values obtained from the MTJs with such Co<sub>2</sub>FeSi electrodes and an alumina barrier were 67.5% at 5 K and 43.5% at 298 K, respectively (Gercsi et al., 2006). The  $P$  value estimated from the TMR, using Jullière's model, matches the spin polarization measured by PCAR very well, indicating that the TMR value from the MTJ is governed by the intrinsic value of  $P$  of the electrode material for incoherent tunneling. But in fact, PCAR is a technique in which the spin polarization of a material depends on fitting parameters. Therefore, the spin polarization of tunnel junctions often differs from the results obtained by PCAR. On the other hand, a TMR ratio 159% at 2 K was observed for an alumina barrier with an epitaxially grown L<sub>21</sub>-ordered Co<sub>2</sub>MnSi electrode and an Co<sub>75</sub>Fe<sub>25</sub> top electrode (Oogane et al., 2006). According to Jullière's formula, the spin polarization of the Co<sub>2</sub>MnSi bottom electrode in these MTJs was estimated to be  $P=0.89$ . Unfortunately, the observed TMR value shows a large temperature dependency. However, the replacement of the top Co<sub>75</sub>Fe<sub>25</sub> electrode by Co<sub>2</sub>MnSi led to comparable TMR values at RT, but a



dramatical increase is observed with decreasing temperature to 570% at 2 K (Sakuraba et al., 2006). If the spin polarization of the lower  $\text{Co}_2\text{MnSi}$  electrode is assumed to be 89%, the spin polarization for the upper  $\text{Co}_2\text{MnSi}$  electrode can be estimated to be 83%. The strong temperature dependency is commonly attributed to spin-flip tunneling caused by magnetic impurities at the  $\text{Co}_2\text{MnSi}/\text{AlO}_x$  interface or pinholes in the barrier. Especially, for MTJs containing  $\text{Co}_2\text{MnSi}$ , the creation of magnetic impurities is a critical problem, as Mn and Si both have a high affinity to oxygen compared to other 3d transition metals. Furthermore, the location of  $\epsilon_F$  in the half-metallic energy gap is an important factor in the temperature dependency of the TMR ratio. Therefore, the large decrease in the TMR ratio is also attributed to the small energy separation between the Fermi level and the bottom of the conduction band, since the thermal fluctuations at RT are twice as big as this energy separation.

A different approach for obtaining much larger TMR values was established by the using single-crystalline MgO as barrier material (Butler et al., 2001; Mathon and Umerski, 2001; Parkin et al., 2004; Yuasa et al., 2004). Theoretical investigations show that the principle of coherent tunneling can also be applied to  $\text{Co}_2\text{MnSi}/\text{MgO}$  junctions (Miura et al., 2007). Here, the introduction of MgO barriers into MTJs with Heusler electrodes led to a dramatic improvement in their performance. In addition to that, the relatively small lattice mismatch between  $\text{Co}_2\text{YZ}$  and MgO for a  $45^\circ$  in-plane rotation (e.g.,  $\approx -3.7\%$  for  $\text{Co}_2\text{Cr}_{0.6}\text{Fe}_{0.4}\text{Al}$ , and  $-5.1\%$  for  $\text{Co}_2\text{MnSi}$ ) makes the fabrication of fully epitaxial MTJ trilayers possible, featuring smooth and abrupt interfaces (Ishikawa et al., 2006; Marukame et al., 2007; Marukame and Yamamoto, 2007; Yamamoto et al., 2006). As a result, relatively high TMR ratios of 109% at RT (317% at 4.2 K) were demonstrated for  $\text{Co}_2\text{Cr}_{0.6}\text{Fe}_{0.4}\text{Al}/\text{MgO}/\text{Co}_{50}\text{Fe}_{50}$  MTJs (Marukame et al., 2007), and 90% at ambient temperature (192% at 4.2 K) for  $\text{Co}_2\text{MnSi}/\text{MgO}/\text{Co}_{50}\text{Fe}_{50}$  MTJs (Ishikawa et al., 2006). A further increase of the TMR ratio was achieved by the fabrication of MTJs with  $\text{Co}_2\text{MnSi}$  electrodes as both, the lower and upper electrode, leading to TMR ratios of 179% at RT and 638% at 4.2 K (Ishikawa et al., 2008). An even higher value of 753% at 2 K was obtained for a  $\text{Co}_2\text{MnSi}/\text{MgO}/\text{Co}_{50}\text{Fe}_{50}$  junction (Tsunegi et al., 2008). Although these results are promising, a large decrease with increasing temperature to 217% at RT was still observed, which was explained with the occurrence of inelastic tunneling events, caused by magnon excitations due to the low Curie temperature at the  $\text{Co}_2\text{MnSi}$  surface, and by magnetic impurity scatterings, resulting from the presence of Mn and Si oxide impurities. However, the highest reported TMR ratio so far of 340% at RT was observed in a B2-type disordered  $\text{Co}_2\text{FeAl}$ -based MTJ (Wang et al., 2010). Since this Heusler material does not exhibit a complete spin polarization, the high TMR value is a strong indication for pronounced coherent tunneling. Additionally, a TMR oscillation as a function of the MgO layer thickness was

observed. First-principles electronic band structure calculations confirm, that the B2-type disordered  $\text{Co}_2\text{FeAl}$  behaves like a half-metal in terms of the  $\Delta_1$  symmetry in the (001) direction. It should be pointed out, that this remarkable result was achieved with a Heusler alloy displaying considerable disorder. This result strongly indicates that Heusler compounds are promising materials for a giant TMR due to coherent tunneling and their tunable electronic and magnetic properties.

In addition to the fabrication of TMR devices, current-perpendicular-to-plane (cpp)-GMR devices with Heusler electrodes recently emerged in the field of spintronics. Compared to TMR, cpp-GMR is expected to be insensitive to the electronic state at the interfaces, where half-metallicity is often destroyed. In fact, the first cpp-GMR devices consisted of two  $\text{Co}_2\text{MnSi}$  electrodes, sandwiching a 3-nm Cr spacer (Yakushiji et al., 2006). For this trilayer system a maximum MR ratio of 36.4% was obtained at RT (67.2% at 110 K) (Sakuraba et al., 2010). It should be noted that the choice of the spacer layer is an important issue, since epitaxial growth of the Heusler thin film on the spacer material is required to form fully epitaxial Heusler/spacer/Heusler trilayers. A large spin-diffusion length and low resistivity are also necessary for the spacer layer to obtain large cpp-GMR values. These considerations, combined with a small lattice mismatch, led to the selection of silver as an ideal spacer layer. Consequently, a cpp-GMR ratio of 6.9% at RT (14% at 6 K) was realized for a  $\text{Co}_2\text{FeAl}_{0.5}\text{Si}_{0.5}/\text{Ag}/\text{Co}_2\text{FeAl}_{0.5}\text{Si}_{0.5}$  structure (Furubayashi et al., 2008). Additionally, an enhanced cpp-GMR ratio of 34% at 290 K (80% at 14 K) for the same system was just reported recently (Nakatani et al., 2010).

A different approach is given by the using copper as spacer material. Despite the large lattice mismatch between Cu and Heusler compounds, cpp-GMR values of 8.6% at RT (30.7% at 6 K) were obtained for the system  $\text{Co}_2\text{MnSi}/\text{Cu}/\text{Co}_2\text{MnSi}$  (Kodama et al., 2009). To minimize the lattice mismatch and to optimize the interface scattering properties, “all-Heusler” cpp-GMR devices with the trilayer  $\text{Co}_2\text{MnSi}/\text{Ru}_2\text{CuSn}/\text{Co}_2\text{MnSi}$  were proposed. These devices yielded a MR ratio of 6.7% at RT (Nikolaev et al., 2009). Narrow cpp-GMR read heads, incorporating Heusler materials as reference layers, were successfully tested using a conventional spin-stand system. Thus, the capability of the cpp-GMR technology for ultrahigh density magnetic recording was demonstrated, further development of the cpp-GMR stag materials, however, is necessary, to make the heads superior to TMR heads (Nikolaev et al., 2008).

The tremendous impact of Heusler compounds can also be seen in new developments by leading industrial companies. For instance, Toshiba designed an all Heusler cpp-GMR device with  $\text{Co}_2\text{MnGe}$  electrodes and a nonmagnetic  $\text{Ru}_2\text{CuSn}$  spacer layer which yielded a MR ratio of 6.7% for a bottom spin-valve configuration (Nikolaev et al., 2009). Hitachi developed cpp-GMR devices based on Heusler alloys which exploit their

high spin polarization but produce minimal current-induced noise without loss of MR of sensor resolution (Carey et al., 2008). Furthermore, they applied band structure calculations to study the influence of impurities and distortions on  $\text{Co}_2\text{MnGe}$ , yielding that the spin polarization is retained even under significant strains and distortions, whereas impurity concentrations as low as 3% affect the spin polarization distinctly (Carey et al., 2004).

Another important aspect for the understanding and the advancement of Heusler-based devices is a detailed knowledge of the spin structure on the nanometer scale. Vaz et al. studied the spin configuration of  $\text{Co}_2\text{FeAl}_{0.4}\text{Si}_{0.6}$  thin film elements using X-ray magnetic circular dichroism photoemission electron microscopy (XMCD-PEEM) (Vaz et al., 2011). These investigations revealed that, for  $\text{Co}_2\text{FeAl}_{0.4}\text{Si}_{0.6}$  alloy elements below 2  $\mu\text{m}$  in size, well defined magnetic states are observed, determined by the interplay between exchange energy and magnetocrystalline and shape anisotropies. Furthermore, the existence and control of domain walls is a prerequisite for domain wall-based applications and experiments (Parkin et al., 2008). The authors showed, that domain walls in Heusler alloys can be generated reproducibly for elements with typical widths around 500 nm, determined mostly by the shape anisotropy (Vaz et al., 2011). The domain wall spin configuration becomes more complicated for wider elements that are more strongly affected by the MCA and magnetic ripple domains. This study shows the high spin polarization in  $\text{Co}_2\text{FeAl}_{0.4}\text{Si}_{0.6}$  elements and the resistance to thermally activated changes make this material an interesting candidate for future applications and experiments.

## 6.2. Spin injection

Pioneering work on the growth of Heusler alloys/SC hybrid structures was performed by Ambrose et al. (2000). The authors successfully demonstrated the epitaxial growth of  $\text{Co}_2\text{MnGe}$  on GaAs(001) with minor enhancement of the lattice constant as compared to the bulk value. However, calculations suggested for this particular system, that a strong reduction of the magnetic moment may occur near the  $\text{Co}_2\text{MnGe}/\text{GaAs}$  interface due to the Co–As and Co–Ga bonding (Picozzi et al., 2003). A different example for the incorporation of Heusler compounds into spin injection devices was given by Hirohata et al., who prepared  $\text{Co}_2\text{Cr}_{(1-x)}\text{Fe}_x\text{Al}$  thin films on GaAs(001) substrates by MBE (Hirohata et al., 2005). In this system, the initial formation of the A2-type structure has been observed up to a thickness of  $\approx 2$  monolayers, followed by a B2-type structure above 3.5 monolayers and the stable  $\text{L}_{21}$  phase above 13–14 monolayers (Hirohata et al., 2006). Even though the half-metallicity should be preserved at the Co/As interface on the (001) surface (Nagao et al., 2004), the initial growth of the A2 structure may introduce unfavorable interfaces, such as CrAl/As, and therefore, reduce the half-metallicity in the vicinity of the interface.

Spin injection experiments with off-stoichiometric  $\text{Co}_{1.6}\text{Mn}_{2.4}\text{Ga}$  revealed a injected electron spin polarization into InGaAs of 13% at 5 K (Hickey et al., 2005). An injected spin polarization of 27% at 2 K was reported for the system  $\text{Co}_2\text{MnGe}/\text{GaAs}$  (Dong et al., 2005), contrast to the value of 40% reached with an Fe injector.

The growth of the Half-Heusler material  $\text{MnNiSb}$  on semiconducting substrates offers another opportunity to build spin-injection devices (Van Roy et al., 2000a, 2003). In this context, the epitaxial growth on InP was demonstrated which is favored compared to GaAs due to a smaller lattice mismatch (Bach et al., 2003; Van Roy et al., 2000b).

Apart from that, the injected polarization of Heusler compounds is significantly below the value of 100% that would be expected for a half-metal. Possible explanations for this phenomenon comprise a local atomic disorder and small band gaps for the minority spins, for example,  $\approx 200$  meV in  $\text{Co}_2\text{MnGe}$  (Picozzi et al., 2002). Consequently, Heusler compounds with larger minority spin gaps, such as  $\text{Co}_2\text{MnSi}$  (Ishida et al., 1998; Schmalhorst et al., 2004), may be more efficient injectors. Since spin injection experiments probe the spin polarization at the interface, a realistic theory does not only need to consider the electronic structure of the interface, but also the presence of atomic disorder, epitaxial strain as well as the effects of nonzero temperature, such as coupling of interface states to bulk states. Recently, a new scheme for efficient spin injection has been proposed by Chadov et al. which could overcome these obstacles (Chadov et al., 2011). Suitable material combinations can be derived from the same parent compounds. By making various mixtures one can produce a series of new Heusler materials with smoothly varying electronic properties ranging from half-metallic, magnetic to semiconducting and nonmagnetic. Much helpful in such design is the Slater–Pauling rule (Pauling, 1938; Slater, 1936b) which states the linear dependency of the unit cell magnetic moment as a function of the valence electrons number (see Section 4 for a detailed discussion). The basic idea is sketched in detail by using the example of the well-known Heusler  $\text{Co}_2\text{MnAl}$  (Buschow and van Engen, 1981) which fulfills the basic requirements of the efficient spin-injecting material. Band structure calculations (Jia et al., 2008; Kübler et al., 2007) characterize it as the HM ferromagnet with magnetic moment of  $4 \mu_B$  in agreement with experiment. Its measured Curie temperature is  $T_C = 698$  K (Jung et al., 2009; Webster, 1971). In order to derive a SC material with a similar lattice it is enough to substitute one Co atom by V. It can be synthesized, for example, by 50–50 mixing of  $\text{Mn}_2\text{Val}$  (Jiang et al., 2001) and  $\text{Co}_2\text{Val}$  (Kanomata et al., 2010). The resulting  $\text{CoMnVAl}$  (SC) compound with 24 valence electrons is nonmagnetic in agreement with the Slater–Pauling rule (Basit et al., 2011). The unit cells and corresponding calculated bulk band structures of both  $\text{Co}_2\text{MnAl}$  and  $\text{CoMnVAl}$  are shown in Fig. 1.20a. To verify which sequence of stacking layers conserves the

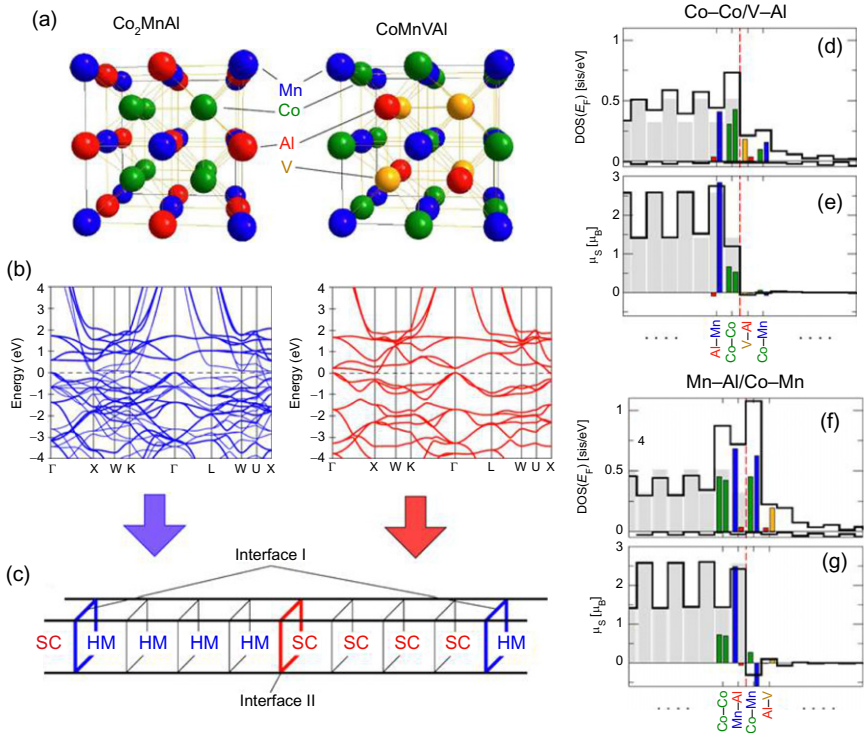


**Figure 1.20** (a) Crystal structures of the typical candidate materials: the half-metallic ferromagnet  $\text{Co}_2\text{MnAl}$  and the nonmagnetic semiconductor  $\text{CoMnVAl}$ . (b) Their calculated bulk band structures. In case of  $\text{Co}_2\text{MnAl}$ , the bands of the gapped minority-spin channel are made thicker. The Fermi level is marked by the dashed line. (c) Structure of the supercell. Subsections marked as HM or SC represent the complete Heusler blocks, each containing four atomic layers. (d and f) The black solid line represents the layer-resolved DOS at the Fermi energy with positive values referring to the majority-spin, negative to the minority-spin channels and the magnetic moments (e, f) calculated for HM/SC supercells (HM 1/4  $\text{Co}_2\text{MnAl}$ , SC 1/4  $\text{CoMnVAl}$ ). Pale gray bars show the corresponding values calculated for the bulk HM and SC materials. Darker (colored) bars mark the atom-projected contributions within the first nearest and next nearest interface layers (each layer contains two atoms). Vertical red dashed lines mark the interface borders. Data taken from [Chadov et al. \(2011\)](#).

half-metallicity the corresponding band structure calculations for the  $\text{Co}_2\text{MnAl}/\text{CoMnVAl}$  interfaces were performed. In the following example the stacking direction between  $\text{CoMnVAl}$  and  $\text{Co}_2\text{MnAl}$  is chosen along the densely packed (001) plane as shown on [Fig. 1.20b](#). Since the supercell contains an integer number of these units, in general it has no inversion center. For this reason one deals with two nonequivalent interfaces within

each supercell. There are four stacking possibilities along the (001) plane which can be paired in two different supercells. The first one will contain Co–Co/V–Al and Mn–Al/Co–Mn, and the second—Co–Co/Co–Mn and Mn–Al/Al–V interfaces. The spin polarization indeed depends critically on the way of stacking: half-metallicity is preserved for the system with Co–Co/V–Al and Co–Mn/Mn–Al interfaces, and in case of Co–Co/Mn–Co and Mn–Al/Al–V interfaces it is destroyed.

At Co–Co/V–Al (d), and Co–Mn/Mn–Al (f) interfaces, the spin polarization increases. This effect can be qualitatively understood by comparing the materials effectively formed on the interfaces with their ideal bulk equivalents, since the properties of Heuslers in a large extent originate from the nearest neighbor coupling. Indeed, Co–Co/V–Al and Co–Mn/Mn–Al interfaces correspond to the existing Heusler compounds with  $2 \mu_B$  magnetic moment and high spin polarization:  $\text{Co}_2\text{Val}$  (Jia et al., 2008; Jiang et al., 2001) and  $\text{Mn}_2\text{CoAl}$  (Liu et al., 2008a). Figure 1.20e and f show that, except of the overall demagnetization, the magnetic structure of these interfaces is rather similar to their bulk equivalents. Indeed, both interfaces are half-metallic.

Thus the authors concluded that the “constructive” interface (preserving the half-metallicity) can be formed if the effective interface composition would correspond to the stable bulk material with the intermediate properties between the left- and right-side materials, as in the sequence of  $\text{Co}_2\text{MnAl}/\text{Co}_2\text{Val}/\text{CoMnVal}$  which exhibit bulk magnetic moments of 4, 2 and  $0 \mu_B$ , respectively. The experimentally suitable method to obtain the 24-electron SC material would be through a mixture of two stable HMFs with numbers of valence electrons larger and smaller than 24.

This situation is rather general. By applying similar first-principle analysis an analogous situation was found for other  $\text{Co}_2$ -based Heusler materials. The pairs of “constructive” and “destructive” interfaces were obtained also for  $\text{Co}_2\text{MnZ}/\text{CoMnTiZ}$  ( $Z = \text{Si, Ge, Sn}$ ) and  $\text{Co}_2\text{FeZ}/\text{CoFeTiZ}$  ( $Z = \text{Al, Ga}$ ) (more details can be found in Felser et al., 2010). For the “constructive” case the effective interface compounds will correspond to  $\text{Co}_2\text{TiZ}$  group of HMFs with magnetic moments of  $1 \mu_B$ . Due to the chemical and structural compatibilities the possible disorder in “constructive” interfaces could be expected to be “constructive” as well, since it will be restricted more probably to the disorder which intrinsically occurs in the corresponding bulk systems, which are known to remain half-metallic.

## 7. TETRAGONAL HEUSLER COMPOUNDS

Amongst the multifunctional Heusler compounds Mn-based materials have received special attention in recent years due to their dynamical behavior in different structural configurations. A variety of magnetic ordering is observed in Heuslers with the  $\text{X}_2\text{YZ}$  structure depending on the

location of Mn atoms in the lattice (X, Y, or Z). Of particular interest are compounds of the  $\text{Ni}_2\text{MnZ}$  ( $Z = \text{Ga, Sn, In, and Sb}$ ) family because of their important functional as well as fundamental properties (Kainuma et al., 2006a; Krenke et al., 2005b); also,  $\text{Mn}_2\text{YZ}$ -based compounds for their potential use in spintronics and spin torque devices (Alijani et al., 2011c; Klaer et al., 2011).

Recent development of efficient spintronic devices is substantially focused on exploiting the STT effect since the improvement of data storage permanently requires to minimize the distance between storage elements (Berger, 1996; Ikeda et al., 2010; Slonczewski, 1996). STT, which provides an ultra-low-power switching (writing) solution and makes down-scaling of the individual bit cell below 10 nm possible, is predicted to be the next key step towards the development of practical spintronic devices. For radio frequency devices a new type of an integrated spin torque nano oscillator (STNO) has been proposed for telecommunication. Furthermore, the use of such a material as a tip in a spin-polarized scanning tunneling microscope (STM), would not give rise to stray flux, and thus, would not distort the domain structure of a soft magnetic material. The major advantage of switching by a spin-polarized current compared to the field-induced switching of the magnetization direction is that the stray fields causing the undesired writing on vicinal elements do not appear. The requirements on materials utilized for STT devices are highly ambitious because the contrary demands of low switching currents and thermal stability need to be fulfilled (Huai, 2008). The key property for the corresponding, ideally RE-free materials, is a strong MCA energy providing the out-of-plane magnetization, the so-called perpendicular magnetocrystalline anisotropy (PMA). Further properties required are a high spin polarization and  $T_C$  but a low saturation magnetization  $M_S$  and Gilbert damping in order to facilitate the sufficiently low switching currents according to the Slonczewski–Berger equation (Berger, 1996; Slonczewski, 1996).

Half-metallic ferrimagnetic materials are desirable candidates for the application in magnetoelectronic devices. The advantage of a ferrimagnetic interaction is the resulting reduction of the magnetic moment due to the compensation of the moments carried by different sublattices. These materials offer distinct advantages over their ferromagnetic counterparts which are mostly due to their small magnetic moment. The ideal compensated ferrimagnet would exhibit a total magnetic moment of zero. For such compensated ferrimagnets which were initially named “compensated anti-ferromagnets” single spin superconductivity was predicted by Pickett (1996). Further interesting applications can be envisioned, since they do not give rise to strong stray fields and are less effected by external magnetic fields. An ideal case for application would be a half-metallic compensated ferrimagnet since it would be a perfectly stable spin-polarized electrode in a junction device, especially for current-induced magnetic switching.



Many Heusler compounds intrinsically exhibit the important STT properties of high spin polarization and high  $T_C$  (Graf et al., 2011b; Wurmehl et al., 2006a), which are important for the stable performance of spintronic devices at RT and above. Cubic Heusler compounds, however, do not exhibit MCA and thus not the advantages, which can be realized in PMA materials. However, it is known that valence instabilities in their electronic structures can force a cubic Heusler unit cell to undergo a tetragonal distortion corresponding to a band Jahn–Teller effect (Suits, 1976). Heusler compounds with a cubic-to-tetragonal martensitic transition are well known in the context of the magnetic shape memory effect (Jakob and Elmers, 2007), and most recently their attractivity for STT applications was discovered (Balke et al., 2007b; Winterlik et al., 2008).

A combination of the above explained Slater–Pauling rule and the Kübler rule allows the prediction of half-metallic completely compensated ferrimagnetism in cubic Heusler compounds with 24 valence electrons (Wurmehl et al., 2006d). In these compounds, the two atoms on the X site have to compensate the magnetic moment of the atom at the Y site (mostly Mn). For Mn to be located on the Y position it has to be the more electropositive transition metal in the compound. The only possible elements to occupy the X position are, therefore, Fe, Co, Ni, Cu, and Zn, as well as Mn itself. The total valence electron number of 24 restricts the possible combinations to the binary  $\text{Mn}_2\text{MnZ}$  compounds, with Z being an element from the third main group of the periodic table. Wurmehl et al. first designed the material  $\text{Mn}_2\text{MnGa}$  (or simply  $\text{Mn}_3\text{Ga}$ ) indeed leading to a totally compensated half-metallic ferrimagnet with the  $L2_1$  Heusler structure with  $\text{Mn}^{3+}$  on the octahedral position (Kübler rule) (Wurmehl et al., 2006d). The two magnetic moments of the manganese atoms on the tetrahedral positions cancel the moment of the  $\text{Mn}^{3+}$  leading to zero net magnetization.

The synthesis of  $\text{Mn}_3\text{Ga}$ , however, revealed, that this compound does not crystallize in the cubic and ordered Heusler structure, but in the aforementioned tetragonally distorted structure desired for STT applications and suggested the materials  $\text{Mn}_{3-x}\text{Ga}$  to exhibit strong PMA (Balke et al., 2007a; Winterlik et al., 2008). *Ab initio* calculations for the distorted crystal structure have shown that  $\text{Mn}_3\text{Ga}$  is ferrimagnetically ordered with a total magnetic moment of  $\approx 1.7 \mu_B$  and  $T_C$  was found to be higher than 770 K. A higher DOS of the minority electrons compared to the majority channel at  $\epsilon_F$  indicates a distinct difference in the conductivity between the two spin directions. Furthermore, a pronounced magnetic anomaly was observed, which suggests that  $\text{Mn}_3\text{Ga}$  is a magnetically frustrated ferrimagnet. Tetragonally distorted  $\text{Mn}_{2.5}\text{Ga}$  films were grown on Cr-buffered MgO substrates with the tetragonal  $c$ -axis pointing along the normal direction, resulting in a giant PMA with an effective magnetic anisotropy energy of  $K_u^{\text{eff}} = 1.2 \times 10^7 \text{ erg/cm}^3$  (Wu et al., 2009). The proposed high spin



polarization was confirmed by Coey et al. (Kurt et al., 2011). Recently, an exceptionally low Gilbert damping and long-lived ultrafast spin precession of up to 280 GHz in  $\text{Mn}_{3-x}\text{Ga}$  was demonstrated by Mizukami et al. (2011b). The superiority of the  $\text{Mn}_{3-x}\text{Ga}$  compounds to various materials which show a PMA in thin films is also evident from the summary presented in Fig. 1.21.

A tunable PMA material for STT magnetic random access memories (STT-MRAM) is supposed to contain a fixed layer with strong MCA and an easily switchable free layer. The major drawback of  $\text{Mn}_3\text{Ga}$  is its huge lattice mismatch with  $\text{MgO}$  (the most commonly used tunneling barrier) which leads to an unsatisfactory TMR in devices. Furthermore, a lower magnetic moment as the  $1 \mu_B$  in  $\text{Mn}_3\text{Ga}$  would be preferable. Recently a design scheme for tetragonal Heusler compounds was presented opening a straightforward access to a large number of PMA–Heusler compounds (Winterlik et al., 2012) which could fulfill all the requirements on an STT material: tunability of the magnetic moment and the lattice parameters, high spin polarization, high  $T_C$ , high MCA due to a tetragonal distortion of the unit cell, and low Gilbert damping due to moderate SOC of the 3d and 4p elements in Heusler compounds compared to many other anisotropic magnetic compounds such as  $\text{FePt}$ . The underlying idea of this design

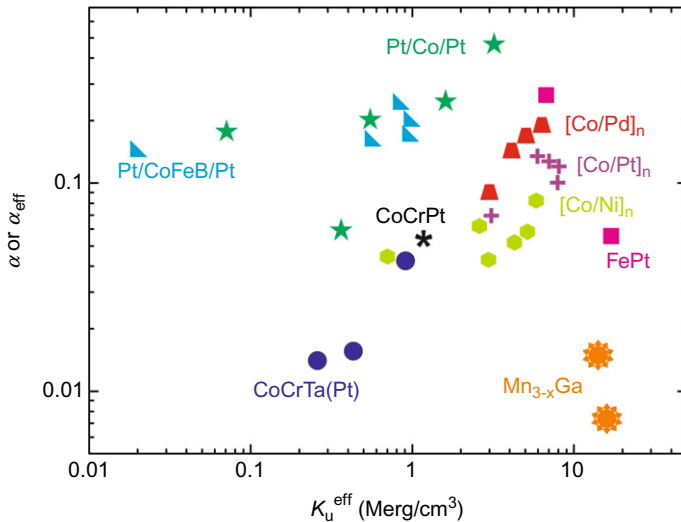


**Figure 1.21** Summary of the damping constant  $\alpha$  versus the effective perpendicular magnetic anisotropy energy  $K_u^{\text{eff}}$  for various thin films with PMA. Data taken from Barman et al. (2007), Ikeda et al. (2010), Inaba et al. (1997), Kim et al. (2011), Malinowski et al. (2009), Mizukami et al. (2010a,b, 2011a,b, 2011, Nozaki et al. (2009), and Pal et al. (2011). Figure adopted from S. Mizukami.

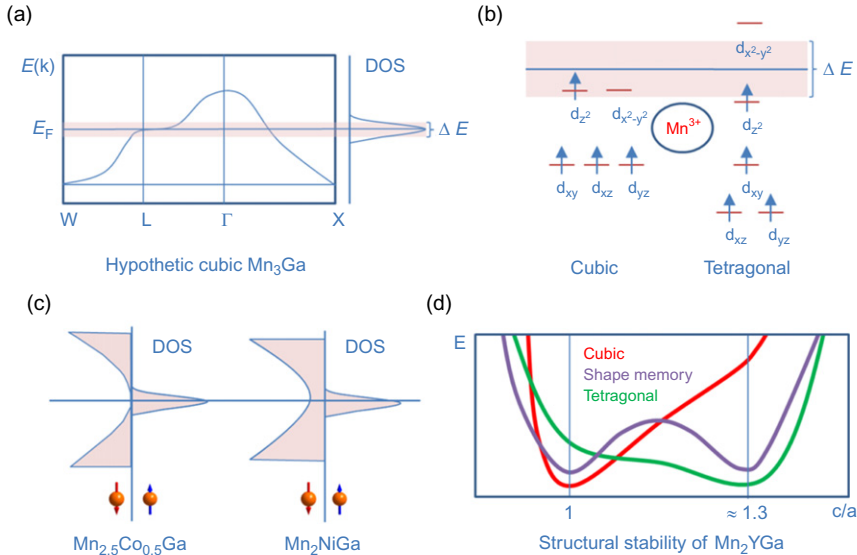


**Figure 1.22** The design scheme of tetragonal  $Mn_2$ -based Heusler compounds. The schematic band structure of hypothetical cubic  $Mn_3Ga$ , which represents the typical DOS of nearly all Heusler compounds exhibiting the tetragonal distortion caused by the van Hove singularity in proximity of  $\epsilon_F$  is shown in (a). The corresponding energy level scheme of a  $Mn_2YZ$  Heusler compound conforms to the molecular  $e_g$  orbitals (MO) of  $Mn^{3+}$  ions with  $d_4$ -configuration as determined by calculations as depicted in (b). The tetragonal distortion lifts the degeneracy of the  $e_g$  orbitals. Exemplary spin-resolved densities of states of half-metallic  $Mn_{2.5}Co_{0.5}Ga$  and the shape memory alloy  $Mn_2NiGa$  are shown in (c). In case of  $Mn_{2.5}Co_{0.5}Ga$ , the system is stable in the tetragonal phase. The DOS of  $Mn_2NiGa$  also shows a van Hove singularity. However, the total energy difference between the different crystal phases is small, resulting in a shape memory behavior (d).

scheme as shown in Fig. 1.22 is that the structural instability of the cubic phase is typically indicated by van Hove singularities in proximity of  $\epsilon_F$  resulting in high peaks of the DOS. These singularities can be straightforwardly identified by *ab initio* band structure calculations. If all reasonable electronic relaxation mechanisms including magnetism cannot remove the van Hove singularity, the only way to escape from this type of instability is by undergoing a structural distortion, thereby reducing the DOS at  $\epsilon_F$ . This is the necessary condition for the tetragonal distortion but it is not sufficient for a high MCA. As mentioned above, in Heusler compounds the octahedrally coordinated Mn atoms typically exhibit the  $d^4$  configuration of  $Mn^{3+}$  ions and are thus very susceptible to Jahn–Teller distortions. The characteristics of the crystal field splitting on the Mn atoms are shown in Fig. 1.23. If the corresponding degenerated  $e_g$  states are found at  $\epsilon_F$  for  $c/a = 1$ , then a

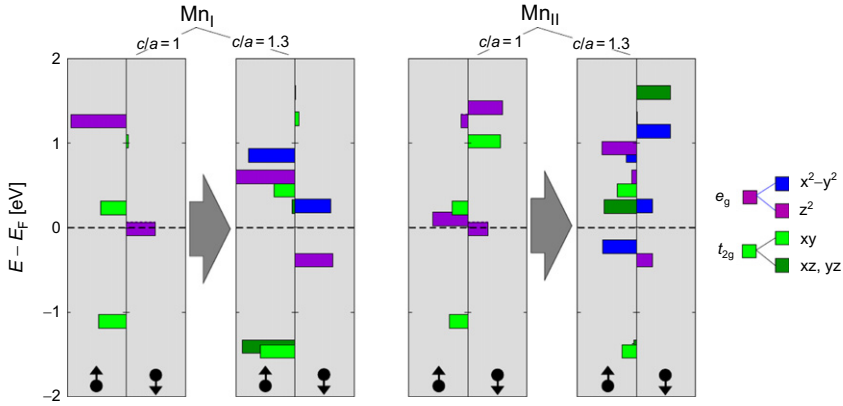


**Figure 1.23** Effect of the tetragonal strain on the orbital structure. The current example corresponds to the  $\text{Mn}_3\text{Ga}$  system. The horizontal bars mark the d-energy levels of the octahedrally (Mn-I) and tetrahedrally coordinated (Mn-II) atoms calculated at the  $\Gamma$  point of the Brillouin zone. Left or right orientation of a bar distinguishes the “up” or “down” spin channels, respectively (also indicated by black arrows). The size of a bar corresponds to the relative spectral weight of the certain symmetry distinguished by color. In the cubic crystal ( $c/a = 1$ ) the d-orbitals group in twofold  $e_g$  ( $z^2, x^2 - y^2$ ) and threefold  $t_{2g}$  ( $xy, xz, yz$ ) representations of the octahedron symmetry group, marked by violet and light-green, respectively. By undergoing tetragonal strain along the  $z$ -axis ( $c/a = 1.3$ ), the out-of-plane orbitals split out from the in-plane ones. In particular, the  $e_g$  orbitals at  $\epsilon_F$ , which carry the van Hove singularity in the “down” spin channel, split into  $x^2 - y^2$  (blue) and  $z^2$  (violet) above and below  $\epsilon_F$ , thereby reducing the corresponding DOS peak.

local minimum of the total energy will be shifted towards  $c/a \neq 1$  (the typical value of tetragonal Heusler compounds is close to 1.3, however the whole range varies within  $0.95 \leq c/a \leq 1.43$ ). What remains is to evaluate the relative stability of the material for different distortions. The derived energy profiles allow to distinguish between a stable tetragonal distortion ( $\text{Mn}_3\text{Ga}$ ), a stable cubic structure ( $\text{Mn}_2\text{CoGa}$ ), and a shape memory system ( $\text{Mn}_2\text{NiGa}$ ). The corresponding results of the first-principle calculations are shown in Fig. 1.24. Typical profiles of stable cubic compounds exhibit the total energy minimum at  $c/a = 1$ , those of tetragonal compounds at  $c/a \neq 1$ . Shape memory compounds exhibit two distinct minima (cubic and tetragonal structures) separated by a small energy barrier.  $\text{Mn}_{2.5}\text{Co}_{0.5}\text{Ga}$  is a system, which appears exactly at the borderline between the stable and unstable cubic structures.

The whole manifold of possible structures formed by the especially useful  $\text{Mn}_2\text{YZ}$  Heusler compounds is shown in Fig. 1.25. When the Y element is more electronegative than the Mn atom, the so-called inverse Heusler structure including three different magnetic sublattices is formed.

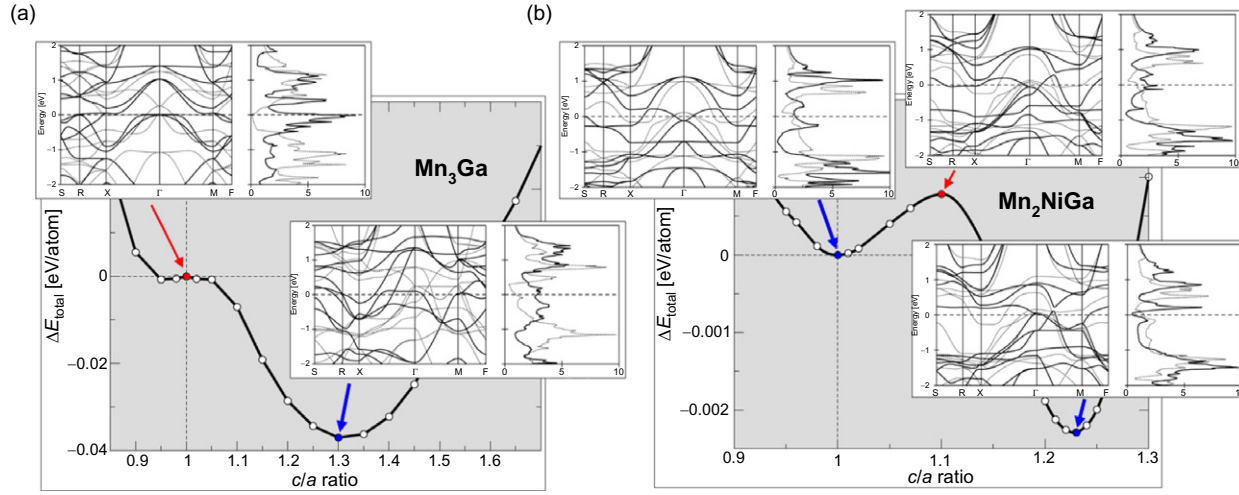


**Figure 1.24** Determination of the relative phase stability. The total energy difference between cubic and tetragonally distorted phases calculated as a function of  $c/a$ :  $E_{\text{total}} = E_{\text{total}}(c/a) - E_{\text{total}}(c/a = 1)$ . The red and blue dots mark the unstable and stable configurations, respectively. (a) Shows the  $\text{Mn}_3\text{Ga}$  system. The insets show the corresponding spin-resolved band structures and densities of states for the cubic ( $c/a = 1$ ) and distorted ( $c/a = 1.3$ ) cases. The bold curves correspond to the spin channel, which exhibits the van Hove singularity at  $\epsilon_F$  in the cubic case. The latter is obvious in the band structure (at  $R$ ,  $X$ ,  $\Gamma$ , and  $M$  symmetric points in the Brillouin zone, symmetry group 119) and leads to a high peak of DOS at  $\epsilon_F$  in this spin channel. The tetragonal distortion lifts this degeneracy by moving the states away from  $\epsilon_F$ , which reduces the DOS peaks and stabilizes the system at  $c/a = 1.3$ . (b) Shows the shape-memory alloy  $\text{Mn}_2\text{NiGa}$ . The system exhibits two stable states at  $c/a = 1$  and  $c/a = 1.23$ , both characterized by the absence of the van Hove singularities leading to a dip of DOS at  $\epsilon_F$ . In the unstable configuration ( $c/a = 1.1$ ), the singularity in  $R - Xk$  direction leads to a sharp DOS peak at  $\epsilon_F$ .

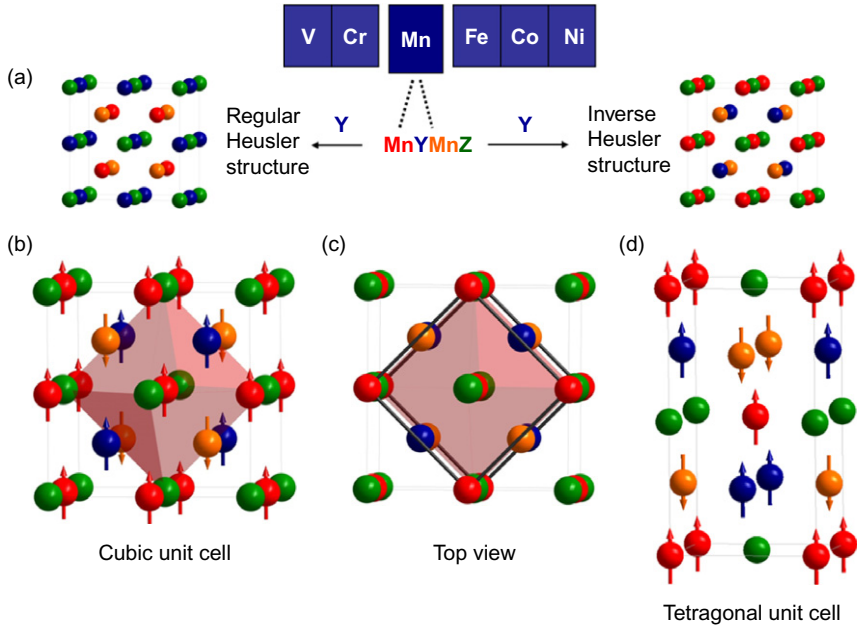


**Figure 1.25** Crystal structures of different types of  $\text{Mn}_2\text{YZ}$  Heusler compounds. (a) Shows the preferred structure chosen by a composition of arbitrary transition metals Y, which depend on their position in the periodic system and the electronic structure of the compound (van Hove singularity). (b–d) Show different views of an cubic inverse Heusler and the tetragonal inverse Heusler cells with three magnetic sublattices (red, blue, and orange spheres).

The tetragonal inverse  $\text{Mn}_2$ -based Heusler compounds are strongly preferable for STT since the interatomic distance between the Mn atoms on different lattice sites determines an antiferromagnetic coupling thus allowing for the desired low magnetic moments. Figure 1.26 shows the calculated MCA of tetragonal compounds and their experimental realization. Obviously, the MCA of the  $\text{Mn}_2$ -based compounds follow simple trends. First, it strongly depends on the number of valence electrons ( $N_V$ ), which is directly related to  $\Delta E$ , the distance from the van Hove singularity to  $\epsilon_F$ ; second, they scale up with the SOC by going from  $Y = \text{v}3d$  (Ni) via  $4d$  (Rh) to  $5d$  (Ir). The highest MCA was found for  $\text{Mn}_2\text{PtSn}$  (3.04 meV) but its low  $T_C$  (374 K) constitutes a drawback.  $\text{Mn}_3\text{Ga}$  with a calculated MCA of about 1 meV, which is in excellent agreement with the experimental observation (Winterlik et al., 2008), can already compete with the typical material used for the STT compound FePt (MCA is close to 3 meV; Lyubina et al., 2005). As the coercive fields of both materials are very similar, the difference in MCA is only due to the lower magnetic moment of  $\text{Mn}_3\text{Ga}$ , which is on

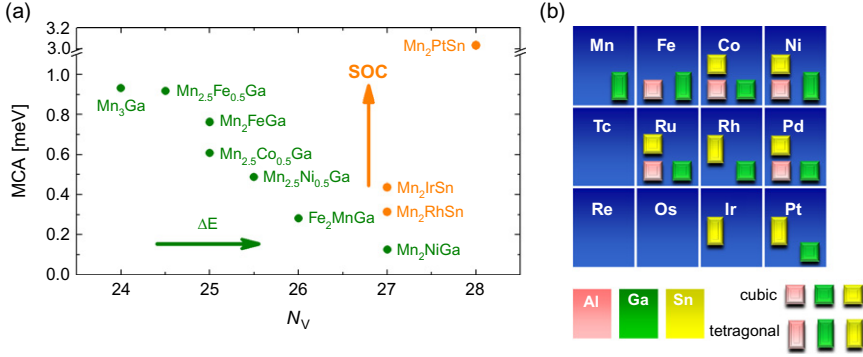


**Figure 1.26** MCA predicted for several tetragonal Heusler compounds and the experimental verification. The calculated MCA values are depicted in (a). The MCA of compounds with 3d Y elements increases upon decrease of  $\Delta E$  corresponding to a coincidence of van Hove singularity and  $\epsilon_F$ . MCA scales up with increasing SOC as well but at the expense of higher Gilbert damping. (b) Shows an overview of the synthesized and characterized “stoichiometric  $Mn_2YZ$  Heusler compounds” with  $Z = Al, Ga,$  and  $Sn$  found using the desing scheme described in the text.

the other hand necessary to ensure the sufficiently low switching current.  $Mn_3Ga$  also exhibits a substantially lower Gilbert damping (one order of magnitude) and much higher TMR. It is important to emphasize that the tetragonal distortion does not automatically guarantee the perpendicular alignment of magnetization as determined for the related tetragonal Heusler compounds  $Rh_2YZ$  (Gao et al., 2011) since the MCA oscillates as a function of  $c/a$ . But this feature can be verified by calculations.

Figure 1.26 gives an overview of the cubic and tetragonal  $Mn_2YZ$  Heusler compounds identified using this design scheme, synthesized, and characterized with respect to crystal structures and magnetism. Two trends were observed:  $Mn_2YGa$  compounds with the exception of  $Y = Co$  tend to form tetragonal structures with 3d elements at the Y position. In contrast, the 4d and 5d elements form only cubic  $Mn_2YGa$ . The opposite situation takes place in the  $Mn_2YSn$  series, which contains several tetragonal compounds with 4d and 5d elements, while only cubic (and hexagonal, not mentioned here) phases are found with 3d elements. Consequently, the lowest MCA were obtained in the known shape memory systems  $Mn_2NiGa$  and  $Fe_2MnGa$ . The tetragonal compounds with 3d elements in the Y position exhibit high MCA and high  $T_C$  of 500 K and above. The tetragonal compounds with 4d and 5d elements in the Y position exhibit high MCA but low coercivities, which are also related to their low  $T_C$ . Magnetic characterizations of the three Heusler systems  $Mn_{3-x}Fe_xGa$ ,  $Mn_{3-x}Co_xGa$ , and  $Mn_{3-x}Ni_xGa$  are shown in Fig. 1.27. The entire series of alloys investigated exhibits high  $T_C$ . The  $Mn_{3-x}Co_xGa$  system exhibits a feature

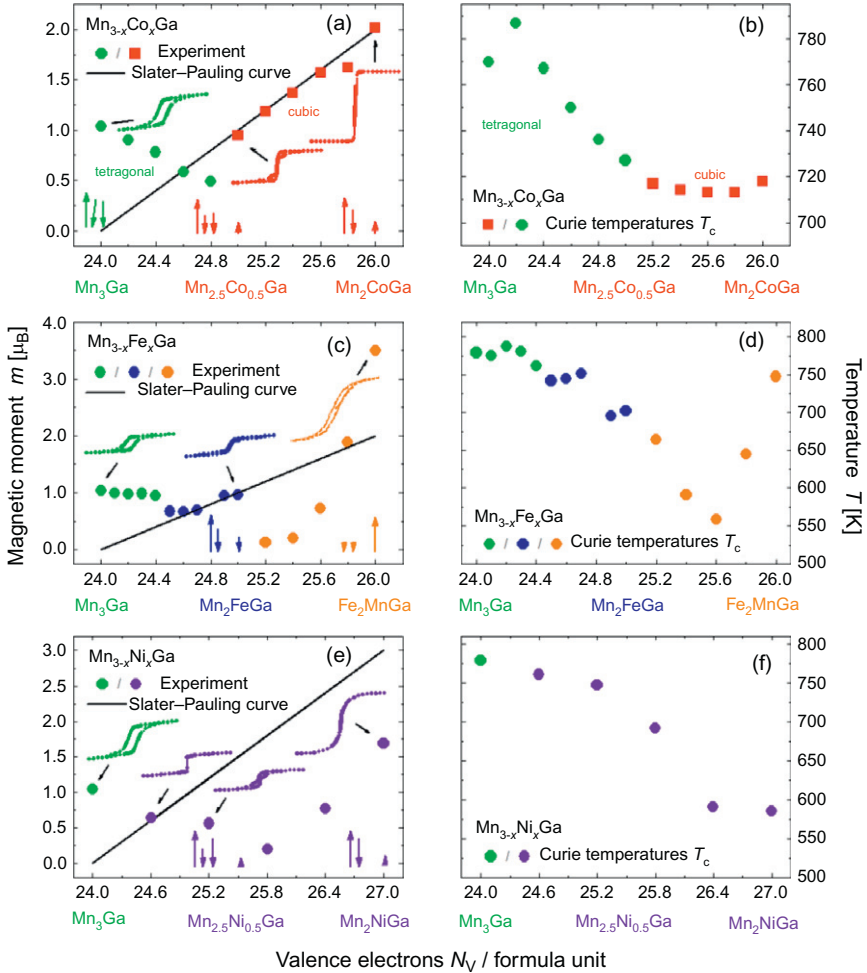


**Figure 1.27** Magnetic properties of  $\text{Mn}_{3-x}\text{Y}_x\text{Z}$  alloys, where  $\text{Y} = \text{Fe}, \text{Co}, \text{Ni}$ . (a), (c), and (e) show the experimentally determined saturation magnetic moments at  $T = 5\text{ K}$  compared to the Slater–Pauling values. Tetragonal and cubic compounds are represented by circles and squares, respectively. Heights and widths of the inserted hysteresis loops correspond to the factual ratios. The colored arrows represent the calculated local magnetic moments placed directly above the corresponding compositions. (b), (d), and (f) show the corresponding  $T_C$  of all alloys.

of special interest: while the tetragonal Mn-rich alloys are hard-magnetic and similar to  $\text{Mn}_{3-x}\text{Ga}$ , the cubic Co-rich alloys exhibit soft-magnetic hysteresis loops and follow the Slater–Pauling rule perfectly. These

characteristics facilitate the MCA tunability by simply varying the Co concentration. While the tetragonal alloys exhibit the features typically attractive for STT applications (high  $T_C$ , strong PMA, high spin polarization, low  $M_S$ ), the cubic systems represent the second big class of 100% spin-polarized half-metallic Heusler materials robustly following the Slater–Pauling rule as in case of the  $\text{Co}_2\text{YZ}$  compounds. The tetragonal  $\text{Mn}_{3-x}\text{Co}_x\text{Ga}$  alloys are still highly spin polarized due to a pseudogap in one spin channel. Tuning between the spin polarization on one hand, but on the other hand between high and low degrees of magnetic anisotropy offers the opportunity of tailoring the magnetic properties continuously as desired. The magnetic couplings in  $\text{Mn}_{3-x}\text{Co}_x\text{Ga}$  correspond to the arrangements shown in Fig. 1.1b and d. Co atoms are always tetrahedrally coordinated while Mn atoms are found in both tetrahedral and octahedral environments. Being next neighbors, they carry opposing spins.

The ferrimagnetic Mn-rich alloys  $\text{Mn}_{3-x}\text{Fe}_x\text{Ga}$  are similar to  $\text{Mn}_{3-x}\text{Ga}$  but exhibit smaller coercivity and magnetic remanence. The phases  $\text{Mn}_{2.5}\text{Fe}_{0.5}\text{Ga}$ – $\text{Mn}_2\text{FeGa}$  despite their tetragonal structures exhibit magnetic moments in agreement with the Slater–Pauling rule. An exceptional structure is found for  $\text{Mn}_2\text{FeGa}$ , which on a first glance appears to be completely disordered face-centered cubic (A1). The Rietveld analysis of the diffraction pattern, however, confirmed the inverse tetragonally distorted Heusler structure with a  $c/a$  ratio close to  $\sqrt{2}$ . Reducing the Fe amount only by 10% is sufficient to uncover the tetragonal splits of certain reflections. The Fe-rich phases show strong magnetic moments on Mn culminating in a magnetic moment of nearly  $4 \mu_B$  in  $\text{Fe}_2\text{MnGa}$ . The latter occurs due to decreasing contributions of the antiparallely aligned Fe spins. It was ascertained by Moessbauer spectroscopy that the Fe atoms carry only small magnetic moments (Winterlik et al., 2012). The magnetic moment is almost completely carried by the localized octahedral Mn atoms very similar to  $d^4 \text{Mn}^{3+}$  ions. While  $\text{Fe}_2\text{MnGa}$  is a shape memory compound, the Mn-rich alloys are interesting for the STT applications.

The alloys  $\text{Mn}_{3-x}\text{Ni}_x\text{Ga}$  show an exceptional variety of anisotropies and shapes of magnetic hysteresis loops. Mn doping of the known shape memory compound  $\text{Mn}^2\text{NiGa}$ , which is relatively soft-magnetic, leads first to a strong decrease of the magnetic moment ( $0.20 \mu_B$  for  $\text{Mn}_{2.4}\text{Ni}_{0.6}\text{Ga}$ ) but then, similar to  $\text{Mn}_{3-x}\text{Co}_x\text{Ga}$ , it increases up to the value of  $\text{Mn}_3\text{Ga}$ . Detailed information about the magnetic characteristics of the important tetragonal Heusler compositions is given in Table 1.2. Generally, in the alloys  $\text{Mn}_x\text{Fe}_x\text{Ga}$ ,  $\text{Mn}_{3-x}\text{Co}_x\text{Ga}$ , and  $\text{Mn}_{3-x}\text{Ni}_x\text{Ga}$  the magnetic moments decrease with decreasing Mn content, pass through a minimum, and then increase again. A similar trend has been observed in the corresponding  $T_C$  dependencies. For the different Y atoms all minima are found in the range within  $24.8 < N_V < 25.8$  electrons per formula unit. This very interesting feature is strongly related with the similarity of electronic structures of the alloys.



**Table 1.2** Magnetic properties of tetragonal Mn<sub>2</sub>-based Heusler compounds

Alloy	$N_V$	$c/a$	$m_S$	$T_C$	$H_c$
Mn <sub>3</sub> Ga	24	1.28	1.04	779	453
Mn <sub>2</sub> FeGa	25	1.43	0.96	702	56.9
Mn <sub>2.7</sub> Co <sub>0.3</sub> Ga	24.6	1.28	0.58	750	282
Mn <sub>2</sub> Ga	17	1.30	1.41	723	102
Mn <sub>2</sub> hSn	27	1.09	1.87	305	55.2
Mn <sub>2</sub> PtSn	28	0.95	3.69	374	78.8
Mn <sub>2</sub> NiGa	25	1.21	1.69	585	32.6

$N_V$  is the number of valence electrons per formula unit,  $m_S$  are the saturation magnetic moments,  $T_C$  the Curie temperatures, and  $H_c$  the coercivities.

This systematic approach of combining the indications for a possible tetragonal distortion from first-principles calculations and the subsequent experimental realization has opened the enormous phase space of tetragonal Mn<sub>2</sub>YZ Heusler compounds and corresponding alloys, which, in future, could provide ideal materials for the fabrication of universally applicable spintronic devices, combining many advantages and avoiding many disadvantages of state of the art. With respect to MTJ, Mn<sub>2</sub>-based Heusler compounds inherently offer all the prerequisites, which are currently only simulated by complex synthetic ferrimagnetic structures consisting multiple different layers. Substituted by a highly spin-polarized Heusler ferrimagnet, a lot of effort and loss of efficiency could be economized in future. Already now, Seagate technology invented a STT-MRAM which incorporates magnetic Heusler layers (Lou, 2010). TDK designed a multilayer device with PMA incorporating Heusler materials with high spin polarization and low magnetic damping (Zhang et al., 2009c).

### 7.1. Tetragonal Heusler compounds for shape-memory and magnetocaloric applications

The recently discovered tetragonal Heusler compounds open up many possibilities in the field of shape memory materials, and novel applications in the field of magnetocalorics as well as potential RE-free hard magnets.

Today, the Ni<sub>2</sub>MnGa system is one of the most intensively investigated materials owing to its shape memory behavior and its potential application in actuator devices, in which strains are controlled by the application of an external magnetic field. In this system, the cubic phase undergoes a ferro-magnetic transition at  $T_C=376\text{K}$  (Webster et al., 1984). Additionally, stoichiometric Ni<sub>2</sub>MnGa undergoes a structural phase transition at  $T_M=202\text{K}$  from the high-temperature cubic L2<sub>1</sub> structure to a low-temperature martensite phase (Webster et al., 1984). Due to the reversibility of this structural transition, a shape memory effect is observed in this system.

Moreover, the crystal structure of the martensite phase in Ni–Mn–Ga system can be modulated or unmodulated to be orthorhombic, tetragonal, or monoclinic (Brown et al., 2002; Kokorin et al., 1992; Martynov and Kokorin, 1992; Pons et al., 1999). In case of a tetragonal martensite phase, the cubic unit cell is contracted along one (001) axis and extended along the other two. Since this transformation is diffusion less, large stresses have to be stored and accommodated in the martensite microstructure. As a consequence, the minimization of the strain energy leads to the formation of a number of crystallographic domains, known as variants. In this case, the original cubic cell allows the formation of three different variants, depending on which axis is contracted. A typical martensite microstructure consists of mixtures of the three variants, in which two adjacent variants meet at one of the two possible well-defined interfaces, called twin planes (compare Fig. 1.28). While each of these variants has a unique orientation, defined by its  $c$ -axis, the martensite phase is essentially in a polycrystalline state, composed of variable volume fractions of these three variants. In ferromagnetic shape memory alloys, such as Ni<sub>2</sub>MnGa, a magnetic field can move these twin planes. Variants, in which the easy-axis of magnetization is aligned in parallel to the external field, grow preferentially at expense of variants with different orientation, resulting in macroscopic strains of up to 10% (Sozinov et al., 2002).

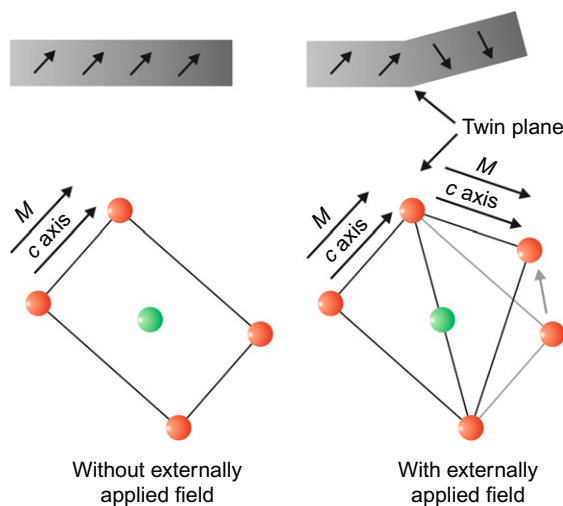


**Figure 1.28** Schematic views of a sample in the martensite phase are shown at the top. The direction of magnetization is indicated by the arrows. At the bottom, the orientation of the martensitic unit cell is sketched on the left-hand side, and the twinned martensitic cell is displayed on the right. Reprinted from Graf et al. (2011a) with kind permission of Elsevier.

To provide the necessary driving force for twin boundary motion in moderate magnetic fields ( $\approx 1\text{--}2\text{ T}$ ), the presence of strong magnetoelastic coupling on the mesoscopic length-scale is essential. This condition is fulfilled in Ni–Mn–Ga shape memory alloys, in which the magnetocrystalline anisotropy energy and the magnetization are sufficiently high in the martensite phase (O’Handley et al., 2000; Tickle and James, 1999). On a microscopic length-scale, however, strong magnetic coupling leads to large strains. In contrast to the Ni–Mn–Ga system, where the saturation magnetization in the martensite phase is higher than in the  $L2_1$  austenite phase, the magnetization in Ni–Mn–Z, Z = In, Sn, or Sb is lower in the martensite phase than in the  $L2_1$  austenite phase (Khan et al., 2007, 2008; Krenke et al., 2005a, 2006). Therefore, a magnetic field applied to the martensite phase can shift the transition to sufficiently low temperatures and stabilize the austenite phase giving rise to a field-induced reverse martensite transformation (FIRMT) (Kainuma et al., 2006a; Planes et al., 2009). In fact, such transitions were observed in the Heusler-based materials  $\text{Ni}_{50}\text{Mn}_{36}\text{Sn}_{14}$  and  $\text{Ni}_{50}\text{Mn}_{36}\text{In}_{14}$  by neutron and X-ray diffraction measurements in magnetic fields (Koyama et al., 2006; Krenke et al., 2007), and are also classified as metamagnetic transitions (Kainuma et al., 2006b).

On the other hand, in Ni–Mn–Ga-based shape-memory alloys the volume does not change when the structural phase transition takes place, and the rate of change in the martensite start temperature range with applied field is comparably small ( $|dT_M/dH| \approx 1\text{--}2\text{ K T}^{-1}$ ) (Dikshtein et al., 2000; Marcos et al., 2002). Therefore, field-induced strains superimpose on the larger strain, which is caused by twin boundary motion, and thus, strains associated with any field-induced transformation become negligible compared to those originating from twin-boundary motion. Contrary to this, the structural phase transition is distinctly affected by an applied magnetic field in Ni–Mn–Z (Z = In, Sn, or Sb)-based materials and a unit cell volume change between the austenite and the martensite transition of  $\approx 0.4\%$  (Kanomata et al., 2008; Koyama et al., 2006). Such volume changes can lead to large strains and barocaloric effects at the FIRMT (Kanomata et al., 2008). The rate of change in the transition temperature with the magnetic field can be as high as  $\approx -10\text{ K T}^{-1}$  in some of these materials, which can result in magnetic superelasticity (large reversible magnetic field-induced strains) (Krenke et al., 2007).

Another interesting feature is the tunability of both critical temperatures by alloying in the Ni–Mn–Ga-based system: Changing the relation between  $T_M$  and  $T_C$  results in different properties, which makes these alloys promising for technological applications. For example, in  $\text{Ni}_{2+x}\text{Mn}_{1-x}\text{Ga}$  with  $0.18 \leq x \leq 0.20$ , a coupling of the magnetic and the structural transition takes place, because the transition temperatures are close to each other (Khovaylo et al., 2005). Consequently, it becomes possible not only to achieve a shape memory effect by applying an external magnetic field, but also to induce attractive properties such as the giant magnetocaloric effect,

magnetostriction, and MR, which are important for magnetic refrigeration or magnetostrictive transducers (Marcos et al., 2003; Murray et al., 2000; Sharma et al., 2006; Sozinov et al., 2002; Zhou et al., 2004). However, for  $x \geq 0.3$   $T_M$  is higher than  $T_C$ , and therefore, the martensite transition occurs in the paramagnetic region. Since  $T_M$  increases dramatically with increasing  $x$ , alloys with a high Ni excess can be used as high temperature shape memory alloys. Here again, the total electron count is an easy, but reliable way to qualitatively understand the relation between composition and transition temperatures. For example, it was shown, that an increasing number of valence electrons lowers  $T_M$  (Lanska et al., 2004). However, a profound understanding of the physical properties is needed, to design new materials with predictable properties. For this purpose, first-principles calculations can give an insight into the complex relation between concentration dependent properties and the transition temperatures (Li et al., 2010).

The ternary phase diagram of the Ni–Mn–Ga system was mapped to search for new shape memory alloys and for a systematic relation between  $T_C$  and  $T_M$  in a wide range of compositions (Takeuchi et al., 2003). Generally, the transition temperature increases as the molecular percentage of Ga is decreased, which in turn results in a non-Heusler composition. A typical composition is  $\text{Ni}_{43}\text{Mn}_{47}\text{Ga}_{10}$  whose martensite transition starts at 400 K making this system particularly interesting for technological applications. Based on these findings it can be concluded that a Ga-induced structural instability in the ferromagnetic/antiferromagnetic transition region of  $\text{Ni}_{1-x}\text{Mn}_x$  is the origin of the martensite transition in the Ni–Mn–Ga system.

For a technical application of magnetic shape memory materials, such as actuators with a long stroke and high precision, Ni–Mn–Ga-based materials are extremely well suitable due to their very high-magnetic field-induced strain (up to 10%) and their full shape recovery over  $\leq 10^8$  mechanical cycles (Chmielusz et al., 2008). For a long time these very large effects could only be achieved for single crystals. Compared to monocrystalline Ni–Mn–Ga, fine-grained Ni–Mn–Ga is much easier to process but shows near-zero strains because twin boundary motion is inhibited by constraints imposed by grain boundaries (Gaitzsch et al., 2006, 2007; Pötschke et al., 2007). A new approach to maintaining the ease of processing and reduce the constraints imposed by grain boundaries by introducing porosity in Ni–Mn–Ga (Chmielusz et al., 2009). This leads to magnetic field-induced strains of 2.0–8.7% being stable for more than 200,000 cycles and which are larger than those of any polycrystalline, active material.

In addition to the above mentioned giant magnetocaloric effect in Ni–Mn–Ga materials, where the structural and magnetic transition temperatures are close to each other, samples close to the  $\text{Ni}_2\text{MnGa}$  stoichiometry show an inverse magnetocaloric effect (Marcos et al., 2003), in which the adiabatical application of a magnetic field leads to a cooling of the sample. In the case of  $\text{Ni}_2\text{MnGa}$ , the effect, however, vanishes as the magnetic field increases, and the standard magnetocaloric effect is observed at high fields. on the other hand,

for the  $\text{Ni}_{0.50}\text{Mn}_{0.50-x}\text{Sn}_x$  system with compositions lying in the narrow range of  $0.13 \leq x \leq 0.15$  an inverse magnetocaloric effect was observed that is three times larger than in Ni–Mn–Ga-based compounds (Krenke et al., 2005b). The potential technological application of inverse magnetocaloric effects are manifold since they open up the possibility of increasing room-temperature refrigeration efficiency by using materials showing this effect in combination with a conventional magnetocaloric material.

Recently, the observation of a giant barocaloric effect in the Ni–Mn–In system was reported (Mañosa et al., 2010). This effect is based on the isothermal entropy change or adiabatic temperature change by application or withdrawal of external pressure. Today, this effect is used in most present cooling technologies that are based on the compression and expansion cycles of gases. The value for the barocaloric effect of  $24.4 \text{ J kg}^{-1} \text{ K}^{-1}$  under a hydrostatic pressure of 2.6 kbar at ambient temperatures is 20 times larger than the value resulting from elastic heating (Mañosa et al., 2010) and is comparable to the best values reported in giant magnetocaloric materials (Brück, 2005; Gschneidner et al., 2005). Interestingly, the physical origin of the barocaloric effect found in the Ni–Mn–In system is the same as that reported for the inverse magnetocaloric effect, that is, the large entropy change that accompanies the structural (martensite) transition, which can be induced either by magnetic field or by hydrostatic pressure, or even a combination of both (multicaloric effect).

Shape memory materials were expanded to a large number of compounds, for instance  $\text{Ni}_2\text{MnAl}$ ,  $\text{Co}_2\text{NbSn}$  and  $\text{Fe}_2\text{MnGa}$  (Mañosa et al., 2004; Wolter et al., 2002; Zhu et al., 2009) and also quaternary compounds were investigated in this context (Ito et al., 2008; Kainuma et al., 2008), for example, a magnetic field-induced shape recovery was reported for compressively deformed  $\text{NiCoMnIn}$  (Kainuma et al., 2006a). Stresses of more than 100 MPa can be generated in this material by application of a magnetic field. The observed deformation of  $\approx 3\%$  is fully recovered to the original shape of the material which is attributed to a reverse transformation from the antiferromagnetic (or paramagnetic) martensite state to the ferromagnetic parent phase in  $\text{Ni}_{45}\text{Co}_5\text{Mn}_{36.7}\text{In}_{13.3}$  single crystals.

The shape memory compounds  $\text{Ni}_2\text{MnZ}$  show additionally exchange bias behavior at low temperatures (Brown et al., 2006; Khan et al., 2007). The stoichiometric  $\text{Ni}_2\text{MnZ}$ -based compounds stabilize in the cubic phase with ferromagnetic ordering (Krenke et al., 2005a). Most of the important functional properties in this system arise because of an austenite to martensitic structural phase transition resulting from substitution of excess Mn at the Z position (Kainuma et al., 2006a; Krenke et al., 2005a,b, 2006; Ullakko et al., 1996). The excess Mn occupying the Z sites couple antiferromagnetically with the Mn at the regular Y sites (Aksoy et al., 2009; Brown et al., 2006). In these off-stoichiometric alloys, the presence of antiferromagnetic interaction in a ferromagnetic matrix is responsible for the exchange bias behavior (Khan et al., 2007; Xuan et al., 2010). Also in the  $\text{Mn}_2\text{YZ}$  family with many

unexplored compounds a large exchange bias in off stoichiometric members is likely. Just recently a large exchange bias was observed in  $\text{Mn}_2\text{PtIn}$  (Nayak et al., 2012). The exchange bias behavior in  $\text{Mn}_2\text{PtIn}$  is argued to originate from the glassy nature of the low temperature magnetic state. Although the strength of the exchange bias filed in the present system is not large, the demonstrated feasibility of achieving large PMA along with presence of exchange bias behavior can motivate the search for other Heusler alloys with further improved properties for potential multifunctional applications.

One of the major important opportunities besides the magnetic shape memory applications is the concept of ferroic cooling, which could allow for strongly reducing the energy sink of refrigeration. Furthermore, the effects for the environment are also beneficial because greenhouse gases or ozone depleting substances are no longer required in refrigerators, which could thus become smaller, environmentally friendly, and less noisy compared to state of the art. The underlying principle for operating the cooling cycle with solid state matter is based on the magnetocaloric effect (MCE) (Tegus et al., 2002), which is well known for its use for accomplishing extremely low temperatures by isothermal magnetization and adiabatic demagnetization. The discovery of giant MCE facilitates ferroic cooling at operating temperatures in the region of RT (Gutfleisch et al., 2011; Pecharsky and Gscheidner, 1997). The first promising alloys were based on RE elements such as  $\text{Gd}_5(\text{Si}_2\text{Ge}_2)$  or  $\text{La}(\text{Fe,Si})_{13}$  (Gutfleisch et al., 2005). As large amounts of materials are required for employment in refrigerators, economy and nowadays also political reasons dictate the use of cheap materials with good availability. Therefore designing the new materials “RE free” is presently among the most important requirements. Another big class of magnetocaloric materials are the MnAs-based compounds (Wada and Tanabe, 2001). This type of materials fulfills the prerequisite of low cost, but the toxicity of As certainly constitutes a major drawback when thinking of mass production.

Considering the drawbacks of the competitor materials the Heusler compounds nowadays represent the most promising class, which offers obviously many advantages. Design of Heusler compounds with specific magnetic and structural properties is possible because the materials usually follow simple trends based on their electron count and are therefore to a large amount predictable. It is furthermore possible to design them cheap, nontoxic, and RE free. The most prominent example of a Heusler compound with suitable magnetocaloric properties is  $\text{Ni}_2\text{MnGa}$  (Webster et al., 1984) with a martensitic transition at approximately 220 K. In the vicinity of the martensitic-transition temperature a large change of magnetization at low applied magnetic fields takes place, which is due to the difference of magnetocrystalline anisotropy between the cubic austenitic and tetragonal martensitic phases. In the best case scenario, the structural and the magnetic transition occur at identical temperatures thus maximizing the MCE (Pareti et al., 2003). The martensitic transitions of magnetocaloric Heusler

compounds can be tuned by modifying their stoichiometry. This way the transitions can easily be shifted to RT or the temperature region desired. The related Heusler compound  $\text{Mn}_2\text{NiGa}$  came to center of attention due to its comparably high Curie temperature and its martensitic transition close to RT (compare also Fig. 1.29) (Blum et al., 2011; Liu et al., 2005).

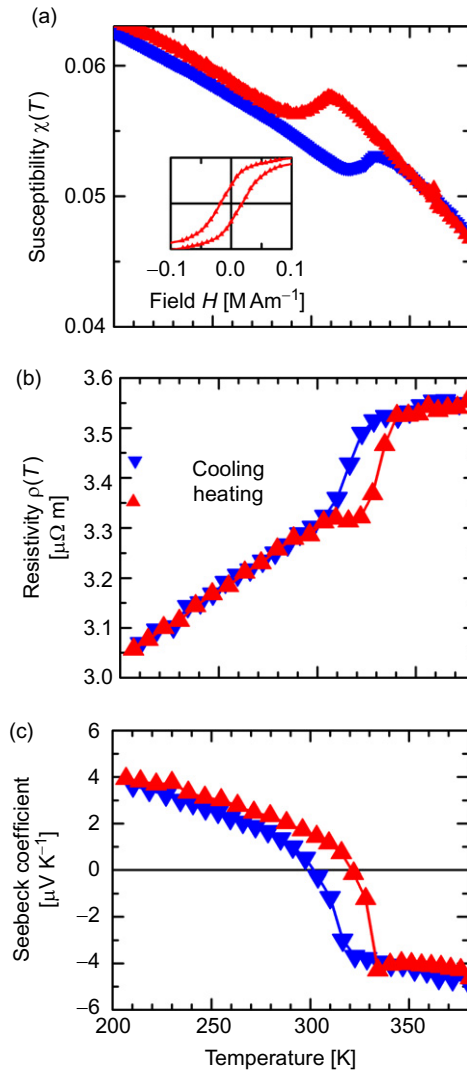


**Figure 1.29** Temperature dependence of the magnetic and transport properties for  $\text{Mn}_2\text{NiGa}$ . Shown are (a) magnetic susceptibility  $\chi(T)$  using a field of 5 T (the inset shows the magnetization hysteresis at 200 K), (b) electrical resistivity  $\rho(T)$ , and (c) Seebeck coefficient  $S(T)$ . Data taken from Blum et al. (2011).

However, this compound exhibits the drawback of a low magnetic moment, which limits the desired large changes of magnetic entropy.

Several Heusler compounds were reported to exhibit a giant inverse MCE, among them the NiMnSn alloys (Krenke et al., 2005b). In practice this means that application of a magnetic field on a material with inverse MCE causes cooling. This corresponds to an increase of entropy when a magnetic field is applied and is observed when first-order magnetic transitions such as antiferromagnetic/ferromagnetic or ferrimagnetic/ferromagnetic take place. In fact Heusler compounds can exhibit both, regular and inverse MCE due to competing interactions of different magnetic sublattices, especially when Mn is present, dependent on the distance between the corresponding lattice sites occupied by these atoms. Combining materials exhibiting both of these effects could increase the power of cooling devices. Currently, the most promising magnetocaloric Heusler compounds are based on Ni–Mn–In–Co (Liu et al., 2008). The drawbacks, which have to be overcome in future to allow for technological implementation of ferroic cooling are reducing the currently achieved hysteresis losses and, concerning the Heusler compounds, reducing their brittleness. Improved brittleness could be achieved by producing composites, that is, introducing polymers into the MCE materials (Liu et al., 2009). An fruitful Ansatz for reducing the hysteresis losses of Heusler compounds could be a modified synthesis using melt-spinning, which was shown to work for the giant MCE material  $\text{LaFe}_{13-x}\text{Si}_x$  in the form of melt spun ribbons, which exhibited a much larger MCE and less hysteresis loss compared to the corresponding bulk materials (Gutfleisch et al., 2005).

## 8. SUMMARY AND OUTLOOK

Cubic Heusler compounds and their tetragonal cousins are a remarkable and predictable class of ferromagnetic, ferrimagnetic, and antiferromagnetic materials. These apparently complex ternary compounds show an outstandingly wide range of properties and tunability, including HMFs, shape memory alloys, ferro- and ferrimagnetic metals, and semiconducting compounds. In particular, most of the  $\text{Co}_2\text{YZ}$  and the  $\text{Mn}_2\text{YZ}$  ( $\text{Y}$  = transition metal,  $\text{Z}$  = main group element) are half-metallic ferro- or ferrimagnets. Due to their flexibility both in microstructure and electronic structure, Heusler alloys offer a toolbox where scientists can realize demanding and seemingly contradictory properties within one material. For example, Skyrmions, giant exchange bias, and RE-free hard magnets within this family of compounds are to be discovered in near future. Furthermore, novel artificial and multifunctional properties can be realized by layer-by-layer deposition of thin films. The development departments of



companies including Hitachi, IBM, Seagate, and Western Digital are already working with Heusler compounds such as  $\text{Co}_2\text{FeSi}$  for electrodes in next-generation read heads for high capacity disk-drives representing the high impact of Heusler compounds for applications in spintronics. Challenges are still the control of disorder and interface on an atomistic scale. The design and optimization of suitable materials for complex devices is a field of ongoing active research and maybe will lead to the production of an universal spintronics device.

## ACKNOWLEDGMENTS

The authors thank B. Balke, A. Beleanu, C. G. F. Blum, F. Casper, S. Chadov, T. Gruhn, V. Jung, J. Kübler, V. Ksenofontov, S. Ouardi, T.D. Schladt, M. Schwall, and S. Wurmehl for providing data and for many fruitful discussions.

Financial support by the Deutsche Forschungsgemeinschaft (Project TP 2.3-A in research unit FOR 1464 “ASPIMATT” and GR4000/1-1) is gratefully acknowledged.

## REFERENCES

- Aksoy, S., Acet, M., Deen, P.P., Manosa, L., Planes, A., 2009. *Phys. Rev. B* **79**, 212401.
- Alijani, V., Fecher, G.H., Winterlik, J., Naghavi, S.S., Felser, C., 2011a. *Phys. Rev. B* **83**, 184428.
- Alijani, V., Ouardi, S., Fecher, G.H., Balke, B., Winterlik, J., Beleanu, A., Kozina, X., Stryganyuk, G., Felser, C., Bernardi, F., Morais, J., Ikenaga, E., *et al.*, 2011b. *Phys. Rev. B* **84**, 224416.
- Alijani, V., Winterlik, J., Fecher, G.H., Felser, C., 2011c. *Appl. Phys. Lett.* **99**, 222510.
- Alijani, V., Winterlik, J., Fecher, G.H., Naghavi, S.S., Chadov, S., Gruhn, T., Felser, C., 2012. *J. Phys. Condens. Matter* **24**, 046001.
- Ambrose, T., Krebs, J.J., Prinz, G.A., 2000. *Appl. Phys. Lett.* **76**, 3280.
- Anisimov, V.I., Aryasetiawan, F., Lichtenstein, A.I., 1997. *J. Phys. Condens. Matter* **9**, 767.
- Antonov, V.N., Dürr, H.A., Kucherenko, Y., Bekenov, L.V., Yaresko, A.N., 2005. *Phys. Rev. B* **72**, 054441.
- Attema, J.J., Fang, C.M., Chioncel, L., de Wijs, G.A., Lichtenstein, I.A., de Groot, R.A., 2004. *J. Phys. Condens. Matter* **15**, S5517.
- Auth, N., Jakob, G., Block, T., Felser, C., 2003. *Phys. Rev. B* **68**, 024403.
- Bach, P., Bader, A.S., Rusten, C., Gould, C., Becker, C.R., Schmidt, G., Molenkamp, L. W., Weigand, W., Kumpf, C., Umbach, E., Urban, R., Woltersdorf, G., *et al.*, 2003. *Appl. Phys. Lett.* **83**, 521.
- Bacon, G.E., Plant, J.S., 1971. *J. Phys. F: Met. Phys.* **1**, 524.
- Balke, B., Fecher, G.H., Kandpal, H.C., Felser, C., Kobayashi, K., Ikenaga, E., Kim, J.-J., Ueda, S., 2006. *Phys. Rev. B* **74**, 104405.
- Balke, B., Fecher, G.H., Winterlik, J., Felser, C., 2007a. *Appl. Phys. Lett.* **90**, 152504.
- Balke, B., Wurmehl, S., Fecher, G.H., Felser, C., Alves, M.C.M., Bernardi, F., Morais, J., 2007b. *Appl. Phys. Lett.* **90**, 172501.
- Balke, B., Fecher, G.H., Gloskovskii, A., Barth, J., Kroth, K., Felser, C., Robert, R., Weidenkaff, A., 2008. *Phys. Rev. B* **77**, 045209.
- Balke, B., Ouardi, S., Graf, T., Barth, J., Blum, C.G.F., Fecher, G.H., Shkabko, A., Weidenkaff, A., Felser, C., 2010. *Solid State Commun.* **150**, 529.
- Bandyopadhyay, T., Sarma, D.D., 1989. *Phys. Rev. B* **39**, 3517.

- Barman, A., Wang, S., Hellwig, O., Berger, A., Fullerton, E.E., Schmidt, H., 2007. *J. Appl. Phys.* **101**, 09D102.
- Barth, J., Fecher, G.H., Balke, B., Ouardi, S., Graf, T., Felser, C., Shkabko, A., Weidenkaff, A., Klaer, P., Elmers, H.-J., Yoshikawa, H., Ueda, S., *et al.*, 2010. *Phys. Rev. B* **81**, 064404.
- Basit, L., Fecher, G., Chadov, S., Balke, B., Felser, C., 2011. *Eur. J. Inorg. Chem.* 3950.
- Berger, L., 1996. *Phys. Rev. B* **54**, 9353.
- Bernevig, B.A., Zhang, S.C., 2006. *Phys. Rev. Lett.* **96**, 106802.
- Bernevig, B.A., Hughes, T.L., Zhang, S.-C., 2006. *Science* **314**, 1757.
- Bhattacharya, S., Pope, A.L., Littleton, R.T. IV, Tritt, T.M., Ponnambalam, V., Xia, Y., Poon, S.J., 2000. *Appl. Phys. Lett.* **77**, 2476.
- Block, T., Felser, C., Jakob, G., Ensling, J., Mühling, B., Gütlich, P., Beaumont, V., Studer, F., Cava, R.J., 2003. *J. Solid State Chem.* **176**, 646.
- Block, T., Wurmehl, S., Felser, C., Windeln, J., 2006. *Appl. Phys. Lett.* **88**, 202504.
- Blum, C.G.F., Ouardi, S., Fecher, G.H., Balke, B., Kozina, X., Stryanyuk, G., Ueda, S., Kobayashi, K., Felser, C., Wurmehl, S., Büchner, B., 2011. *Appl. Phys. Lett.* **98**, 252501.
- Bona, G.L., Meier, F., Taborelli, M., Bucher, E., Schmidt, P.H., 1985. *Solid State Commun.* **56**, 391.
- Borca, C.N., Komesu, T., Jeong, H.-K., Dowben, P.A., Ristoiu, D., Hordequin, C., Nozieres, J.P., Pierre, J., Stadler, S., Idzerda, Y.U., 2001. *Phys. Rev. B* **64**, 052409.
- Bradley, A.J., Rodgers, J.W., 1934. *Proc. Royal Soc. A* **144**, 340.
- Brooks, J.S., Williams, J.M., 1975. *Phys. Stat. Sol. A* **32**, 413.
- Brown, P.J., Crangle, J., Kanomata, T., Matsumoto, M., Neumann, K.-U., Ouladdiaf, B., Ziebeck, K.R.A., 2002. *J. Phys. Condens. Matter* **14**, 10159.
- Brown, P.J., Gandy, A.P., Ishida, K., Kainuma, R., Kanomata, K.T., Neumann, K.U., Oikawa, K., Ouladdiaf, B., Ziebeck, K.R.A., 2006. *J. Phys. Condens. Matter* **18**, 2249.
- Brück, E., 2005. *J. Phys. D: Appl. Phys.* **38**, R381.
- Buschow, K.H.J., van Engen, P., 1981. *J. Magn. Magn. Mater.* **25**, 90.
- Butler, W.H., Zhang, X.-G., Schulthess, T.C., MacLaren, J.M., 2001. *Phys. Rev. B* **63**, 054416.
- Butler, W.H., Mewes, C.K.A., Liu C., T. Xu, 2011. arXiv:1103.3855v1.
- Canfield, P.C., Thompson, J.D., Beyermann, W.P., Lacerda, A., Hundley, M.F., Peterson, Z., Fisk, E., Ott, H.R., 1991. *J. Appl. Phys.* **70**, 5800.
- Carey, M.J., Block, T., Gurney, B.A., 2004. *Appl. Phys. Lett.* **85**, 4442.
- Carey, M. J., Childress, J. R., Maat, S., 2008. US Patent 2008/0112095.
- Casper, F., Felser, C., 2008. *Solid State Commun.* **148**, 175.
- Casper, F., Ksenofontov, V., Kandpal, H.C., Reiman, S., Shishido, T., Takahashi, M., Takeda, M., Felser, C., 2006. *Z. Allgem. Anorg. Chem.* **632**, 1273.
- Casper, F., Seshari, R., Felser, C., 2009. *Phys. Stat. Sol. A* **206**, 1090.
- Chadov, S., Fecher, G.H., Felser, C., Minár, J., Braun, J., Ebert, H., 2009. *J. Phys. D: Appl. Phys.* **42**, 084002.
- Chadov, S., Qi, X., Kübler, J., Fecher, G.H., Felser, C., Zhang, S.C., 2010. *Nat. Mater.* **9**, 541.
- Chadov, S., Graf, T., Chadova, K., Dai, X., Casper, F., Fecher, G.H., Felser, C., 2011. *Phys. Rev. Lett.* **107**, 047202.
- Chen, Y.-L., Analyti, J.G., Chu, J.-H., Liu, Z.-K., Mu, S.-K., Qi, X.-L., Zhang, H.-J., Lu, D.-H., Dai, X., Fang, Z., Zhang, S.-C., Fisher, I.R., *et al.*, 2009. *Science* **325**, 178.
- Chmielus, M., Chernenko, V.A., Knowlton, W.B., Kosterz, G., Müllner, P., 2008. *Eur. Phys. J. Special Topics* **158**, 79.

- Chmielus, M., Zhang, X.X., Witherspoon, C., Dunand, D.C., Muellner, P., 2009. *Nat. Mater.* **8**, 863.
- Clifford, E., Venkatesan, M., Gunning, R., Coey, J.M.D., 2004. *Solid State Commun.* **131**, 61.
- Conca, A., Jourdan, M., Adrian, H., 2007. *J. Phys. D: Appl. Phys.* **40**, 1534.
- Dai, X., Hughes, T.L., Qi, X.-L., Fang, Z., Zhang, S.-C., 2008. *Phys. Rev. B* **77**, 125319.
- de Groot, R.A., 1991. *Phys. B* **172**, 45.
- de Groot, R.A., Mueller, F.M., Van Engen, P.G., Buschow, K.H.J., 1983. *Phys. Rev. Lett.* **50**, 2024.
- de Groot, R.A., van der Kraan, A.M., Buschow, K.H.J., 1986. *J. Magn. Magn. Mater.* **61**, 330.
- Deng, Z., Jin, C., Liu, Q., Wang, X., Zhu, J., Feng, S., Chen, L., Yu, R., Arguello, C., Goko, T., Ning, F., Zhang, J., *et al.*, 2011. *Nat. Commun.* **2**, 422.
- de Wijs, G.A., de Groot, R.A., 2001. *Phys. Rev. B* **64**, 020402.
- Dikshteĭn, I.E., Ermakov, D.I., Koledov, V.V., Koledov, L.V., Takagi, T., Tulaĭkova, A.A., Cherechultin, A.A., Sharov, V.G., 2000. *JETP Lett.* **72**, 373.
- Dong, X.Y., Adelman, C., Xie, J.Q., Palmstrøm, C.J., Lou, X., Strand, J., Crowell, P.A., Barnes, J.-P., Petford-Long, A.K., 2005. *Appl. Phys. Lett.* **86**, 102107.
- Ebert, H., Schütz, G., 1991. *J. Appl. Phys.* **69**, 4627.
- Ebke, D., Thomas, A., Hütten, A., Balke, B., Felser, C., Schmalhorst, J., Reiss, G., 2008. *Phys. Stat. Sol. A* **205**, 2298.
- Edmonds, K.W., Wang, K.Y., Campion, R.P., Neumann, A.C., Farley, N.R.S., Gallagher, B.L., Foxon, C.T., 2002. *Appl. Phys. Lett.* **81**, 4991.
- Elmers, H.-J., Fecher, G.H., Valdaitsev, D., Nepijko, S.A., Gloskovskii, A., Jakob, G., Schönhense, G., Wurmehl, S., Block, T., Felser, C., Hsu, P.-C., Tsai, W.-L., *et al.*, 2003. *Phys. Rev. B* **67**, 104412.
- Fecher, G.H., Felser, C., 2007. *J. Phys. D: Appl. Phys.* **40**, 1582.
- Fecher, G.H., Kandpal, H.C., Wurmehl, S., Morais, J., Lin, H.-J., Elmers, H.-J., Schönhense, G., Felser, C., 2005. *J. Phys. Condens. Matter* **17**, 7237.
- Fecher, G.H., Kandpal, H.C., Wurmehl, S., Felser, C., Schönhense, G., 2006. *J. Appl. Phys.* **99**, 08J106.
- Fecher, G.H., Balke, B., Ouardi, S., Felser, C., Schönhense, G., Ikenaga, E., Kim, J.-J., Ueda, S., Kobayashi, K., 2007. *J. Phys. D: Appl. Phys.* **40**, 1576.
- Felser, C., Seshadri, R., 2000. *Int. J. Inorg. Mater.* **6**, 677.
- Felser, C., Ahn, K., Kremer, R.K., Seshadri, R., Simon, A.J., 1999. *J. Solid State Chem.* **147**, 19.
- Felser, C., Heitkamp, B., Kronast, F., Schmitz, D., Cramm, S., Dürr, H.A., Elmers, H.-J., Fecher, G.H., Wurmehl, S., Block, T., Valdaitsev, D., Nepijko, S.A., *et al.*, 2003. *J. Phys. Condens. Matter* **15**, 7019.
- Felser, C., Fecher, G.H., Balke, B., 2007. *Angew. Chem. Int. Ed.* **46**, 668.
- Felser, C., Casper, F., Dai, X., Reiss, G., 2010. Patent DE102008046920.3.
- Flude, P., 1995. *Electron Correlations in Molecules and Solids*. 3rd ed. Springer Verlag, Heidelberg.
- Fu, L., Kane, C.L., 2007. *Phys. Rev. Lett.* **98**, 106803.
- Fujii, S., Sugimura, S., Ishida, S., Asano, S., 1990. *J. Phys. Condens. Matter* **2**, 8583.
- Furubayashi, T., Kodama, K., Sukegawa, H., Takahashi, Y.K., Inomata, K., Hono, K., 2008. *Appl. Phys. Lett.* **93**, 122507.
- Gaitzsch, U., Roth, S., Rellinghaus, B., Schultz, L., 2006. *J. Magn. Magn. Mater.* **305**, 275.
- Gaitzsch, U., Pötschke, M., Roth, S., Rellinghaus, B., Schultz, L., 2007. *Scr. Mater.* **57**, 493.
- Galanakis, I., 2002. *J. Phys. Condens. Matter* **14**, 6329.
- Galanakis, I., 2004. *J. Phys. Condens. Matter* **16**, 8007.

- Galanakis, I., Dederichs, P., 2005. *Halfmetallic Alloys (Lecture Notes in Physics)* Vol. 676, Springer Verlag, Berlin.
- Galanakis, I., Ostanin, S., Alouani, M., Dreyse, H., Wills, J.M., 2000. *Phys. Rev. B* **61**, 4093.
- Galanakis, I., Dederichs, P.H., Papanikolaou, N., 2002. *Phys. Rev. B* **66**, 134428.
- Gao, L., Li, M., Samant, M.G., Hughes, B.P., Roche, K.P., Felser, C., Parkin, S.S.P., 2011. *Bull. Am. Phys. Soc.* **56**, T19.
- Gercsi, Z., Rajanikanth, A., Takahashi, Y.K., Hono, K., Kikuchi, M., Tezuka, N., Inomata, K., 2006. *Appl. Phys. Lett.* **89**, 082512.
- Gofryk, K., Kaczorowski, D., Plackowski, T., Leithe-Jasper, A., Grin, Y., 2005. *Phys. Rev. B* **72**, 094409.
- Gofryk, K., Kaczorowski, D., Plackowski, T., Mucha, J., Leithe-Jasper, A., Schnelle, W., Grin, Y., 2007. *Phys. Rev. B* **224426**, 75.
- Goldmann, J.E., 1953. *Rev. Mod. Phys.* **25**, 108.
- Graf, T., Casper, F., Winterlik, J., Balke, B., Fecher, G.H., Felser, C., 2009. *Z. Anorg. Allg. Chem.* **635**, 976.
- Graf, T., Klaer, P., Barth, J., Balke, B., Elmers, H.-J., Felser, C., 2010. *Scr. Mater.* **63**, 1216.
- Graf, T., Felser, C., Parkin, S.S.P., 2011a. *Solid State Chem.* **39**, 1.
- Graf, T., Parkin, S.S.P., Felser, C., 2011b. *IEEE Trans. Magn.* **47**, 367.
- Gruhn, T., 2010. *Phys. Rev. B* **82**, 125210.
- Gschneidner, K.A., Pecharsky, V.K., Tsokol, A.O., 2005. *Rep. Prog. Phys.* **68**, 1479.
- Gutfleisch, O., Yan, A., Müller, K.-H., 2005. *J. Appl. Phys.* **97**, 10M305.
- Gutfleisch, O., Willard, M.A., Brück, E., Chen, C.H., Sankar, S.G., Liu, J.P., 2011. *Adv. Mater.* **23**, 821.
- Hanssen, K.E.M., Mijnders, P.E., 1986. *Phys. Rev. B* **34**, 5009.
- Hanssen, K.E.M., Mijnders, P.E., Rabou, L.P.L.M., Buschow, K.H.J., 1990. *Phys. Rev. B* **42**, 1533.
- Hartjes, K., Jeitschko, W., 1995. *J. Alloys Compd.* **226**, 81.
- Hasan, M.Z., Kane, C.L., 2010. *Rev. Mod. Phys.* **82**, 3045.
- Hedin, L., Lundqvist, B.I., 1971. *J. Phys. C: Solid State Phys.* **4**, 2064.
- Helmholdt, R.B., de Groot, R.A., Mueller, F.M., van Engen, P.G., Buschow, K.H.J., 1984. *J. Magn. Magn. Mater.* **43**, 249.
- Herbot, C., Jorge, E.A., Jordan, M., 2009. *Appl. Phys. Lett.* **94**, 142504.
- Heremans, J.P., Jovovic, V., Toberer, E.S., Saramat, A., Kurosaki, K., Charoenphakdee, A., Yamanaka, S., Snyder, G.J., 2008. *Science* **321**, 554.
- Heusler, F., 1903. *Verh. Dtsch. Phys. Ges.* **5**, 219.
- Heusler, O., 1934. *Ann. Phys.* **19**, 155.
- Heusler, F., Starck, W., Haupt, E., 1903. *Verh. Dtsch. Phys. Ges.* **5**, 220.
- Heyne, L., Igarashi, T., Kanomata, T., Neumann, K.-U., Ouladdiaf, B., Ziebeck, K.R.A., 2005. *J. Phys. Condens. Matter* **17**, 4991.
- Hickey, M.C., Damsgaard, C.D., Farrer, I., Holmes, S.N., Husmann, A., Hansen, J.B., Jacobsen, C.S., Ritchie, D.A., Lee, G.A.C., Jones, R.F., Pepper, M., 2005. *Appl. Phys. Lett.* **86**, 252106.
- Hirohata, A., Kurebayashi, H., Okamura, S., Kikuchi, M., Masaki, T., Nozaki, T., Tezuka, N., Inomata, K., 2005. *J. Appl. Phys.* **97**, 103714.
- Hirohata, A., Kikuchi, M., Masaki, T., Nozaki, T., Tezuka, N., Inomata, K., Claydon, J.S., Xu, Y.B., van der Laan, G., 2006. *Curr. Opin. Solid State Mater. Sci.* **10**, 93.
- Hordequin, C., Lelivre-Bernab, E., Pierre, J., 1997a. *Phys. B* **234–236**, 602.
- Hordequin, C., Pierre, J., Currat, R., 1997b. *Phys. B* **234–236**, 605.
- Hordequin, C., Ristoiu, D., Ranno, L., Pierre, J., 2000. *Eur. Phys. J. B* **16**, 287.
- Hsieh, D., Xia, Y., Qian, D., Wray, L., Dil, J.H., Meier, F., Osterwalder, J., Patthey, L., Checkelsky, J.G., Ong, N.P., Fedorov, A.V., Lin, H., *et al.*, 2009. *Nature* **460**, 1101.

- Huai, Y., 2008. AAPPS Bull. **18**, 33.
- Ikeda, S., Miura, K., Yamamoto, H., Mizunuma, K., Gan, H.D., Endo, M., Kanai, S., Hayakawa, J., Matsukura, F., Ohno, H., 2010. Nat. Mater. **9**, 721.
- Inaba, N., Uesaka, Y., Nakamura, A., Futamoto, M., Sugita, Y., Narishige, S., 1997. IEEE Trans. Magn. **33**, 2989.
- Inomata, K., Okamura, S., Goto, R., Yezuka, N., 2003. Jpn. J. Appl. Phys. **42**, L419.
- Ishida, S., Akazawa, S., Kubo, Y., Ishida, J., 1982. J. Phys. F: Met. Phys. **12**, 1111.
- Ishida, S., Fujii, S., Kashiwagi, S., Asano, S., 1995a. J. Phys. Soc. Jpn. **64**, 2152.
- Ishida, S., Kashiwagi, S., Fujii, S., Asano, S., 1995b. Phys. B **210**, 140.
- Ishida, S., Masaki, T., Fujii, S., Asano, S., 1998. Phys. B **245**, 1.
- Ishikawa, T., Marukame, T., Kijima, H., Matsuda, K.-i., Uemura, T., Yamamoto, M., 2006. Appl. Phys. Lett. **89**, 192505.
- Ishikawa, T., Hakamata, S., Matsuda, K.-i., Uemura, T., Yamamoto, M., 2008. J. Appl. Phys. **103**, 07A919.
- Ito, K., Ito, W., Umetsu, R.Y., Nagasako, M., Kainuma, R., Fujita, A., Oikawa, K., Ishida, K., 2008. Mater. Trans. **49**, 1915.
- Jakob, G., Elmers, H.J., 2007. J. Magn. Magn. Mater. **310**, 2779.
- Jenkins, S.J., 2004. Phys. Rev. B **70**, 245401.
- Jenkins, S.J., King, D.A., 2001. Surf. Sci. **494**, L793.
- Jia, X., Yang, W., Qin, M., Wang, L., 2008. J. Phys. D: Appl. Phys. **41**, 085004.
- Jiang, C., Venkatesan, M., Coey, J.M.D., 2001. Solid State Commun. **118**, 513.
- Jiang, L., Kane, C.L., Preskill, J., 2011. Phys. Rev. Lett. **106**, 130504.
- Johnson, P.R., Kautzky, M.C., Mancoff, F.B., Kondo, R., Clemens, B.M., White, R.L., 1996. IEEE Trans. Magn. **32**, 4615.
- Jung, V., Fecher, G.H., Balke, B., Ksenofontov, V., Felser, C., 2009. J. Phys. D: Appl. Phys. **42**, 084007.
- Juza, R., Hund, F., 1948. Z. Anorg. Chem. **257**, 1.
- Kainuma, R., Imano, Y., Ito, W., Morito, H., Okamoto, S., Kitakami, O., Oikawa, K., Fujita, A., Kanomata, T., Ishida, K., 2006a. Nature **439**, 957.
- Kainuma, R., Imano, Y., Ito, W., Morito, H., Sutou, Y., Oikawa, K., Fujita, A., Ishida, K., Okamoto, S., Kitakami, O., Kanomata, T., 2006b. Appl. Phys. Lett. **88**, 192513.
- Kainuma, R., Ito, W., Umetsu, R.Y., Oikawa, K., Ishida, K., 2008. Appl. Phys. Lett. **93**, 091906.
- Kalarasse, F., Bennecer, B., 2006. J. Phys. Chem. Solids **67**, 846.
- Kämmerer, S., Thomas, A., Hütten, A., Reiss, G., 2004. Appl. Phys. Lett. **85**, 79.
- Kandpal, H.C., Felser, C., Seshadri, R., 2005. J. Phys. D: Appl. Phys. **38**, 1.
- Kandpal, H.C., Fecher, G.H., Felser, C., Schönhense, G., 2006a. Phys. Rev. B **73**, 094422.
- Kandpal, H.C., Felser, C., Seshadri, R., 2006b. J. Phys. D: Appl. Phys. **39**, 776.
- Kandpal, H.C., Fecher, G.H., Felser, C., 2007a. J. Phys. D: Appl. Phys. **40**, 1507.
- Kandpal, H.C., Fecher, G.H., Felser, C., 2007b. J. Magn. Magn. Mater. **310**, 1626.
- Kandpal, H.C., Ksenofontov, V., Wojcik, M., Seshadri, R., Felser, C., 2007c. J. Phys. D: Appl. Phys. **40**, 1587.
- Kane, C.L., Mele, E.J., 2005. Phys. Rev. Lett. **95**, 146802.
- Kanomata, T., Fukushima, K., Nishihara, H., Kainuma, R., Itoh, W., Oikawa, K., Ishida, K., Neumann, K.U., Ziebeck, K.R.A., 2008. Mater. Sci. Forum **583**, 119.
- Kanomata, T., Chieda, Y., Endo, K., Okada, H., Nagasako, M., Kobayashi, K., Kainuma, R., Umetsu, R., Takahashi, H., Furutani, Y., Nishihara, H., Abe, K., *et al.*, 2010. Phys. Rev. B **82**, 144415.
- Karla, I., Pierre, J., Skolozdra, R.V., 1998. J. Alloys Compd. **265**, 42.
- Kautzky, M.C., Mancoff, F.B., Bobo, J.-F., Johnson, P.R., White, R.L., Clemens, B.M., 1997. J. Appl. Phys. **81**, 4026.
- Khan, M., Dubenko, I., Stadler, S., Ali, N., 2007. Appl. Phys. Lett. **91**, 072510.

- Khan, M., Dubenko, I., Stadler, S., Ali, N., 2008. *J. Phys. Condens. Matter* **20**, 235204.
- Khovaylo, V.V., Buchelnikov, V.D., Kainuma, R., Koledov, V.V., Ohtsuka, M., Shavrov, V.G., Takagi, T., Taskaev, S.V., Vasiliev, A.N., 2005. *Phys. Rev. B* **72**, 224408.
- Kim, J.-W., Song, H.-S., Jeong, J.-W., Lee, K.-D., Sohn, J.-W., Shima, T., Shin, S.-C., 2011. *Appl. Phys. Lett.* **98**, 092509.
- Kirillova, M.N., Makhnev, A.A., Shreder, E.I., Dyakina, V.P., Gorina, N.B., 1995. *Phys. Stat. Sol. B* **187**, 231.
- Kisker, E., Carbone, C., Flipse, C.F., Wassermann, E.F., 1987. *J. Magn. Magn. Mater.* **70**, 21.
- Klaer, P., Jenkins, C.A., Alijani, V., Winterlik, J., Balke, B., Felser, C., Elmers, H.J., 2011. *Appl. Phys. Lett.* **98**, 212510.
- Kobayashi, K., Umetsu, R.Y., Kainuma, R., Ishida, K., Oyamada, T., Fujita, A., Fukamichi, K., 2004. *Appl. Phys. Lett.* **85**, 4684.
- Kodama, K., Furubayashi, T., Sukegawa, H., Nakatani, T.M., Inomata, K., Hono, K., 2009. *J. Appl. Phys.* **105**, 07E905.
- Kohn, W., Sham, L.J., 1965. *Phys. Rev.* **140**, 1133.
- Kokorin, V.V., Martynov, V.V., Chernenko, V.A., 1992. *Scr. Metall. Mater.* **26**, 175.
- König, M., Wiedmann, S., Brüne, C., Roth, A., Buhmann, H., Molenkamp, L., Qi, X.-L., Zhang, S.-C., 2007. *Science* **318**, 766.
- Koyama, K., Watanabe, K., Kanomata, T., Kainuma, R., Oikawa, K., Ishida, K., 2006. *Appl. Phys. Lett.* **88**, 132505.
- Krenke, T., Acct, M., Wassermann, E.F., Moya, X., Mañosa, L., Planes, A., 2005a. *Phys. Rev. B* **72**, 014412.
- Krenke, T., Duman, E., Acet, M., Wassermann, E.F., Moya, X., Mañosa, L., Planes, A., 2005b. *Nat. Mater.* **4**, 450.
- Krenke, T., Acct, M., Wassermann, E.F., Moya, X., Moñosa, L., Planes, A., 2006. *Phys. Rev. B* **73**, 174413.
- Krenke, T., Duman, E., Acct, M., Wassermann, E.F., Moya, X., Moñosa, L., Planes, A., Suard, E., Ouladdiaf, B., 2007. *Phys. Rev. B* **75**, 104414.
- Kroth, K., Balke, B., Fecher, G.H., Ksenofontov, V., Felser, C., Lin, H.-J., 2006. *Appl. Phys. Lett.* **89**, 202509.
- Ksenofontov, V., Kroth, K., Reiman, S., Casper, F., Jung, V., Takahashi, M., Takeda, M., Felser, C., 2006a. *Hyperf. Interact.* **168**, 1201.
- Ksenofontov, V., Melnyk, G., Wojcik, M., Wurmehl, S., Kroth, K., Reiman, S., Blaha, P., Felser, C., 2006b. *Phys. Rev. B* **74**, 134426.
- Kübler, J., 1984. *Phys. B* **127**, 257.
- Kübler, J., 2000. *Theory of Itinerant Electron Magnetism*. Clarendon Press, Oxford.
- Kübler, J., Williams, A.R., Sommers, C.B., 1983. *Phys. Rev. B* **28**, 1745.
- Kübler, J., Fecher, G.H., Felser, C., 2007. *Phys. Rev. B* **76**, 024414.
- Kubota, H., Nakata, J., Oogange, M., Ando, Y., Sakuma, A., Miyazaki, T., 2004. *Jpn. J. Appl. Phys.* **43**, L984.
- Kulakov, E., Mazin, I.I., 1990. *J. Phys. Condens. Matter* **2**, 343.
- Kulakov, E., Uspenskii, Y., Halilov, S., 1995. *J. Magn. Magn. Mater.* **145**, 395.
- Kurt, H., Rode, K., Venkatesan, M., Stamenov, P., Coey, J.M.D., 2011. *Phys. Rev. B* **83**, 020405.
- Kurtulus, Y., Dronskowski, R., Samolyuk, G.D., Antropov, V.P., 2005a. *Phys. Rev. B* **71**, 014425.
- Kurtulus, Y., Gilleen, M., Dronskowski, R., 2005b. *J. Comput. Chem.* **27**, 90.
- Lakshmi, N., Pandey, A., Venugopalan, K., 2002. *Bull. Mater. Sci.* **25**, 309.
- Lanska, N., Söderberg, O., Sozinov, A., Ge, Y., Ullakko, K., Lindroos, V.K., 2004. *J. Appl. Phys.* **95**, 8074.

- Larson, P., Mahanti, S.D., Sportouch, S., Kanatzidis, M.G., 1999. *Phys. Rev. B* **59**, 15660.
- Lezaic, M., Mavropoulos, P., Enkovaara, J., Bihlmayer, G., Blügel, S., 2006. *Phys. Rev. Lett.* **97**, 026404.
- Li, C.-M., Luo, H.-B., Hu, Q.-M., Yang, R., Johansson, B., Vitos, L., 2010. *Phys. Rev. B* **82**, 024201.
- Lin, H., Wray, A., Xia, Y., Xu, S., Jia, S., Cava, R.J., Bansil, A., Hasan, M.Z., 2010. *Nat. Mater.* **9**, 546.
- Liu, G.D., Chen, J.L., Liu, Z.H., Dai, X.F., Wu, G.H., Zhang, B., Zhang, X.X., 2005. *Appl. Phys. Lett.* **87**, 262504.
- Liu, G.D., Dai, X.F., Liu, H.Y., Chen, J.L., Li, Y.X., Xiao, G., Wu, G.H., 2008. *Phys. Rev. B* **77**, 014424.
- Liu, J., Scheerbaum, N., Hinz, D., Gutfleisch, O., 2008a. *Appl. Phys. Lett.* **92**, 162509.
- Liu, J., Scheerbaum, N., Weiß, S., Gutfleisch, O., 2009. *Appl. Phys. Lett.* **95**, 152503.
- Lou, X., 2010. US Patent 2010/0103565.
- Lyubina, J., Opahle, I., Müller, K.-H., Gutfleisch, O., Richter, M., Wolf, M., Schultz, L., 2005. *J. Phys. Condens. Matter* **17**, 4157.
- MacDonald, A.H., Schiffer, P., Samarth, N., 2005. *Nat. Mater.* **4**, 195.
- Malinowski, G., Kuiper, K.C., Lavrijsen, R., Swagten, H.J.M., Koopmans, B., 2009. *Appl. Phys. Lett.* **94**, 102501.
- Mancoff, F.B., Bobo, J.F., Richter, O.E., Bessho, K., Johnson, P.R., Sinclair, R., Nix, W. D., White, R.L., Clemens, B.M., 1999. *J. Mater. Res.* **14**, 1560.
- Mañosa, L., Planes, A., Bonnot, E., Acet, M., Duman, E., Wassermann, E.F., 2004. *J. Magn. Magn. Mater.* **272**, 2090.
- Mañosa, L., Gonzáles-Alonso, D., Planes, A., Bonnot, E., Barrio, M., Tamarit, J.-L., Aksoy, S., Acet, M., 2010. *Nat. Mater.* **9**, 478.
- Marcos, J., Planes, A., Mañosa, L., Casanova, F., Batlle, X., Labarta, A., Martínez, B., 2002. *Phys. Rev. B* **66**, 224413.
- Marcos, J., Mañosa, L., Planes, A., Casanova, F., Batlle, X., Labarta, A., 2003. *Phys. Rev. B* **68**, 094401.
- Martin, J.J., 1972. *J. Phys. Chem. Solids* **33**, 1139.
- Martynov, V.V., Kokorin, V.V., 1992. *J. Phys. III France* **2**, 739.
- Marukame, T., Yamamoto, M., 2007. *J. Appl. Phys.* **101**, 083906.
- Marukame, T., Ishikawa, T., Matsuda, K.-i., Uemura, T., Yamamoto, M., 2006. *J. Appl. Phys.* **99**, 08A904.
- Marukame, T., Ishikawa, T., Hakamata, S., Matsuda, K.-i., Uemura, T., Yamamoto, M., 2007. *Appl. Phys. Lett.* **90**, 012508.
- Masek, J., Kudrnovsky, J., Maca, F., Gallagher, B., Champion, R., Gregory, D., Jungwirth, T., 2007. *Phys. Rev. Lett.* **98**, 067202.
- Mathon, J., Umerski, A., 2001. *Phys. Rev. B* **63**, 220403(R).
- Miura, Y., Nagao, K., Shirai, M., 2004a. *Phys. Rev. B* **69**, 144413.
- Miura, Y., Shirai, M., Nagao, K., 2004b. *J. Appl. Phys.* **95**, 7225.
- Miura, Y., Uchida, H., Oba, Y., Nagao, K., Shirai, M., 2007. *J. Phys. Condens. Matter* **19**, 365228.
- Mizukami, S., Sajitha, E.P., Watanabe, D., Wu, F., Miyazaki, T., Naganuma, H., Oogane, M., Ando, Y., 2010a. *Appl. Phys. Lett.* **96**, 152502.
- Mizukami, S., Watanabe, D., Kubota, T., Zhang, X., Naganuma, H., Oogane, M., Ando, Y., Miyazaki, T., 2010b. *Appl. Phys. Exp.* **3**, 123001.
- Mizukami, S., Iihama, S., Inami, N., Hiratsuka, T., Kim, G., Naganuma, H., Oogane, M., Ando, Y., 2011a. *Appl. Phys. Lett.* **98**, 052501.
- Mizukami, S., Wu, F., Sakuma, A., Walowski, J., Watanabe, D., Kubota, T., Zhang, X., Naganuma, H., Oogane, M., Ando, Y., Miyazaki, T., 2011b. *Phys. Rev. Lett.* **106**, 117201.

- Mizukami, S., Zhang, X., Kubota, T., Naganuma, H., Oogane, M., Ando, Y., Miyazaki, T., 2011. *Appl. Phys. Exp.* **4**, 013005.
- Mohn, P., Blaha, P., Schwarz, K., 1995. *J. Magn. Magn. Mater.* **140–144**, 183.
- Moore, J., 2009. *Nat. Phys.* **5**, 378.
- Müchler, L., Zhang, H., Chadov, S., Yan, B., Casper, F., Kübler, J., Zhang, S.-C., Felser, C., 2012. *Angew. Chem. Int. Ed.* **51**(29), 7221–7225.
- Murray, S.J., Marioni, M., Allen, S.M., O'Handley, R.C., Lograsso, T.A., 2000. *Appl. Phys. Lett.* **77**, 886.
- Nagao, K., Shirai, M., Miura, Y., 2004. *J. Phys. Condens. Matter* **16**, S5725.
- Nakatani, T.M., Furubayashi, T., Kasai, S., Sukegawa, H., Takahashi, Y.K., Mitani, S., Hono, K., 2010. *Appl. Phys. Lett.* **96**, 212501.
- Nayak, A.K., Shekhar, C., Winterlik, J., Gupta, A., Felser, C., 2012. *Appl. Phys. Lett.* **100**, 152404.
- Nikolaev, K., Anderson, P., Kolbo, P., Dimitrov, D., Xue, S., Peng, X., Pokhil, T., Cho, H., Chen, Y., 2008. *J. Appl. Phys.* **103**, 07F533.
- Nikolaev, K., Kolbo, P., Pokhil, T., Peng, X., Chen, Y., Ambrose, T., Mryasov, O., 2009. *Appl. Phys. Lett.* **94**, 222501.
- Nowotny, H., Bachmayer, K., 1950. *Monatsh. Chem.* **81**, 488.
- Nowotny, H., Holub, F., 1960. *Monatsh. Chem.* **91**, 877.
- Nowotny, H., Sibert, W., 1941. *Z. Metallkunde* **33**, 391.
- Nozaki, Y., Narita, N., Tanaka, T., Matsuyama, K., 2009. *Appl. Phys. Lett.* **95**, 082505.
- Nuss, J., Jansen, M., 2002. *Z. Anorg. Allg. Chem.* **628**, 1152.
- O'Handley, R.C., Murray, S.J., Marioni, M., Nembach, H., Allen, S.M., 2000. *J. Appl. Phys.* **87**, 4712.
- Oestreich, J., Probst, U., Richardt, F., Bucher, E., 2003. *J. Phys. Condens. Matter* **15**, 635.
- Offernes, L., Ravindran, P., Kjekshus, A., 2003. *Appl. Phys. Lett.* **82**, 2862.
- Offernes, L., Ravindran, P., Kjekshus, A., 2007. *J. Alloys Compd.* **439**, 37.
- Ohno, H., Shen, A., Matsukura, F., Oiwa, A., Endo, A., Katsumoto, S., Iye, Y., 1996. *Appl. Phys. Lett.* **69**, 363.
- Okamura, S., Goto, R., Sugimoto, S., Tezuka, N., Inomata, K., 2004. *J. Appl. Phys.* **96**, 6561.
- Okamura, S., Miyazaki, A., Sugimoto, S., Tezuka, N., Inomata, K., 2005. *Appl. Phys. Lett.* **86**, 232503.
- Oogane, M., Sakuraba, Y., Nakata, J., Kubota, H., Ando, Y., Sakuma, A., Miyazaki, T., 2006. *J. Phys. D: Appl. Phys.* **39**, 834.
- Orgassa, D., Fujiwara, H., Schulthess, T.C., Butler, W.H., 1999. *Phys. Rev. B* **60**, 13237.
- Orgassa, D., Fujiwara, H., Schulthess, T.C., Butler, W.H., 2000. *J. Appl. Phys.* **87**, 5870.
- Otto, M.J., van Woerden, R.A.M., van de Valk, P.J., Wijngaard, J., van Bruggen, C.F., Haas, C., 1989. *J. Phys. Condens. Matter* **1**, 2351.
- Ouardi, S., Fecher, G., Balke, B., Schwall, M., Kozina, G., Stryanyuk, X., Felser, C., Ikenaga, E., Yamashita, Y., Ueda, S., Kobayashi, K., 2010a. *Appl. Phys. Lett.* **97**, 252113.
- Ouardi, S., Fecher, G.H., Balke, B., Kozina, X., Stryanyuk, G., Felser, C., Lowitzer, S., Ködderitzsch, D., Ebert, H., Ikenaga, E., 2010b. *Phys. Rev. B* **82**, 085108.
- Ouardi, S., Shekhar, C., Fecher, G.H., Kozina, X., Stryanyuk, G., Felser, C., Ueda, S., Kobayashi, K., 2011. *Appl. Phys. Lett.* **98**, 211901.
- Pal, S., Rana, B., Hellwig, O., Thomson, T., Barman, A., 2011. *Appl. Phys. Lett.* **98**, 082501.
- Pareti, L., Solzi, M., Albertini, F., Paoluzi, A., 2003. *Eur. Phys. J. B* **32**, 303.
- Parkin, S.S.P., Kaiser, C., Panchula, A., Rice, P.M., Hughes, B., Samant, M., Yang, S.H., 2004. *Nat. Mater.* **3**, 862.
- Parkin, S.S.P., Hayashi, M., Thomas, L., 2008. *Science* **320**, 190.



- Pauling, L., 1938. Phys. Rev. **54**, 899.
- Pecharsky, V.K., Gscheidner, K.A., 1997. Phys. Rev. Lett. **78**, 4494.
- Perdew, J.P., Yue, W., 1986. Phys. Rev. B **33**, 8800.
- Perdew, J.P., Chevary, J.A., Vosko, S.H., Jackson, K.A., Pederson, M.R., Singh, D.J., Fiolhais, C., 1992. Phys. Rev. B **46**, 6671.
- Perdew, J.P., Burke, K., Ernzerhof, M., 1996. Phys. Rev. Lett. **77**, 3865.
- Perdew, J.P., Burke, K., Ernzerhof, M., 1997. Phys. Rev. Lett. **78**, 1396.
- Pickett, W.E., 1996. Phys. Rev. Lett. **77**, 3185.
- Picozzi, S., Continenza, A., Freeman, A.J., 2002. Phys. Rev. B **66**, 094421.
- Picozzi, S., Continenza, A., Freeman, A.J., 2003. J. Phys. Chem. Solids **64**, 1697.
- Picozzi, S., Continenza, A., Freeman, A.J., 2004. Phys. Rev. B **69**, 094423.
- Pierre, J., Karla, I., 2000. J. Magn. Magn. Mater. **217**, 74.
- Pierre, J., Skolozdra, R.V., Gorelenko, Y.K., Kouacou, M.A., 1994. J. Magn. Magn. Mater. **134**, 95.
- Planes, A., Mañosa, L., Acct, M., 2009. J. Phys. Condens. Matter **21**, 233201.
- Pons, J., Seguí, C., Chernenko, V.A., Cesari, E., Ochín, P., Protier, R., 1999. Mater. Sci. Eng. **A273–275**, 315.
- Pötschke, M., Gaitzsch, U., Roth, S., Rellinghaus, B., Schultz, L., 2007. J. Magn. Magn. Mater. **316**, 383.
- Puselj, M., Ban, Z., 1969. Croat. Chem. Acta. **41**, 79.
- Qi, X.-L., Zhang, S.-C., 2010. Phys. Today **63**, 33.
- Ristoiu, D., Nozieres, J.P., Borca, C.N., Borca, B., Dowben, P.A., 2000a. Appl. Phys. Lett. **76**, 2349.
- Ristoiu, D., Nozieres, J.P., Borca, C.N., Komesu, H.-k., Jeong, T., Dowben, P.A., 2000b. Europhys. Lett. **49**, 624.
- Rowe, D., 2006. Thermoelectrics Handbook: Macro to Nano. CRC Taylor & Francis, Boca Raton.
- Sakuraba, Y., Hattori, M., Oogane, M., Ando, Y., Kato, H., Sakuma, A., Miyazaki, T., Kubota, H., 2006. Appl. Phys. Lett. **88**, 192508.
- Sakuraba, Y., Iwase, T., Mitani, S., Takanashi, K., 2009. Appl. Phys. Lett. **94**, 012511.
- Sakuraba, Y., Izumi, K., Iwase, T., Bosu, S., Saito, K., Takanashi, K., Miura, Y., Futatsukawa, K., Abe, K., Shirai, M., 2010. Phys. Rev. B **82**, 094444.
- Sakurada, S., Shutoh, N., 2005. Appl. Phys. Lett. **86**, 082105.
- Schmalhorst, J., Kämmerer, S., Sacher, M., Reiss, G., Hütten, A., Scholl, A., 2004. Phys. Rev. B **70**, 024426.
- Schwall, M., Balke, B., 2011. Appl. Phys. Lett. **98**, 042106.
- Sharma, V.K., Chattopadhyat, M.K., Shaeb, K.H.B., Chouhan, A., Roy, S.B., 2006. Appl. Phys. Lett. **89**, 222509.
- Shutoh, N., Sakurada, S., 2005. J. Alloys Compd. **389**(1–2), 204.
- Skovsen, I., Bjerg, L., Christensen, M., Nishibori, E., Balke, B., Felser, C., Iversen, B.B., 2010. Dalton Trans. **39**, 10154.
- Slater, J.C., 1936a. Phys. Rev. **49**, 537.
- Slater, J.C., 1936b. Phys. Rev. **49**, 931.
- Slonczewski, J., 1996. J. Magn. Magn. Mater. **159**, L1.
- Sootsman, J.R., Chung, D.Y., Kanatzidis, M.G., 2009. Angew. Chem. Int. Ed. **48**(46), 8616.
- Soulen, R.J. Jr., Byers, J.M., Osofsky, M.S., Nadgorny, B., Cheng, S.F., Broussard, P.R., Tanaka, C.T., Nowack, J., Moodera, J.S., Barry, A., *et al.*, 1998. Science **282**, 85.
- Soulen, R.J., Osofsky, M.S., Nadgorny, B., Broussard, P.R., Cheng, S.F., Byers, J.M., Tanaka, C.T., Nowack, J., Moodera, J.S., Laprade, G., Barry, A., Coey, M.D., 1999. J. Appl. Phys. **85**, 4589.
- Sozinov, A., Likhachev, A.A., Lanska, N., Ullakko, K., 2002. Appl. Phys. Lett. **80**, 1746.

- Spina, L., Jia, Y.-Z., Ducourant, B., Tillard, M., Belin, C., 2003. *Z. Kristallogr.* **218**, 740.
- Suits, J.C., 1976. *Solid State Commun.* **18**, 423.
- Surikov, V.V., Zhordochkin, V.N., Astakhova, T.Y., 1990. *Hyperf. Interact.* **59**, 469.
- Szytula, A., 1991. In: Buschow, K.H.J. (Ed.), *Handbook of Magnetic Materials* Vol. 6, North Holland, Amsterdam, p. 85.
- Taira, T., Ishikawa, T., Itabashi, N., Matsuda, K., Uemura, T., Yamamoto, M., 2009. *J. Phys. D: Appl. Phys.* **42**, 084015.
- Takeuchi, I., Famodu, O.O., Read, J.C., Aronova, M.A., Chang, K.-S., Craciunescu, C., Lofland, S.E., Wuttig, M., Wellstood, F.C., Knauss, L., Orozco, A., 2003. *Nat. Mater.* **2**, 180.
- Tanaka, C.T., Nowak, J., Moodera, J.S., 1999. *J. Appl. Phys.* **86**, 6239.
- Tegus, O., Brück, E., Buschow, K.H.J., de Boer, F.R., 2002. *Nature* **415**, 150.
- Teo, J.C.Y., Fu, L., Kane, C.L., 2008. *Phys. Rev. B* **78**, 045426.
- Tezuka, N., Ikeda, N., Miyazaki, A., Sugimoto, S., Kikuchi, M., Inomata, K., 2006a. *Appl. Phys. Lett.* **89**, 112514.
- Tezuka, N., Ikeda, N., Sugimoto, S., Inomata, K., 2006b. *Appl. Phys. Lett.* **89**, 252508.
- Tezuka, N., Ikeda, N., Sugimoto, S., Inomata, K., 2007. *Jpn. J. Appl. Phys.* **46**, L454.
- Tezuka, N., Ikeda, N., Mitsunashi, F., Sugimoto, S., 2009. *Appl. Phys. Lett.* **94**, 162504.
- Tickle, R., James, R.D., 1999. *J. Magn. Magn. Mater.* **195**, 627.
- Tobola, J., Pierre, J., Kaprzyk, S., Skolozdra, R.V., Kouacou, M.A., 1998. *J. Phys. Condens. Matter* **10**, 1013.
- Tsunegi, S., Sakuraba, Y., Oogane, M., Takanashi, K., Ando, Y., 2008. *Appl. Phys. Lett.* **93**, 112506.
- Tsunegi, S., Sakuraba, Y., Oogane, M., Telling, N.D., Sheldford, L.R., Arenholz, E., van der Laan, G., Hicken, R.J., Takanashi, K., Ando, Y., 2009. *J. Phys. D: Appl. Phys.* **42**, 195004.
- Ullakko, K., Huang, J.K., Kantner, C., O'Handley, R.C., Kokorin, V.V., 1996. *Appl. Phys. Lett.* **69**, 1966.
- van Engen, P.G., Bushow, K.H.J., 1983. *J. Magn. Magn. Mater.* **30**, 374.
- van Engen, P.G., Bushow, K.H.J., Jongebreur, R., Erman, M., 1983. *Appl. Phys. Lett.* **42**, 202.
- Van Roy, W., De Boeck, J., Brijs, B., Borghs, G., 2000a. *J. Cryst. Growth* **227**, 862.
- Van Roy, W., De Boeck, J., Brijs, B., Borghs, G., 2000b. *Appl. Phys. Lett.* **77**, 4190.
- Van Roy, W., Wojcik, M., Jedryka, E., Nadolski, S., Jalabert, D., Brijs, B., Borghs, G., De Boeck, J., 2003. *Appl. Phys. Lett.* **83**, 4214.
- van Vleck, J.H., 1945. *Rev. Mod. Phys.* **17**, 27.
- van Vleck, J.H., 1953. *Rev. Mod. Phys.* **25**, 220.
- Vaz, C.A.F., Rhensius, J., Heidler, J., Wohlhüter, A., Bisig, P., Körner, H.S., Montes, T.O., Locatelli, A., Le Guyader, L., Nolting, F., Graf, T., Felser, C., Heyderman, K.J., *et al.*, 2011. *Appl. Phys. Lett.* **99**, 185210.
- Villars, P., Calvert, L.D., 1991. *Pearson's Handbook of Crystallographic Data for Intermetallic Phases*. American Society for Metals, Metals Park, OH.
- von Barth, U., Hedin, L., 1972. *J. Phys. C: Solid State Phys.* **5**, 1629.
- Wada, H., Tanabe, Y., 2001. *Appl. Phys. Lett.* **79**, 3302.
- Wang, X., Antropov, V.P., Harmon, B.N., 1994. *IEEE Trans. Magn.* **30**, 4458.
- Wang, W., Lui, E., Kodzuka, M., Sukegawa, H., Wojcik, M., Jedryka, E., Wu, G.H., Inomata, K., Mitani, S., Hono, K., 2010. *Phys. Rev. B* **81**, 140402(R).
- Webster, P.J., 1969. *Contemp. Phys.* **10**, 559.
- Webster, P.J., 1971. *J. Phys. Chem. Solids* **32**, 1221.
- Webster, P.J., Ziebeck, K.R.A., 1973. *J. Phys. Chem. Solids* **34**, 1647.
- Webster, P.J., Ziebeck, K.R.A., 1988. *Landolt-Börnstein—Group III Condensed Matter* Vol. 19C, Springer, Berlinpp. 75–184.

- Webster, P.J., Ziebeck, K.R.A., Town, S.L., Peak, M.S., 1984. *Philos. Mag. B* **49**, 295.
- Weht, R., Pickett, W.E., 1999. *Phys. Rev. B* **60**, 13006.
- Wijngaard, J.H., Haas, C., de Groot, R.A., 1989. *Phys. Rev. B* **40**, 9319.
- Winterlik, J., Balke, B., Fecher, G.H., Felser, C., 2008. *Phys. Rev. B* **77**, 054406.
- Winterlik, J., Fecher, G.H., Thomas, A., Felser, C., 2009. *Phys. Rev. B* **79**, 064508.
- Winterlik, S., Chadov, J., Gupta, A., Alijani, V., Gasi, T., Filsinger, K., Balke, B., Fecher, G. H., Jenkins, C.A., Kübler, J., Liu, G., Parkin, S. S. P., Felser, C., 2012. *Adv. Mater.* (online).
- Wolter, A.U.B., Klauss, H.H., Lifferst, F.J., Geibel, C., Sullow, S., 2002. *J. Magn. Magn. Mater.* **242**, 888.
- Wu, F., Mizukami, S., Watanabe, D., Naganuma, H., Oogane, M., Ando, Y., Miyazaki, T., 2009. *Appl. Phys. Lett.* **94**, 122503.
- Wu, F., Mizukami, S., Watanabe, D., Sajitha, E.P., Naganuma, H., Oogane, M., Ando, Y., Miyazaki, T., 2010. *IEEE Trans. Magn.* **46**, 1863.
- Wurmehl, S., Fecher, G.H., Kandpal, H.C., Ksenofontov, V., Felser, C., Lin, H.-J., Morais, J., 2005. *Phys. Rev. B* **72**, 184434.
- Wurmehl, S., Fecher, G.H., Kandpal, H.C., Ksenofontov, V., Felser, C., Lin, H.-J., 2006a. *Appl. Phys. Lett.* **88**, 032503.
- Wurmehl, S., Fecher, G.H., Kroth, K., Kronast, F., Dürr, H.A., Takeda, Y., Saitoh, Y., Kobayashi, K., Lin, H.-J., Schönhense, G., Felser, C., 2006b. *J. Phys. D: Appl. Phys.* **39**, 803.
- Wurmehl, S., Fecher, G.H., Ksenofontov, V., Casper, F., Stumm, U., Felser, C., Lin, H.-J., Hwu, Y., 2006c. *J. Appl. Phys.* **99**, 08J103.
- Wurmehl, S., Kandpal, H.C., Fecher, G.H., Felser, C., 2006d. *J. Phys. Condens. Matter* **18**, 6171.
- Xia, Y., Qian, D., Hsieh, D., Wray, L., Pal, A., Lin, H., Bansil, A., Grauer, D., Hor, Y.S., Cava, R.J., Hasan, M.Z., 2009. *Nat. Phys.* **5**, 398.
- Xuan, H.C., Cao, Q.Q., Zhang, C.L., Ma, S.C., Chen, S.Y., Wang, D.H., Du, Y.W., 2010. *Appl. Phys. Lett.* **96**, 202502.
- Yakushiji, K., Saito, K., Mitani, S., Takamashi, K., Takahashi, Y.K., Hono, K., 2006. *Appl. Phys. Lett.* **88**, 222504.
- Yamamoto, M., Marukame, T., Ishikawa, T., Matsuda, K.-i., Uemura, T., Arita, M., 2006. *J. Phys. D: Appl. Phys.* **39**, 824.
- Yamamoto, M., Ishikawa, T., Taira, T., Li, G.-f., Matsuda, K.-i., Uemura, T., 2010. *J. Phys. Condens. Matter* **22**, 164212.
- Yan, X., Joshi, G., Liu, W., Lan, Y., Wang, H., Lee, S., Simonson, J.W., Poon, S.J., Tritt, T. M., Chen, G., Ren, Z.F., 2011. *Nano Lett.* **11**, 556.
- Yan, B., Mückler, L., Qi, X.-L., Zhang, S.-C., Felser, C., 2012. *Phys. Rev. B* **85**, 165125.
- Yang, J., Li, H., Wu, T., Zhang, W., Chen, L., Yang, J., 2008. *Adv. Funct. Mater.* **18**(19), 2880.
- Youn, S.J., Min, B.I., 1995. *Phys. Rev. B* **51**, 10436.
- Yuasa, S., Nagahama, T., Fukushima, A., Suzuki, Y., Ando, K., 2004. *Nat. Mater.* **3**, 868.
- Zhang, M., Liu, Z., Hu, H., Liu, G., Cui, Y., Chen, J., Wu, G., Zhang, X., Xiao, G., 2004. *J. Magn. Magn. Mater.* **277**, 30.
- Zhang, H., Liu, C.-X., Qi, X.-L., Dai, X., Fang, Z., Zhang, S.-C., 2009a. *Nat. Phys.* **5**, 438.
- Zhang, K., Li, M., Zhou, Y., Oikawa, S., Yamada, K., Kou, K., 2009. US Patent 2009/0257151.
- Zhou, X., Li, W., Kunkel, H.P., Williams, G., 2004. *J. Phys. Condens. Matter* **16**, L39.
- Zhu, W., Liu, E.K., Feng, L., Tang, X.D., Chen, J.L., Wu, G.H., Liu, H.Y., Meng, F.B., Luo, H.Z., 2009. *Appl. Phys. Lett.* **95**, 222512.
- Ziebeck, K.R.A., Neumann, K.-U., 2001. *Landolt-Börnstein—Group III Condensed Matter Vol. 32C*, Springer, Berlinpp. 64–314.